# Development of ultra-stable laser sources and long-distance optical link via telecommunication networks

Haifeng Jiang

Observatoire de Paris-SYRTE

Université Paris 13-Laboratoire de Physique des Lasers

# Development of ultra-stable laser sources and long-distance optical link via telecommunication networks

# Développement de liens optiques ultra-stables pour le transfert de fréquences à longues distances

A thesis submitted at Université Paris 13 by

Haifeng JIANG

for the degree of *Doctor of Philosophy*
*Specialty: Physics*

Defended on October 26th 2010 in front of the commission consisting of:

| | | |
|---|---|---|
| Mme | Anne AMY-KLEIN | Directrice de thèse |
| M. | Fabien BRETENAKER | Examinateur |
| Mme | Gesine GROSCHE | Rapportrice |
| Mme | Martina KNOOP | Rapportrice |
| M. | Vincent LORENT | Président du jury |
| M. | André LUITEN | Examinateur |
| M. | Giorgio SANTARELLI | Co-encadrant |

# Acknowledgements

I am heartily thankful to my supervisors, Giorgio Santarelli and Anne Amy-Klein, whose guidance and support from the start to the end enabled me to think and work in a good way and finally fulfill the thesis.

I would like to thank our research team members and closely related staffs: Fabien Kéfélian, Scott Crane, Olivier Lopez, Jacques Millo, Pierre Lemonde, André Clairon and Adil Haboucha.

I would like also to thank staffs and students in LNE-SYRTE: Noël Dimarcq, Yann Le coq, Michel Lours, Laurent Voledimer, José Pinto fernandes, David Holleville, Annie Gérard, Sébastien Bize, Peter Rosenbusch, Peter Wolf, Pascal Blondé, Jérôme Lodewyck, Marine Pailler, Véronique Benayoun, Anne Quezel, Florence Cornu, Philip Westergaard, Sinda Mejri, Wei Zhang, Lin Yi, Kunliang Yao, Xiaolong Wang.....

I would like to thank my wife and parents for being eternally supportive and taking care of my son.

Financial support from Institut Francilien de Recherche sur les Atomes Froids - IFRAF is gratefully acknowledged.

# Contents

# Chapter 1

# Introduction

## 1.1 Time and frequency

The international system of units (SI) defines the seven basic units to describe length, mass, time, electric current, thermodynamic temperature, amount of substance and luminous intensity. The unit of time, the second (s), was defined originally by the mean solar day. In order to define the second more accurately, the $13^{th}$ general conference on weights and measures (CGPM) adopted another definition based on atomic transition in 1967. ***The second*** is the duration of 9192631770 periods of the radiation, corresponding to the transition between the two hyperfine levels of the ground state of the cesium 133 atom.

Frequency is the number of occurrences of a repeating event per unit time. In SI units, the unit of frequency is Hertz (Hz), named after the German physicist Heinrich Hertz. 1 `Hz` means that an event repeats once per second. ***The frequency*** $f$ is indeed the reciprocal of the period time $\tau$: $f = \frac{1}{\tau}$.

An atomic clock, also called a frequency standard, generates a stable signal for frequency calibration or reference. Its frequency is stabilized to the transition frequency of the neutral atom or ion. The primary frequency standard is a cesium atomic clock, which realizes the definition of the time/frequency with a given accuracy. The atomic clocks based on other transitions are therefore named as secondary frequency standards. In terms of the atomic species, there are several types of atomic clocks, which can be active or passive, hot or cold (atom temperature), neutral or ionic, in microwave or optical frequency (transition frequency).

Nowadays, the SI second is the most accurate unit to be realized. Consequently, the

frequency metrology becomes the core technique in metrologies and widely used in many applications, such as:

- global positioning systems (GPS, GALILEO, GLONASS, Compass),
- synchronization of telecommunication system and secure communications,
- measurement of fundamental physical constants and other units,
- detection of the gravitational waves (LISA, LIGO...)
- geodesy (gravitational red shift),
- deep space navigation,
- radio telescopes (very long baseline interferometry).

## 1.2 Frequency metrology

### 1.2.1 The atomic clock

The atomic clock plays a central role in frequency metrology. Its performance is evaluated in terms of:

- Accuracy: the degree of closeness between the clock frequency and the exact value of the atomic transition with given experimental conditions.
- Stability/instability: the degree of clock frequency fluctuation for defined time scales.

#### 1.2.1.1 A brief history

Fig.1.1 shows the principle scheme of a passive atomic clock, where the local oscillator's frequency is stabilized to the atomic transition.

The idea of using atomic resonance to measure time occurred as early as the nineteenth century (Maxwell, 1873; Thomson & Tait, 1878). Many years later, use of an atomic beam magnetic resonance as the basis of a clock was put forward (Rabi, 1945). The first atomic clock was an ammonia maser device built in 1949 at the National Bureau of Standards (now NIST) in the United States. It was less stable than existing quartz clocks, but served to demonstrate the concept. In 1947, the separated oscillatory field method was invented for measuring the

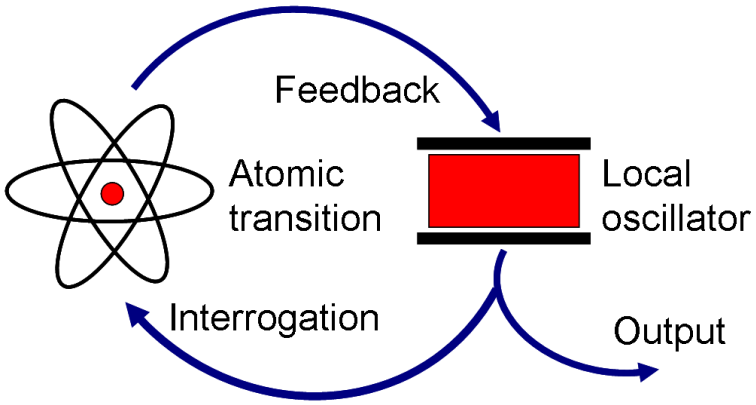


Figure 1.1: Principle of a passive atomic clock.

resonance of the hydrogen molecular beam (Ramsey & Silsbee, 1951). This method improves the accuracy of the transition frequency determination. In 1955, the first accurate atomic clock, based on the hyperfine fundamental transition of the caesium-133 atom, was built at National Physical Laboratory in the United Kingdom (Essen & Parry, 1955). It was a passive atomic clock, and requires a microwave interrogation oscillator producing a probe signal at the frequency close the atomic transition. Its fractional frequency stability was claimed to be in the level of $10^{-9}$.

In 1960, the first atomic hydrogen maser was constructed and successfully operated at Lyman Physics Laboratory of Harvard university in the United States. In this maser, hydrogen atoms in the upper hyperfine state of the fundamental level are continuously selected and injected into a high quality-factor resonant cavity (Ramsey, 1965). It emits spontaneously a stable microwave signal, therefore, is also called an active atomic clock.

Laser cooling and trapping techniques became mature in 1990s (Chu, 1998; Cohen-Tannoudji, 1998; Phillips, 1998). These techniques significantly reduced the Doppler effect, which limited the performance of the early atomic clocks. Finally, the first primary frequency standard, based on Zacharias fountain concept (Ramsey, 1983), was operated at BNM-LPTF (now LNE-SYRTE) in Paris in 1995 (Clairon *et al.*, 1995). A fractional frequency uncertainty of $\sim 10^{-15}$ was obtained.

Since 1995, the microwave fountain clocks have been improved to be mainly limited by the quantum fluctuations effect. The fractional frequency instability of the fountain clocks is

then (Santarelli *et al.*, 1999)

$$\sigma_y(\tau) = \frac{\Delta\nu}{\pi\nu_0}\sqrt{\frac{T_c}{\tau N}}, \tag{1.1}$$

where $\nu_0$ is the transition frequency, $\Delta\nu$ is the interrogation linewidth with the Ramsey separated-field technique, $T_c$ is the cycle time for determination the transition frequency, $\tau > T_c$ is the integration time and $N$ is the number of atoms detected for each cycle.

Optical frequencies are around 5 orders of magnitude higher than the operating frequency of the microwave atomic clock, while the linewidth ($\Delta\nu$) in the two spectral regions are comparable. Consequently, an improvement in stability can be obtained by a standard on an atomic transition in the optical rather than the microwave region.

New technologies, such as femtosecond frequency combs, optical lattices, ultra-stable optical cavity and quantum information, enable the realization of more stable and accurate optical clocks. These atomic systems include $Al^+$, $Ca^+$, $Ca$, $H$, $Hg^+$, $Hg$, $In^+$, $Mg$, $Sr^+$, $Sr$, $Yb^+$ and $Yb$. Several optical clocks have already achieved better stability than the best microwave clocks.

#### 1.2.1.2 The state-of-the-art

The rubidium, cesium and hydrogen maser clocks are commercially available atomic frequency standards without using the laser cooling technique. The best hydrogen maser exhibits a fractional frequency stability of $\sim 10^{-15}$ for integration times longer than $10^4$ s.

Two major types of cold-atom microwave frequency standards are the rubidium and cesium fountain clocks, which typically show a fractional frequency stability of a few $10^{-16}$ for long term (Gerginov *et al.*, 2010; Jefferts *et al.*, 2007; Levi *et al.*, 2006; Parker, 2010; Szymaniec *et al.*, 2005; Vian *et al.*, 2005). The PHARAO[1] atomic clock will be launched in 2013 with a projected fractional instability and accuracy of $10^{-16}$, according to the plan of the ACES (Atomic Clock Ensemble in Space) project (Much *et al.*, 2009). It is a cesium cold atomic clock, and may become the best microwave clock in the future, thanks to improved interrogation times as result of lack of gravity.

Either single ion isolated in a ion trap or atoms confined in optical lattices can be used to realize optical frequency standards. Both methods enable the interrogation of atomic samples in a confined space with dimensions less than the wavelength of the probe light (Lamb-Dicke regime). Thus, the Doppler broadening of the clock transition is well reduced (Dicke, 1953).

[1] Projet d'horloge atomique par refroidissement d'atomes en orbit

The neutral atom clock has achieved a fractional frequency instability of $\sim 10^{-16}$ (Campbell *et al.*, 2008), while the ion clock has reached a fractional uncertainty of slightly less than $10^{-17}$ (Chou *et al.*, 2010).

The operation cycle of cold atoms/ions clocks is about 1 s or longer, limiting the control bandwidth of the local oscillator's frequency noise. Therefore, the Dick effect degrades the frequency stability of clocks due to local oscillator noise and pulse operation with dead-time (Dick, 1987; Quessada *et al.*, 2003; Santarelli *et al.*, 1998). Consequently, it is essential to use ultra-stable local oscillators in these clocks. Fortunately, local oscillators stabilized to the cryogenic sapphire or ultra-stable Fabry-Perot cavity can reach a fractional stability of $10^{-15}$ or better at 1 s integration time.

The general theory of relativity gives that the clocks frequency located at gravitational potential $U1$ and $U2$ differ fractionally by $(U1 - U2)/c^2$, where $c$ is the speed of light. The geoid is a hypothetical surface of constant gravitational potential. At present, the geoid fluctuation effect limits the fractional frequency stability estimated to be a few $10^{-17}$ per year (Kleppner, 2006; Pavlis & Weiss, 2003). In order to overpass this limitation, it may be necessary to operate an optical clock in space, where spatial and temporal variations of the Earth's gravitational field are much smaller than on the ground.

### 1.2.2 Optical frequency synthesizer and frequency measurement

Optical frequency standards, as secondary standards, require calibration by comparison with primary frequency standards. The first optical frequency measurement ($\sim 1$ THz) was carried out in 1967 at MIT (Hocker *et al.*, 1967). In 1986, an optical frequency synthesizer linking infrared (30 THz) and microwave (9.2 GHz) frequencies was performed at BMM-LPTF (Clairon *et al.*, 1988). In 1990s, the early bridges from microwave frequency (9.2 GHz) to visible optical frequency were established at BNM-LPTF and PTB[1] (Schnatz *et al.*, 1996; Touahri *et al.*, 1995). These synthesizer chains are complex and costly, including a lot of frequency-conversion stages.

The invention of the optical frequency comb synthesizer provides a shortcut for converting frequencies between the optical and micorwave/RF ranges (Diddams *et al.*, 2000; Udem *et al.*, 1999). Taking advantage of the mode-locked laser and ultra-high nonlinear fiber techniques, the optical comb compares the frequencies over a wide span from the mircrowave/RF to

[1] the national frequency metrology laboratory in Germany

optical frequencies in a single stage. This synthesizer can also directly yield an optical-to-optical frequency conversion in its operational frequency range.

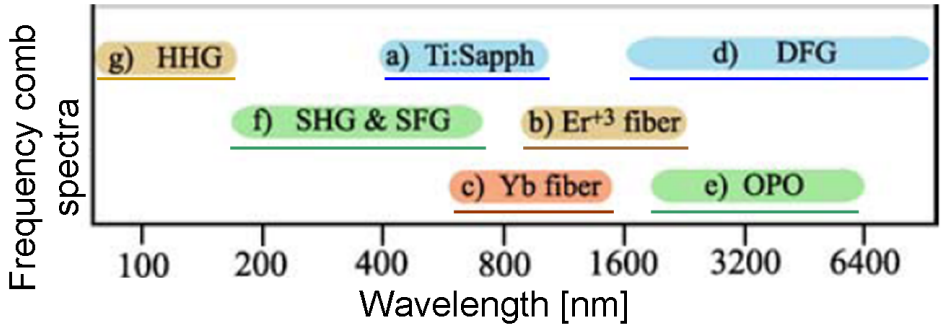


Figure 1.2: Operational frequency range of optical combs [from Thorpe & Ye (2008)], a) Ti:sapphire mode-locked laser, b) erbium-doped fiber laser, c) ytterbium-doped fiber laser, d) difference frequency generation, e) optical parametric oscillator, f) second-harmonic generation and sum-frequency generation, g) high-harmonic generation, note that d-g are the frequency conversion techniques.

Fig.1.2 shows the operational frequency ranges of different optical combs, covering the wavelength span from 75 nm to 10 $\mu$m. Optical frequency combs have also been used to measure infrared frequencies with the sum-frequency generation (SFG) technique at 3.39 $\mu$m (Mucke *et al.*, 2004) and 10 $\mu$m (Amy-Klein *et al.*, 2004, 2005). The fractional frequency instability of a conversion between optical frequencies is in the range of $10^{-17}$ at 1 s, and averages down to the range of $10^{-19}$ for integration times longer a few tens of second (Ma *et al.*, 2007). The instability of a conversion between microwave and optical signals is slightly worse, mainly limited by the detection noise at the microwave frequency. It reaches about $10^{-16}$ at 1 s and in the range of $10^{-19}$ at $10^3$ s (Zhang *et al.*, 2010).

## 1.3 Laser frequency stabilization

The laser frequency is determined by the resonant mode of the laser optical cavity. Because of spontaneous emission and cavity optical length variations, the linewidth of a diode laser is typically in the megahertz region, while the linewidth of a fiber laser is in the kilohertz region. In order to reduce the laser frequency noise, the laser frequency can be stabilized to a more stable external reference.

There are several methods on laser frequency stabilization with various types of references, whose stability determines the stabilized laser frequency in the control bandwidth. I would like to introduce the techniques of laser frequency stabilization on a short ultra-stable Fabry-Perot (FP) cavity and on a long fiber-based interferometer.

### 1.3.1 Principle

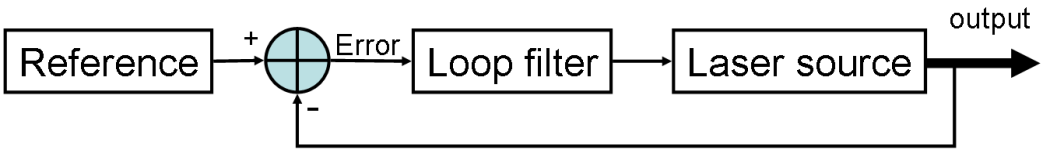


Figure 1.3: General scheme of a frequency stabilized laser.

Fig.1.3 shows the general scheme of a frequency stabilized laser. This scheme is a basic negative feedback control system. An error signal indicating the laser noise is obtained by comparing the laser signal with the external reference. And then, the loop filter corrects the laser frequency noise with negative feedback.

### 1.3.2 Cavity-stabilized laser

#### 1.3.2.1 A brief history

For the cavity-stabilized laser, the error signal was first obtained by detecting the transmission signal of the cavity (Barger *et al.*, 1973; White, 1965). This signal is proportional to the cavity stored power.

A higher finesse of the cavity is a more sensitive discriminator of the laser frequency. However, the time response of the transmitted signal is inversely proportional to the cavity finesse. Consequently, a higher cavity finesse leads to a slower response of the error signal and thus a bandwith reduction of the noise correction. With this approach, the slow response of a high finesse cavity limits the bandwidth of the laser frequency noise suppression.

In order to solve the problem, an alternative method makes use of a reflecting reference interferometer to produce the error signal (Wieman & Gilbert, 1982). This is a Michelson interferometer with a mirror and a FP cavity at the ends of two arms respectively. Therefore, it yields the phase difference between the incident and cavity-stored laser signals. Thus, the

response rate of this error signal is no longer limited by the cavity finesse, leading to a broader bandwidth for the laser frequency noise rejection.

A better approach is the Pound-Drever-Hall (PDH) method borrowed from the microwave cavity stabilization technique (Pound, 1946). It modulates the cavity incident signal with a frequency much higher than the cavity response (Drever *et al.*, 1983). Thus, the cavity stored energy will be roughly constant when the laser frequency is scanned over the cavity resonance. Cavity reflected signals are composed of resonant and off-resonant signals. Similar to Wieman's approach, this method detects the reflected signals from the cavity, therefore, produces the phase difference between the incident and cavity-stored signals. Consequently, the control bandwidth of the PDH method is also not limited by the cavity response. On the other hand, this method separates the compared laser signals in frequency rather than in space. As a result, this system has no additional noise induced by non-common optical pathes as using Wieman's approach. Furthermore, with the heterodyne detection in the PDH method, it is easier to obtain a low noise detection than with the homodyne detection of Wieman's approach. Consequently, the PDH method has become one of the most popular technique for laser frequency stabilization.

#### 1.3.2.2 The state-of-the-art

The lowest noise lasers are realized using laser frequency stabilization onto a short rigid ultra-stable high-finesse cavity with the PDH method (Alnis *et al.*, 2008; Ludlow *et al.*, 2007; Millo *et al.*, 2009b; Webster *et al.*, 2007, 2008; Young *et al.*, 1999). Thanks to improved coating techniques, the cavity finesse can reach a level of $10^6$, leading to a high signal-to-noise ratio for laser frequency noise detection. Consequently, the laser frequency noise is mainly limited by the length variation of the cavity. The best fractional frequency stability is in the range of $10^{-16}$ at 1 `s` integration time for a $10 - 20$ `cm` cavity. The laser frequency stability for short term is limited by the thermodynamic effect of the cavity mirrors, which is inversely proportional to the cavity length (Numata *et al.*, 2004). Extension of the cavity length can further improve the stability of the cavity.

On the other hand, the vibration sensitivity and temperature sensitivity has been studied both theoretically and experimentally (Alnis *et al.*, 2008; Legero *et al.*, 2010; Millo *et al.*, 2009b; Webster *et al.*, 2007). As a result, the requirement of the cavity vibrational and thermal isolations from the environment thus been made less critical, which reduces the complexity and cost of the whole system.

However, the ultra-stable cavity-stabilized laser requires alignment of free-space optical components and spatial mode matching. Moreover, this type of laser is expensive, bulky and fragile, and usually works at a fixed frequency.

### 1.3.3 Fiber-stabilized laser

Chen (1989) originally put forward and experimentally demonstrated stabilization of a laser frequency onto a fiber-based Mach-Zehnder interferometer. The tunable fiber-stabilized laser was first reported about 10 years later (Boggs *et al.*, 1998; Greiner *et al.*, 1998). This technique was later studied by additional groups (Barber *et al.*, 2010; Cliche *et al.*, 2006; Cranch, 2002; Crozatier *et al.*, 2006; Gorju *et al.*, 2007; Jiang *et al.*, 2010; Kéfélian *et al.*, 2009a; Roos *et al.*, 2009; Satyan *et al.*, 2009; Takahashi *et al.*, 2008).

Fiber-stabilized lasers have shown a few excellent features:

- Ultra-low frequency noise: Its level is comparable with that of an ultra-stable cavity-stabilized laser for Fourier frequencies higher than tens of hertz (Jiang *et al.*, 2010; Kéfélian *et al.*, 2009a).
- High linearity frequency sweep: The non-linear frequency error is less than 50 Hz peak-to-peak over a 600 MHz frequency span (Jiang *et al.*, 2010), and the fractional non-linearity reaches a sub-ppm (part per million) level over a $\sim$ 5 THz span (Roos *et al.*, 2009).
- Fast and wide range frequency tuning: The frequency scan rate is up to a few THz/s (Gorju *et al.*, 2007), and the sweep span is up to $\sim$ 5 THz (Roos *et al.*, 2009).

In addition, these lasers are cheap, simple, compact and robust. The frequency noise of these lasers is mainly limited by environmental noise, which can be improved using better isolation.

## 1.4 Current challenge: frequency dissemination

### 1.4.1 The need for ultra-stable frequency transfer

Ultra-stable frequency dissemination is necessary for many applications such as:

- Time and frequency metrology: Ultra-stable frequency standards are bulky and expensive devised that must be maintained by experts at metrology laboratories. The

fractional frequency uncertainty of optical clocks has progressed to the level of $10^{-17}$ at a few hours integration time. In order to precisely and accurately evaluate these clocks, frequency transfer links with a comparable or better stability have to be used for comparing their frequencies.

- Fundamental test of physics: With recently developed atomic clocks and optical comb synthesizers, frequency measurements can be used to test different models of fundamental physics to new boundaries. As an example, clock frequency comparisons allow us to test the stability of the fundamental constants. Clock frequencies are dependent on fundamental constants such as the fine-structure constant $\alpha$ (Fischer *et al.*, 2004; Fortier *et al.*, 2007; Marion *et al.*, 2003; Peik *et al.*, 2004) and the electron-to-proton mass ratio $\mu$ (Shelkovnikov *et al.*, 2008). High-sensitivity frequency measurements are also a key point for parity violation test in chiral molecules (Darquié *et al.*, 2010).

- Astro-physics: In order to improve resolution, distributed antennas are used in astronomical projets, including the very long baseline interferometer (VLBI), the NASA[1] deep space network (DSN) and the Atacama large millimeter/submillimeter array (ALMA). Stable time and frequency distribution must be applied for these systems to work properly.

- Particle physics: large particle accelerators, for instance the Deutsches Elektronen-synthrotron (DESY), the large Hadron Collider (LHC). These system need a precise phase control of the electromagnetic field for accelerating partial clusters and a precise synchronization for detection Wilcox *et al.* (2009).

Time and frequency transfers have a close relationship and can convert each other. The time transfer usually transmits a coded signal, while the frequency transfer transmits the frequency signal. With a ultra-low noise oscillator tracking the received time transfer signal at the remote end, a time transfer is equivalent to a frequency transfer within the tracking bandwidth. With a dead-time free frequency counter continuously recording the frequency transfer signal at the remote end, a frequency transfer is equal to a time transfer.

[1] the national aeronautics and space administration of the United States

### 1.4.2 Satellite-based link

#### 1.4.2.1 Traditional microwave link

The satellite-based transmission is the most widely used method for the time and frequency transfer. These links are mainly based on the two-way satellite time and frequency transfer system (TWSTFT) or the global positioning system (GPS).

The TWSTFT system typically uses communication satellites placed in geosynchronous orbits with an altitude of $\sim$ 35800 km. The link is composed of an up-link and a down-link with carrier frequencies of 14 GHz and 11 GHz respectively. The GPS system has 24 satellites in $\sim$ 20200 km orbits. These satellites provide two down-link signals with carrier frequencies of 1575 MHz and 1228 MHz. The transmission instability is at the level of $10^{-15}$ at one-day integration time with the TWSTFT or GPS carrier-phase transfer technique. The standard GPS technique is capable of giving a similar quality of data by averaging over two days or longer (Bauch *et al.*, 2006).

#### 1.4.2.2 Microwave link for ACES

The link of ACES is a dedicated two-way microwave link, including two down-links and one up-link. The satellite for ACES project will be placed in a 400 km orbit. The carrier frequencies of one down-link and the up-link are in Ku-band (14.7 GHz and 13.5 GHz respectively), which is similar to the TWSTFT system. However, it has an extra down-link in S-band (2.2 GHz), in order to determine the total electron content (TEC) and correct for the ionosphere time delay. Furthermore, a higher coding rate (100 Mchip/s) is used in this link than that of the TWSTFT and GPS systems, allowing a better time measurement resolution. This microwave link can compare on board clock and earth-based clocks with a time resolution of 7 ps per day and 23 ps at 10 days, corresponding to $\sim 10^{-16}$ and $\sim 3 \times 10^{-17}$ (Cacciapuoti & Salomon, 2009; Cacciapuoti *et al.*, 2007; Laurent *et al.*, 2008).

#### 1.4.2.3 Free-space optical link

One free-space optical link T2L2 (transfer time by laser link) system has been flying onboard JASON-2 satellite in a 1336 km orbit since June 2008. By using very short light pulses, this link realizes a synchronization between the ground clocks and space clock of the satellite. Time transfer between several remote ground clocks is therefore obtained through these individual space-ground time transfers. A common view mode can be realized for comparing

ground clocks within 5000 km, while a non-common view mode has to be used for longer distance time comparisons. The evaluation of T2L2 time transfer capability is presently ongoing, and it offers a prospect to reach a time resolution of $\sim 10$ ps after one day averaging for clock comparisons in common view (Cacciapuoti & Salomon, 2009; Samain *et al.*, 2007, 2009). It corresponds to a fractional frequency instability of $\sim 10^{-16}$ at one day integration time.

Another type of free-space optical link transfers directly the optical frequency with a continuous-wave (CW) laser signal. Djerroud *et al.* (2010) reports such a 5 km link between a telescope and a ground target with a fractional frequency instability of $10^{-17}$ at hundreds second integration time.

However, the performance of the free-space optical links strongly depends on the location and the atmosphere conditions.

## 1.5 Fiber links

The fractional frequency stability of best atomic clocks has already reached the level of $10^{-16}$ or better at a few hours integration time. Clearly, the current satellite-based links do not match the requirement of transferring these clocks' frequencies.

Thanks to the improvement of fibre fabrication technique and the development of the commercial communication system, fibre networks show features of low noise, low loss, and are accessible almost everywhere in the world. Consequently, fibre links become a very appropriate candidate for transferring ultra-stable frequency signals (Lutes, 1980).

There are three types of frequency transfer techniques using fiber (Foreman *et al.*, 2007a):

- ***The microwave frequency optical link*** uses a CW laser carrier to transfer an amplitude modulation frequency on the laser signal (Calhoun *et al.*, 2000; Daussy *et al.*, 2005; Kumagai *et al.*, 2009; Lutes, 1980; Narbonneau *et al.*, 2006; Ye *et al.*, 2003). The instability of the link can be improved by increasing the modulation frequency to reduce the detection noise effect and scrambling the polarization to suppress the polarization mode dispersion effect. With these improvements, a 86 km telecom urban link exhibits a fractional instability of $\sim 10^{-15}$ at 1 s integration time, and below $10^{-18}$ at one day (Lopez *et al.*, 2008, 2010a).

- ***The optical comb link*** transfers the mode-locked laser signal over the fiber networks (Holman *et al.*, 2004; Kim *et al.*, 2008; Marra *et al.*, 2010). This link transfers many optical frequencies in a single operation. However, the power in each optical frequency is very weak, therefore, limiting the transmission distance. Consequently, the transferred frequency is usually just the repetition frequency and its harmonics for long-distance transmission. The fiber dispersion should be compensated, so as to avoid any broadening of the laser pulse. Recently, a 50 km spooled optical fiber link showed a fractional instability of a few $10^{-15}/\tau$ for integration times $\tau$ of $1-20$ s (Marra *et al.*, 2010). The spectrum of this pulse laser is a 90-nm-wide comb centered at 1.56 $\mu$m.

- ***The optical carrier link*** presents the best frequency stability among these frequency transmission techniques. It has been developed by several research groups (Foreman *et al.*, 2007b; Grosche *et al.*, 2009; Hong *et al.*, 2009; Jiang *et al.*, 2008; Kéfélian *et al.*, 2009b; Lopez *et al.*, 2010b; Ma *et al.*, 1994; Musha *et al.*, 2008; Newbury *et al.*, 2007; Terra *et al.*, 2009, 2010; Williams *et al.*, 2008). Almost all of these optical links with distances of $100-450$ km show a fractional instability in the range of $10^{-19}$ with rather short integration time (a few hours).

Note that a link can combine the above cited techniques. For instance, Wilcox *et al.* (2009) describes a link, whose transfer frequency is in the microwave domain, whereas the noise compensation is based on the measurement of the optical carrier phase.

## 1.6 Subject of the thesis

This thesis is dedicated to the development of continental distance frequency transfer links with an instability of $\leq 10^{-18}$ for one-day integration. The long-term objective is to connect all national laboratories metrology laboratories as well as some physics laboratories in Europe. These physics laboratories (e.g. LPL, LKB...) would benefit from having access to the best remote locale clock to perform ultra-high sensitivity tests of fundamental physics. We adopt the approach of the optical carrier link.

This thesis contains following steps towards this objective:

1. Develop ultra-stable cavity-stabilized lasers to be the optical source for the link experiments. These laser sources exhibit frequency fluctuations less than 1 Hz for $1-10$

s measurements. The stability is mainly limited by the thermodynamic effect of the reference cavity.

2. Study and realize ultra-stable tunable fiber-stabilized laser systems. These lasers have a flexible frequency tunability with ultra-low frequency noise comparable to the cavity-stabilized laser for Fourier frequency higher than a few tens of Hertz. This type of laser source can be used in the repeater station of the optical link and other for applications (e.g. free space optical link).

3. Transfer the ultra-stable optical signal over $100 - 200$ km via dedicated fiber networks.

4. Transfer the ultra-stable optical signal via public networks on a dedicated channel.

5. Extend the link to 300 km with a cascaded approach.

## 1.7 Outline

This thesis contains five chapters:

- Chapter 1: Introduction.
- Chapter 2: Description and discussion of the home-made ultra-stable cavity-stabilized laser.
- Chapter 3: Presentation of the fiber-stabilized laser.
- Chapter 4: Optical link with the description of the principle and a few experiments of the optical carrier frequency transfer over $86 - 300$ km.
- Chapter 5: Conclusions and future work.

# Chapter 2

# Ultra-stable cavity-stabilized laser

This chapter describes the development of a sub-Hz linewidth 1542 nm wavelength laser source by stabilizing the laser frequency onto a cavity with the Pound-Drever-Hall (PDH) method (Drever *et al.*, 1983).

With the PDH method, the high finesse cavity determines the locked laser frequency, because the laser frequency noise and other technical noises are suppressed below the cavity noise by a high bandwidth control. The noise sensitivities of the high finesse cavity (due to temperature fluctuations, mechanical vibrations, thermal noise etc.) become the limitation of the laser frequency noise. Effects of the cavity's material (Callen & Greene, 1952; Greene & Callen, 1952; Numata *et al.*, 2004), shape and mounting (Millo *et al.*, 2009b; Notcutt *et al.*, 2005; Webster *et al.*, 2007) were studied and understood. As a result, many sub-Hz linewidth laser sources have been developed since late 1990s (Millo *et al.*, 2009b; Notcutt *et al.*, 2005; Seel *et al.*, 1997; Webster *et al.*, 2007; Young *et al.*, 1999). The lowest frequency noise lasers are realized with an ultra-stable cavity up to now, even though an alternative approach to the ultra-low noise laser are explored (Meiser *et al.*, 2009).

We developed two cavity-stabilized sources with the PDH method for ultra-stable frequency transfer experiments (Jiang *et al.*, 2008; Kéfélian *et al.*, 2009b; Lopez *et al.*, 2010b). These lasers also have been used in experiments of ultra-stable microwave frequency generation (Millo *et al.*, 2009a,c) and evaluation of fiber-stabilized lasers (Jiang *et al.*, 2010; Kéfélian *et al.*, 2009a). Our ultra-stable lasers present frequency noise and stability at the state-of-the-art level.

This chapter briefly introduces the principle of the PDH locking. After that, it shows the experimental setup, and discusses design considerations and various noise contributions

of the stabilization system. Finally, it gives a detailed operational process and experimental results of these developed lasers.

## 2.1 Principle of the PDH method

This part only gives a brief introduction on the PDH method. Detailed explanation on this method can be found in several papers (Black, 2001; Day *et al.*, 1992; Zhu & Hall, 1993).

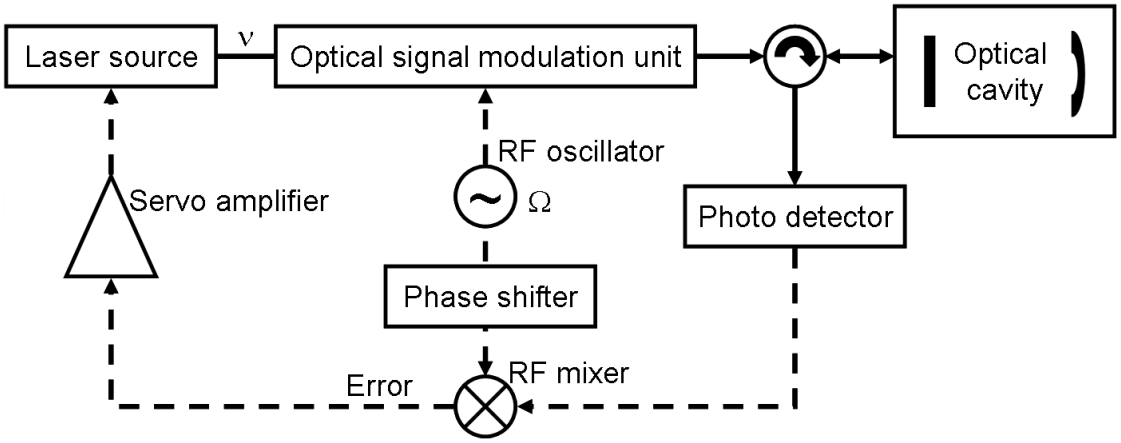


Figure 2.1: Scheme of the PDH method.

Fig.2.1 shows the basic layout of the PDH locking. Optical signals are drawn in solid line, while other signals are drawn in dashed line. A $\nu$ frequency laser signal is phase/frequency modulated by a radio-frequency (RF) signal at a frequency of $\frac{\Omega}{2\pi}$ ($\gg \Delta\nu_{cavity}$), where $\Delta\nu_{cavity}$ is the cavity resonance linewidth [1]. Then, the input of the Fabry-Perot cavity contains optical signals at frequencies of $\nu - \frac{\Omega}{2\pi}$, $\nu$ and $\nu + \frac{\Omega}{2\pi}$. When the carrier frequency $\nu$ is close to a resonant frequency of the cavity, the reflected carrier wave can be regarded as a combination of the reflected incident signal and the backward leakage of cavity-stored signal. We assume that the optical carrier signal is coupled to a cavity mode. For high frequency laser frequency fluctuation, The phase variation of the leakage signal at the resonant frequency does not follow that of the incident signal at high frequencies; while the phase variation of reflected sideband signals does, because the cavity directly reflects these non-resonant signals; thus, the difference between them indicates laser frequency fluctuations $\delta\nu$ without degradation

[1] the linewidth is the full-width of half-maximum transmission.

due to a slow frequency response of the cavity. The corresponding error signal is obtained by demodulating the beat-note signal between the carrier and sidebands. The RF phase shifter is required to set the phase relationship between the demodulation and detected signals to be in phase, leading to a maximum demodulation efficiency. The slope of the error signal with respect to the laser frequency fluctuation is given by Black (2001):

$$D = \frac{8\sqrt{P_c P_s}}{\Delta\nu_{cavity}}, \tag{2.1}$$

where $P_c$ is the optical power in carrier, $P_s$ is the optical power in one sideband, it has been assumed that the carrier transmission contrast, the photo-detector's quantum efficiency and the demodulation efficiency are unity. The principle of this method is to use the cavity-stored signal as reference to detect the phase/frequency noise of laser signal, which is not at the cavity resonant frequency. In fact, a sideband signal instead of the carrier one can be stabilized onto a cavity resonant frequency (Livas *et al.*, 2009). The cost is that the detection noise effect is higher when the same optical signals are used. However, this effect usually can be reduced by using a higher incident optical power.

The laser frequency can be stabilized onto any cavity mode. However, for a flat-concave Fabry-Perot cavity, a higher order mode may correspond to a broader mode linewidth and a lower frequency discriminating efficiency due to the diffraction effect (Kleckner *et al.*, 2010), resulting in stronger technical noise effects. Furthermore, the TEM00 is the most robust mode in terms of spatial coupling. As a result, the TEM00 mode is typically chosen for laser frequency stabilization. It is worth noting that a high order mode coupling corresponds to a bigger beam size, which may average down the thermodynamic noise effect.

## 2.2 Ultra-stable Fabry-Perot cavity

In this section, I introduce basic concepts on the Fabry-Perot (FP) cavity, and describe the ultra-stable cavity, including the shape, material, mounting and noise effects.

### 2.2.1 Fabry-perot cavity

A FP cavity, also called a FP interferometer, is typically made of a spacer and two highly reflecting mirrors. Its resonant effect leads to frequency-dependent transmission and reflection. In fact, the cavity length $L$ and the mirror reflectance $R = \sqrt{R_{mirror\_1} \times R_{mirror\_2}}$ determine the cavity parameters: (Lipson *et al.*, 1995)

- The **f**ree **s**pectral **r**ange (FSR) of the cavity is the frequency span between two successive TEM00[1] modes given by

$$\Delta\nu_{FSR} = c/2L, \tag{2.2}$$

where $c$ is the speed of light.

- The optical intensity decay time of the cavity $\tau$ is given by

$$\tau \approx |L \ln R/c| \approx \frac{L}{c(1-R)}, \tag{2.3}$$

where $1 - R$ is much less than 1.

- The mode linewidth $\Delta\nu_{cavity}$ is the full-width of half-maximum transmission. It is given by

$$\Delta\nu_{cavity} = \frac{1}{2\pi\tau}. \tag{2.4}$$

- The cavity finesse $F$ is the ratio of the FSR to the mode linewidth. It is only determined by the mirror reflectance $R$, and given by

$$F = \Delta\nu_{FSR}/\Delta\nu_{cavity} \approx \pi/(1-R) \approx \pi\tau c/L \tag{2.5}$$

- The quality factor of the cavity is the ratio of the resonant frequency to the mode linewidth

$$Q = \nu_0/\Delta\nu_{cavity} \approx 2\pi\tau\nu_0, \tag{2.6}$$

where $\nu_0$ is the cavity resonant frequency ($\sim 2\times10^{14}$ `Hz`). One has $Q \approx \nu_0\delta\phi/\delta\nu$, where $\delta\phi$ is the variation of a small phase difference between the cavity backward leakage signal and the incident signal, $\delta\nu$ is the laser frequency fluctuation around the cavity resonance.

### 2.2.2 The ultra-stable cavity system

The reference cavity is a 10 `cm` FP interferometer with a pair of flat-concave highly reflecting mirrors. The radius of the concave mirror is 50 `cm`. The specified finesse of the cavity is better than $2\times10^5$, corresponding to $\Delta\nu_{cavity} < 8$ `kHz`. Having a low coefficient of thermal expansion (CTE) is essential to the ultra-stable cavity. Both spacer and mirror substrate of our cavity are made of ultra low expansion glass (ULE), whose CTE is typically as low as

[1] Usually, we stabilize the laser frequency onto the TEM00 mode of the cavity.

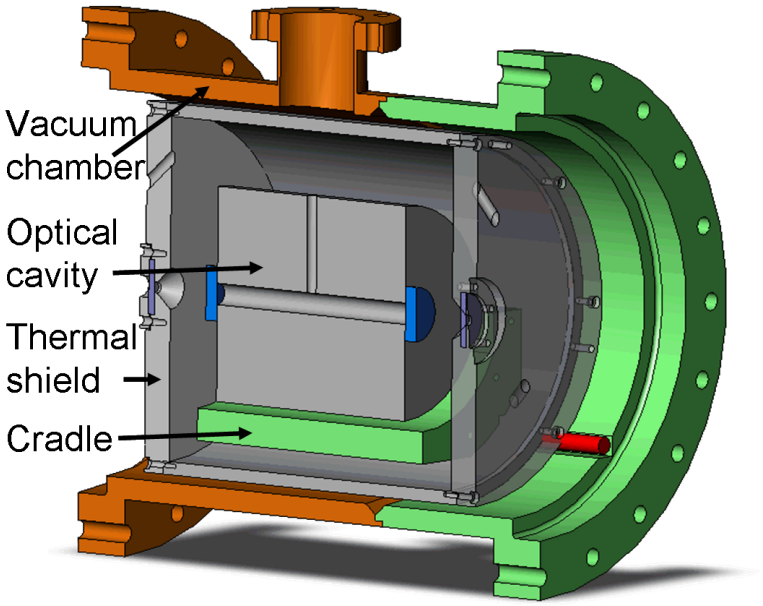


Figure 2.2: Scheme of the ultra-stable cavity.

10 parts per billion (ppb) per Kevin. Indeed, ULE is a titania-doped silicate glass that has a specified thermal expansion minimum at some temperature $Tc$ around room temperature. With sufficient thermal isolation and controlling the operation temperature to be about $Tc$, the drift rate of this type of cavity can be reduced to $< 2 \times 10^{-16}$ /s (Alnis *et al.*, 2008; Webster *et al.*, 2008). The cavity is supported by a cradle inside one layer thermal shield and a vacuum chamber (see Fig.2.2). The whole reference cavity system is mounted on a bread board, which is laid on a commercial vibration isolation platform. All of them are enclosed with a wooden box with acoustic damping foams. The platform and the wooden box provides an acoustic noise attenuation of $10^2 - 10^3$ in amplitude.

### 2.2.3 Noise effects on the cavity system

There are various noise effects on the laser frequency induced by: thermodynamic noise of the cavity, vibration, laser power variation, pressure fluctuation and temperature fluctuation. The cavity system design is based on the analyses of these effects. It is worth noting that these laser sources were designed for the optical link experiment with best performance laser sources. Thus, we trade somewhat off the performance for simplicity.

#### 2.2.3.1 Thermodynamic noise of the cavity

The dominant limitation to the laser frequency noise is usually the thermodynamic effect of the spacer, the mirror substrate and the mirror coating. The thermodynamic effect on laser frequency can be evaluated, based on the fluctuation dissipation theorem (FDT) (Callen & Greene, 1952; Greene & Callen, 1952). The induced laser frequency noise power spectral density (PSD) is given by Numata *et al.* (2004)

$$\begin{cases} S_{\nu-spacer}(f) = \frac{\nu^2}{L}\frac{4k_BT}{2\pi f}\frac{1}{3\pi R_s^2 E}\phi_{spacer} \\ S_{\nu-mirror}(f) = \frac{\nu^2}{L^2}\frac{4k_BT}{2\pi f}\frac{1-\sigma^2}{\sqrt{\pi}E\omega_0}\phi_{sub}\left(1+\frac{2}{\sqrt{\pi}}\frac{1-2\sigma}{1-\sigma}\frac{\phi_{coat}}{\phi_{sub}}\frac{d}{\omega_0}\right) \end{cases}, \tag{2.7}$$

where $R_s$ is the spacer radius 10 $\mathtt{cm}$, $L$ is the spacer length 10 $\mathtt{cm}$, $T$ is the temperature $\sim$ 300 $\mathtt{K}$, $E$ is the Young's modulus $6.8 \times 10^{10}$ $\mathtt{Pa}$, $\sigma$ is Poisson's ratio 0.18 (ULE), $\phi$ is the mechanical loss of materials $4 \times 10^{-4}$ for the coating and $\sim 1.7 \times 10^{-5}$ for ULE glass (in power), $\omega_0$ is the beam radius $\sim$ 0.33 $\mathtt{mm}$, $d$ is the coating thickness 2 $\mu\mathtt{m}$. For our cavities, the thermodynamic effect due to the mirror coatings is $\sim 2\times10^{-2}/f$ $\mathtt{Hz}^2/\mathtt{Hz}$ which limits the laser frequency noise for low Fourier frequencies, while the ULE spacer induces a thermodynamic noise of $\sim 3 \times 10^{-5}/f$ $\mathtt{Hz}^2/\mathtt{Hz}$. By using a lower loss material as the mirror substrate (e.g. fused silica), this limitation can be reduced (by a factor of $\sim$ 4). However, the fused silica mirror has a CTE about 2 orders of magnitude higher than that of ULE glass, requiring a much better thermal isolation to maintain the same rate of the cavity temperature drift. Actually, it is possible to combine the low thermodynamic effect of a fused silica mirror and the low CTE of an ULE mirror by adding an ULE ring on the silicon mirror (Legero *et al.*, 2010).

#### 2.2.3.2 Vibration sensitivity

The vibration noise leads to the cavity deformation, resulting in excess laser frequency noise. Usually, the ultra-stable cavity system is isolated from this noise. However, use of a lower vibration sensitivity cavity can decrease the vibration isolation requirement. Consequently, it simplifies the isolation system. We design our cavity [see Fig.2.3 and Millo *et al.* (2009b)] by starting from the idea of symmetry place and using an approach based on finite element analysis (Alnis *et al.*, 2008; Chen *et al.*, 2006; Nazarova *et al.*, 2006; Notcutt *et al.*, 2005; Webster *et al.*, 2007). This cavity (see Fig.2.3 and Fig.2.4) is mounted on an aluminum cradle with 4 Viton pads. The first point of this design is a minimization of the vibration

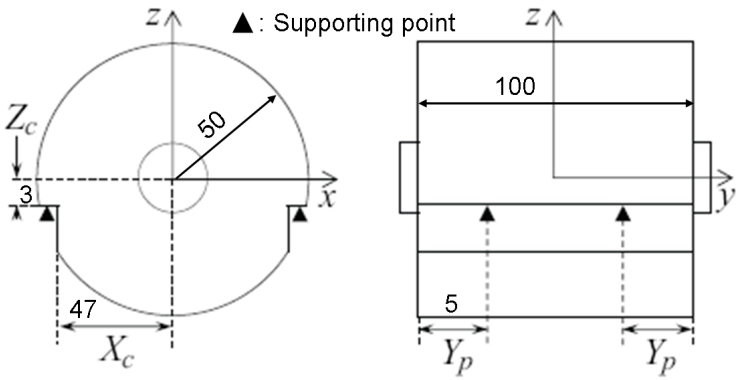


Figure 2.3: Drawing of the cavity (in mm).

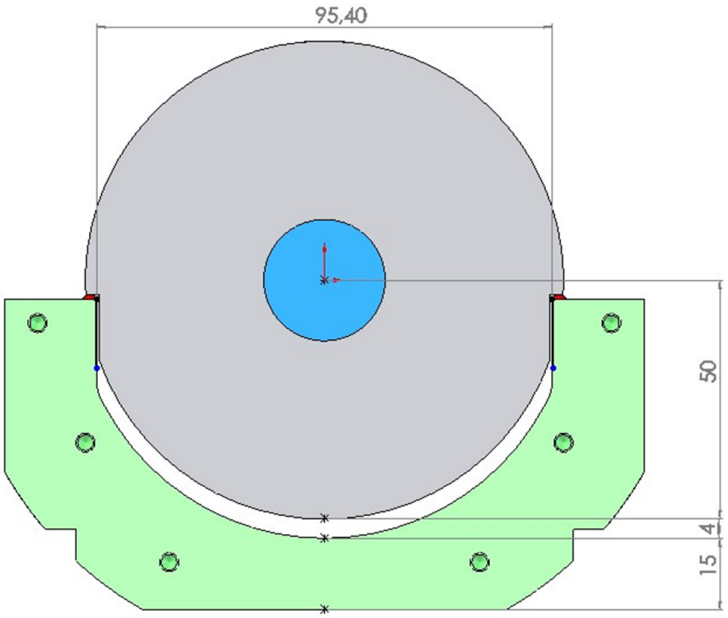


Figure 2.4: Drawing of the cavity mounting (in mm): cavity support (green), ULE cavity spacer (grey), ULE mirror (blue).

sensitivities in all directions. The second point is a low vibration sensitivity variation with respect to a supporting position change, requiring a comparably low mounting accuracy. Experimentally, a cavity of the same configuration shows vibration sensitivities ($\frac{\delta l}{l}/a$) to be $5 \times 10^{-12}$ /ms$^{-2}$ (z direction), $10^{-11}$ /ms$^{-2}$ (y direction) and $3 \times 10^{-12}$ /ms$^{-2}$ (x direction) (Millo *et al.*, 2009b). The magnitude of these vibration sensitivities is at the state-of-the-art level.

#### 2.2.3.3 Laser amplitude noise effect

An optical power fluctuation results in a little resonant frequency fluctuation of the cavity. This phenomenon may be caused by a coating absorption effect (Young *et al.*, 1999) or a radiation pressure effect (Caves, 1980; Dorsel *et al.*, 1983). Whatever, this effect should be proportional to the cavity circulating power for short terms. Thus, it can be approximated as

$$C(f) = \frac{\delta\nu(f)}{\delta P(f)} = e^{-\frac{f}{\Delta\nu_{cavity}}} \frac{C_p F \nu}{L} \approx \frac{C_p F \nu}{L}, \text{ for } f \ll \Delta\nu_{cavity}, \tag{2.8}$$

where $f$ is the Fourier frequency, $\delta\nu$ is the variation of the laser frequency, $\delta P$ is the variation of transmission power, $C_p$ is the conversion parameter mainly determined by the features of the mirror and laser beam size, $\nu$ is the laser frequency, $F$ is the cavity finesse, $L$ is the cavity length. In Young *et al.* (1999), this effect is about 1 Hz/$\mu$W of incident power. Their cavity is made of the same materials as ours. According to Eq.2.8, we determine the parameter $C_p$ to be $\frac{incident\ power}{transmission\ power} 3 \times 10^{-21}\ \frac{\text{m}}{\mu\text{W}}$.

#### 2.2.3.4 Pressure fluctuation effect

Thanks to the low CTE of the spacer and mirrors (made of ULE) decreasing the thermal isolation requirements, we use only one layer thermal shield. Consequently, the volume of the chamber is small ($\sim$ 10 liters). A $\frac{1}{4}$ liter/s ion pump is sufficient to maintain the vacuum to be a few $10^{-6}$ Pa. Thus, the effect of vacuum fluctuations is negligible in our case.

Another interesting effect is small scale refractive index fluctuation, which is usually negligible. The motion of gas particles leads to a laser frequency noise **p**ower **s**pectral **d**ensity (PSD) given by (Saulson, 1994)

$$S_\nu(f) = 2^5 \pi^{5/2} \frac{\alpha_{chem}^2 c^2}{\lambda^{5/2} L^{3/2}} \frac{\rho}{\overline{v}} e^{-\sqrt{8\pi\lambda L} f/\overline{v}}\ \text{Hz}^2/\text{Hz}, \tag{2.9}$$

where $f$ is the Fourier frequency, $\rho$ the gas particle number in $\mathrm{m}^{-3}$, $\overline{v}$ the mean gas particle speed in m/s, $c$ the light speed in m/s, $\lambda$ the laser wavelength in meters and $\alpha_{chem}$ the gas particle polarizability in units of volume (typically $\sim 10^{-30}$ $\mathrm{m}^3$). In practice, the laser frequency noise induced by the gas particles motion is much below the technical vacuum fluctuations, which are relevant to the variations of temperature and pressure. This induced noise is independent of the cavity length. Experimentally, a $\sim 10^{-4}$ Pa vacuum level is sufficient to realize a sub-Hz linewidth laser (Ludlow *et al.*, 2007).

#### 2.2.3.5 Temperature fluctuation effect

The temperature fluctuation degrades the cavity stability. In order to reduce the temperature fluctuation effect, we isolate the cavity with the vacuum system and an acoustic damping box.

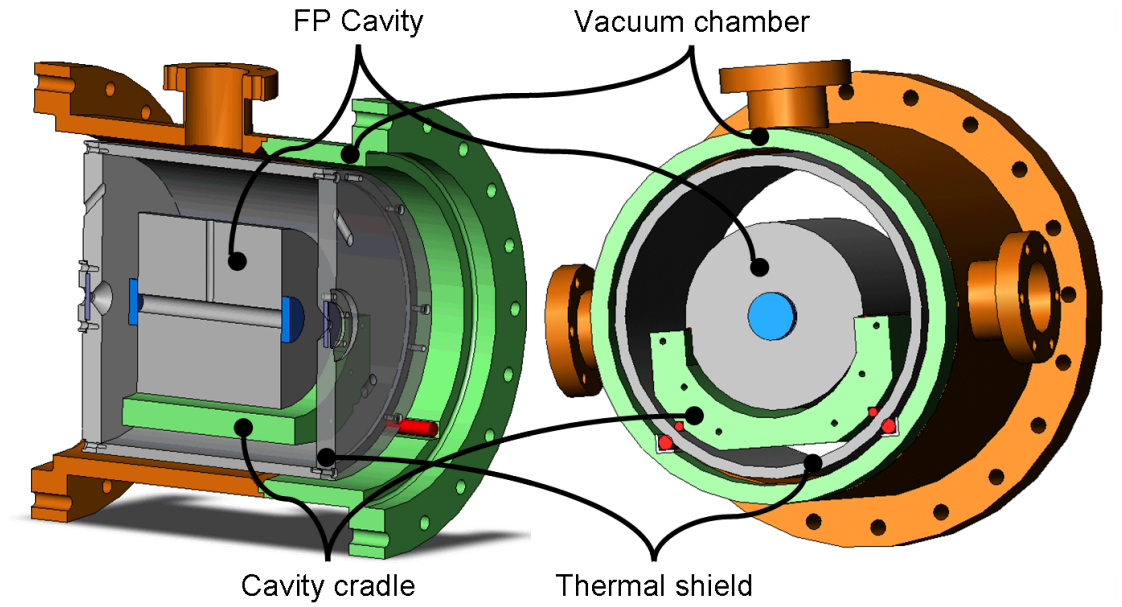


Figure 2.5: Scheme of the vacuum system.

To also reduce radiative heating, we use a thermal shield. Fig.2.5 shows the vacuum system scheme, where the thermal shield is used to enhance the thermal isolation. The thermal shield is made of polished aluminum with inner and outer gold coatings, because gold coatings give high reflectance over a broad spectrum span. The mounting configuration

is rather simple. We fix four pieces of machined Teflon into the vacuum chamber with vacuum glue, in order to block four short Viton rods ($\sim$ 1.5 cm). In succession, we lay the thermal shield on the Viton rods. After that, we put the cradle with the cavity in the shield. Here, four little Viton rods are used to support the cradle, in order to reduce the thermal conductivity.

The radiation power is given by Stefan-Boltzmann law

$$P = A\varepsilon\sigma T^4, \tag{2.10}$$

where $A$ is the absorbtion area in $\mathrm{m}^2$, $\varepsilon$ is the emissivity, $\sigma$ is Stefan-Boltzmann constant $5.67 \times 10^{-8}\ \frac{\mathrm{W}}{\mathrm{m}^2\mathrm{K}^4}$, $T$ is the temperature in Kelvin. Thus, the temperature time constant can be evaluated as

$$\tau = \frac{C_g m}{dP/dT} \approx \frac{C_g m(A_1\varepsilon_1 + A_2\varepsilon_2)}{3T^3 A_1 A_2 \varepsilon_1 \varepsilon_2 \sigma}, \tag{2.11}$$

where $C_g$ is the heat capacity in $\frac{\mathrm{J}}{\mathrm{gK}}$ and $m$ is the mass in g. Assuming an emissivity of 0.02 for the shield, and a high emissivity ($\approx 1$) of the vacuum chamber and the cavity, the time constants due to radiative coupling are estimated to be $2 \times 10^5$ s from the vacuum chamber to the shield and $2 \times 10^5$ s from the shield to the cavity. The thermal attenuation is approximate to be the time constant $\tau$ multiplied by $2\pi f$, where $f$ ($\ll \tau$) is the temperature fluctuation frequency. In our laboratory, the temperature control system has a $\sim$ 1 degree peak-to-peak oscillation at $\sim$ 1/400 Hz. As for this signal, the total thermal attenuation through this path is about $\sim 10^7$. Thus, its radiative coupling effect is about 0.2 Hz peak-to-peak laser frequency fluctuation. However, this isolation is less efficient for lower frequency temperature variation. In addition, the acoustic-damping box also provides a one-order thermal isolation with a time constant of $\sim$ 1 day. Note that the conduction path also degrades the thermal isolation.

Usually, the optical signal coupled into the system is in the level of $\mu$W. A fraction of this signal is absorbed by the mirrors of the cavity and windows of the vacuum system, whereas this absorbtion rate is much below the exchanging rate of the thermal energy due to the black-body radiation (see Eq.2.10). Thus, we neglect the effect of the laser signal absorption on the cavity temperature.

## 2.3 Experimental setup

This section introduces the setup of the laser frequency stabilization system, which includes the optical system and the electronic system.

### 2.3.1 Optical system

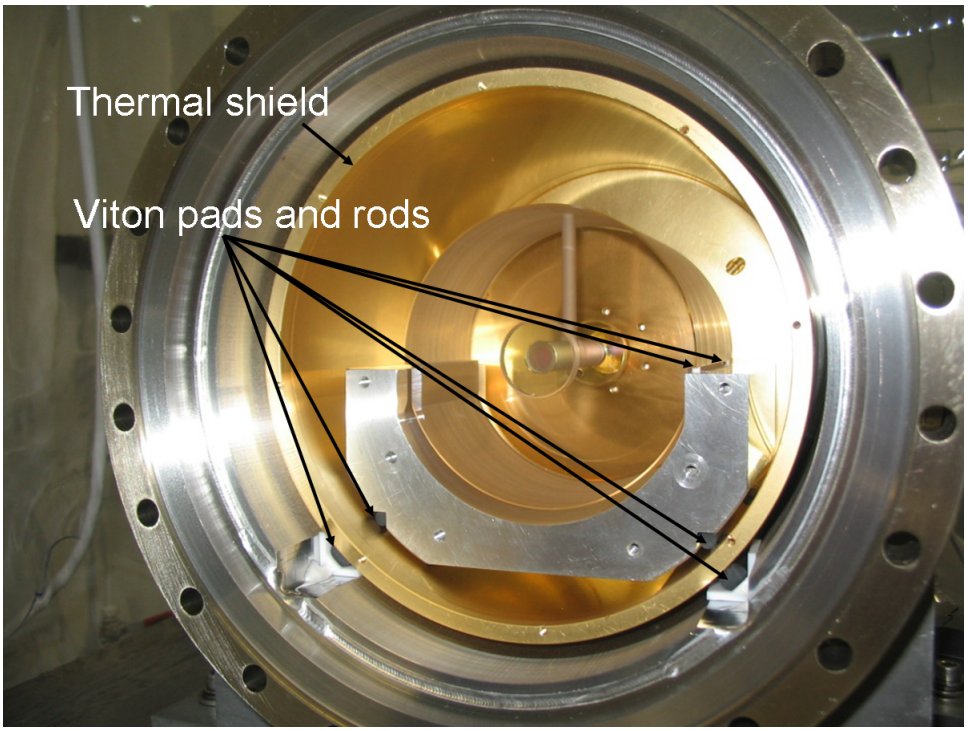


Figure 2.6: Picture of the cavity in the vacuum chamber.

Fig.2.6 shows the picture of the cavity system, which is the key element of the laser frequency stabilization.

The stabilized laser is a 1542 nm commercial fiber laser (Koheras Inc. 100 mW). The linewidth of the free-running laser is less than 1 kHz for a 120 $\mu$s measurement. This laser has two ports for laser frequency control: a temperature control port and a piezo-electric transducer (PZT) control port. Their responses are slow, limiting the control bandwidth to be less than tens of kilo hertz. In order to broaden the control bandwidth, we insert an free-space acousto-optic modulator (AOM) into the optical path to correct the laser frequency. The modulation delay time of this AOM is about 1 $\mu$s, which limits the control bandwidth to be less than 1 MHz.

Fig.2.7 shows the scheme of the optical system. The fiber laser signal is coupled to free space via the input optical collimator. Note that the fiber connecting the input collimator and the output of fiber laser is a polarization-maintaining fiber. The polarization of the laser

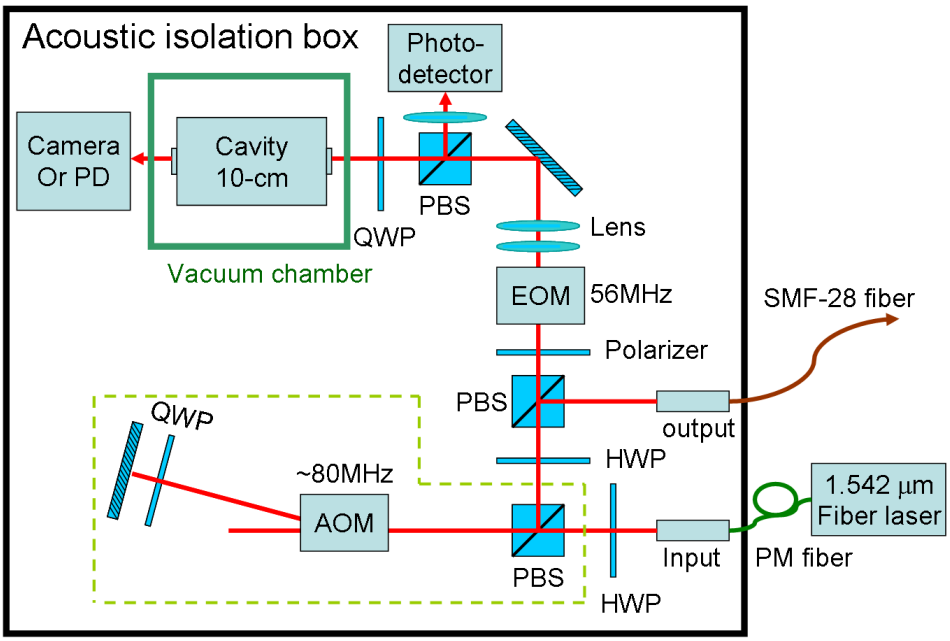


Figure 2.7: Scheme of the optical system (PD: photodiode; PBS: polarization beamsplitter cube, QWP: quarter-wave plate, HWP: half-wave plate, AOM: acousto-optic modulator, EOM: electro-optic modulator, PM: polarization maintaining, SMF: single mode fiber).

signal is adjusted to align to the first polarization beam-splitter (PBS) after passing through a half-wave plate (HWP). Most of the optical signal passes through this PBS toward the AOM, while nearly all the laser signal, which passes twice the AOM and the quarter-wave plate, is reflected to the second PBS. Such an AOM double-pass configuration (in the dashed frame) well maintains the spatial alignment when the AOM frequency is tuned (Donley *et al.*, 2005). The second PBS splits the laser signal into two parts. One part is sent to the cavity for laser frequency stabilization; while the other is coupled out to be the stabilized laser output. The power ratio between two parts is set by using a HWP in front of the second PBS. After that, we modulate the phase of the laser signal for stabilization with an electro-optic modulator (EOM). Unfortunately, the phase modulation is always accompanied with some level of random amplitude modulation (RAM). The RAM leads to a disturbance on the error signal, resulting in an additional laser frequency noise. This noise effect is sensitive to the laser polarization state. Thus, a high quality polarizer is used to minimize the RAM. After that, the laser signal is aligned to the cavity. The last PBS and QWP are applied to

guide the cavity reflected signal to an avalanche photodiode, which produces the beat-note signal of the optical carrier and sidebands.

Note that the incident surface of all optical components are tilted with respect to the incident wave to avoid stray FP interferometer in the system. I optimize the laser beam profile to match with the TEM00 mode by using lenses. The mode can be verified by monitoring the beam profile of cavity transmission signal with a camera.

### 2.3.2 Electronic system

The electronic system mainly includes RF parts for modulation and demodulation optical signals and a loop filter for generating the laser frequency control signals.

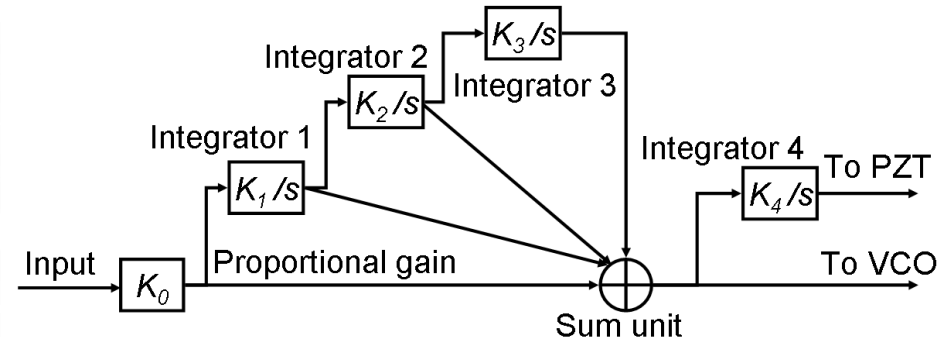


Figure 2.8: Scheme of the loop filter, $K_0 \sim K_4$ are independently adjustable gains.

We use a 56 MHz quartz oscillator to produce simply the modulation and demodulation RF signals. The RF phase shifter (see Fig.2.1) is a coaxial cable matched in length. The input of the loop filter (i.e. servo amplifier in Fig.2.1) is the demodulated error signal. Its scheme is shown in Fig.2.8. The sum output of the proportional gain and first three integrators controls a voltage control oscillator (VCO), which drives the AOM, leading to a fast laser frequency correction. The loop filter itself has a response bandwidth of about 2 MHz; while the maximum loop control bandwidth is about 600 kHz mainly due to the limitation of the AOM control delay. The AOM can only be tuned in a frequency range of $\sim$ 2 MHz, which is not enough to compensate the frequency drift of the fiber laser. To enlarge the frequency control range, we also control the laser frequency via the PZT stretcher port with a slow integration signal of the VCO control voltage. In this way, the laser frequency can be corrected in a range of $>$ 1 GHz. Consequently, the laser can be stabilized for months without any adjustment.

The detection noise of the photo-detector includes the shot noise and the Johnson noise. The PSD of detection shot noise is given by (Black, 2001)

$$S_e = 4h\nu P_s, \tag{2.12}$$

where $P_s$ is the optical power in one sideband, it has been assumed that the photo-detector's quantum efficiency is unity. Eq.2.1) and Eq.2.12 give the laser frequency noise PSD (Black, 2001)

$$S_\nu(f) = \frac{h\nu\Delta\nu^2_{cavity}}{16P_c}\ \mathtt{Hz}^2/\mathtt{Hz}, \tag{2.13}$$

where $h$ is the Planck constant. When a low incident optical power is used, the shot noise effect could be weaker than the Johnson noise effect, which is inversely proportional to the square of the incident power. For an ultra high finesse cavity ($\sim 10^6$), use of a few $\mu$W carrier and $\sim 1$ $\mu$W sidebands is usually sufficient to maintain the detection noise effect negligible. The criterion is that the laser frequency noise is independent of the incident optical power variation. In our case, the detection noise effect gets obvious only if the incident optical power is less than $\sim 0.1$ $\mu$W [$S_\nu(f) \sim 0.01$ $\mathtt{Hz}^2/\mathtt{Hz}$].

## 2.4 Operational process

The PDH method does not produce the error signal, if the laser is not coupled to the cavity resonance. It is difficult to monitor and optimize mode couplings when the laser linewidth is much larger than the cavity linewidth. In order to decrease the operation difficulty, most of the research groups adopt a pre-stabilization stage (Ludlow *et al.*, 2007; Notcutt *et al.*, 2005; Schoof *et al.*, 2001; Young *et al.*, 1999), even though it is not essential (Duan & Gibble, 2005). Our laser source has a linewidth of a few kHz, which is comparable to the linewidth of the cavity resonance. Thus, no pre-stabilization stage is required. We develop our system with following steps:

- Calculate the laser beam spatial intensity profile for the cavity mode coupling and design the optical path from the fiber collimator to the cavity (Kogelnik & Li, 1966). The $1/e^2$ widths (i.e. beam size) on the cavity mirrors are 0.31 mm and 0.35 mm. The optical paths are shown in Fig.2.9, where the incident signal, the cavity reflected signal and the laser output are drawn in solid, dotted and dashed lines respectively.

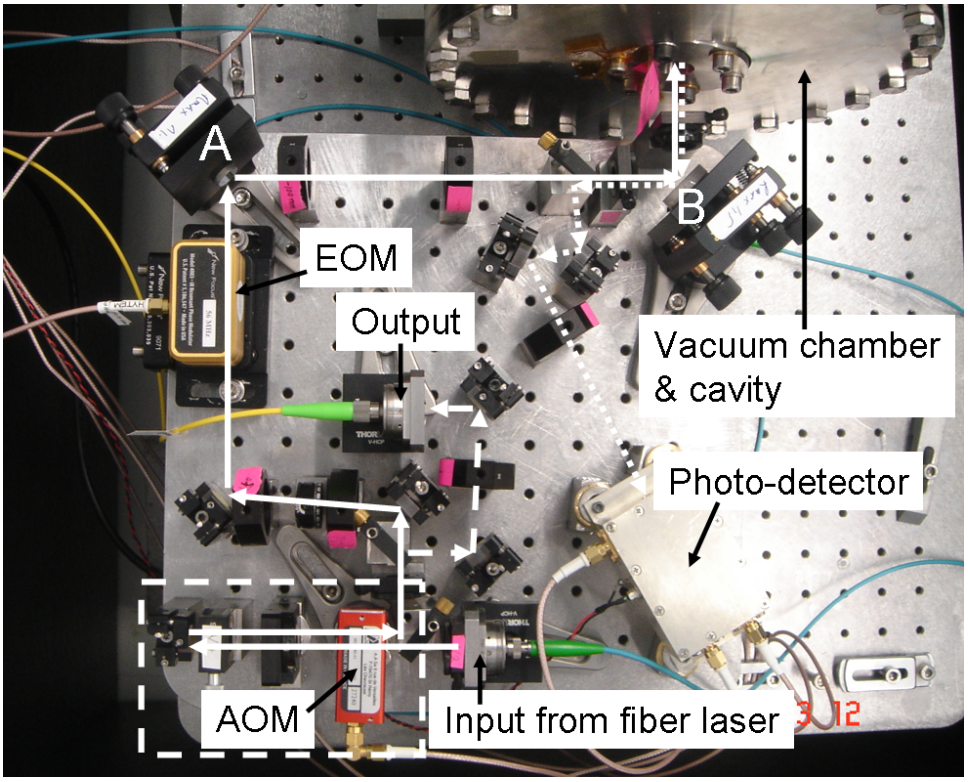


Figure 2.9: Picture of the optical system in the acoustic isolation box.

- Preliminarily align the laser beam to the cavity. It will be very helpful if a visible laser beam is used as a guide [1].

- Linearly sweep the laser frequency over more than a FSR with a signal generator controlling the laser PZT port, and detect the transmission signal with a photodiode. We usually find several peaks on the cavity transmission spectrum, which is monitored by an oscilloscope with "xy" mode, where "x" is the output of the signal generator, "y" is the cavity transmission signal. These peaks correspond to the coupling mode of the cavity. In this step, we can increase the cavity incident optical power to have a good signal-to-noise ratio for monitoring.

- Optimize the mode coupling by adjusting mirror A and B (see Fig.2.9) until there is only one well coupled mode over a FSR and the transmission signal should be as high as

[1] The visible laser beam can propagate through the cavity, because the high reflection coatings of the cavity mirror are not efficient to that wavelength.

possible. This mode usually is the TEM00 mode, which can be verified by monitoring the transmission signal with a camera. When the TEM00 is coupled, the camera takes an image of only one bright local spot.

- Maximize the detection efficiency, which is proportional to the peak-to-peak error signal, by tuning the phase of the demodulation signal with an RF phase shifter (a delay cable). In this step, we should keep the control loop open.

- Set the laser to be far away from the cavity resonance, and minimize the EOM amplitude modulation effect by adjusting the polarizer (see Fig.2.7 and Fig.2.9).

- Stop sweeping the laser frequency and close the control loop to stabilize the laser frequency onto the cavity.

- Finally, optimize the gains (see Fig.2.8) of the loop filter, according to the measured laser frequency noise.

The carrier transmission contrast is measured to be more than 60%.

## 2.5 Measurement results

This section shows and discusses the experimental results, including cavity decay time, laser amplitude noise sensitivity, the laser frequency noise, stability and vibration sensitivities.

### 2.5.1 Cavity optical decay time

The optical decay signal of this cavity is equal to $Ae^{\frac{t-t_0}{\tau}}$, where $A$ is the initial optical power at $t_0$ time and $t$ is the current time, $\tau$ is the cavity decay time. Once the laser can be locked to the cavity, the cavity decay time can be accurately measured. First, we stabilize the laser to the cavity. In succession, we record the optical transmission signal, and switch off the incident optical signal with an RF switch on the AOM RF input. The optical decay signal is then measured and shown in Fig.2.10. By fitting this signal, we determine the cavity decay time to be $\sim 80$ $\mu$s, corresponding to a cavity finesse of $\sim 8 \times 10^5$. Clearly, this is an ultra high finesse cavity at the state-of-the-art level (see Tab.2.1).

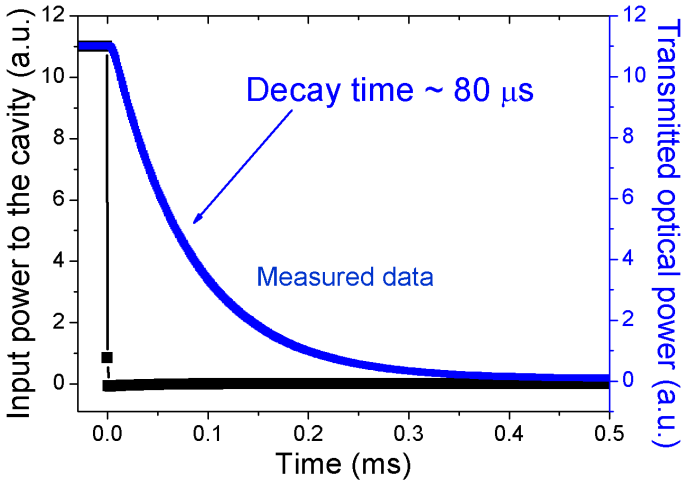


Figure 2.10: Measured optical decay in the cavity.

Table 2.1: Basic cavity Specifications

| Item | Value | Unit |
|---|---|---|
| Cavity length.$L$ | 10 | cm |
| Free spectral range.$\Delta\nu_{FSR}$ | 1.5 | GHz |
| Laser wavelength.$\nu$ | 1.54 | $\mu$m |
| Cavity decay time.$\tau$ | 80 | $\mu$s |
| Cavity linewidth.$\Delta\nu_{cavity}$ | 2 | kHz |
| Mirror reflectance.$R$ | 99.9996% | |
| Cavity Finesse.$F$ | 800,000 | |
| Cavity quality.$Q$ | $10^{11}$ | |

### 2.5.2 Sensitivity to the optical power

We constructed two independent and identical ultra-stable cavity-stabilized lasers. Thus, the laser frequency fluctuation can be measured by comparing their frequencies. We determine a cavity resonance shift of $\sim 10$ Hz/$\mu$W with respect to the transmission power. With a few $\mu$W transmission power of power stability better than 1% peak-to-peak, this effect is much less than 1 Hz without extra power stabilization. According to Eq.2.8, the conversion parameter

$C_p$ of our cavity is $6 \times 10^{-21}$ $\frac{\mathtt{m}}{\mu\mathtt{W}}$, which is comparable to that in Young *et al.* (1999) (see Eq.2.8).

### 2.5.3 Frequency noise of the stabilized laser

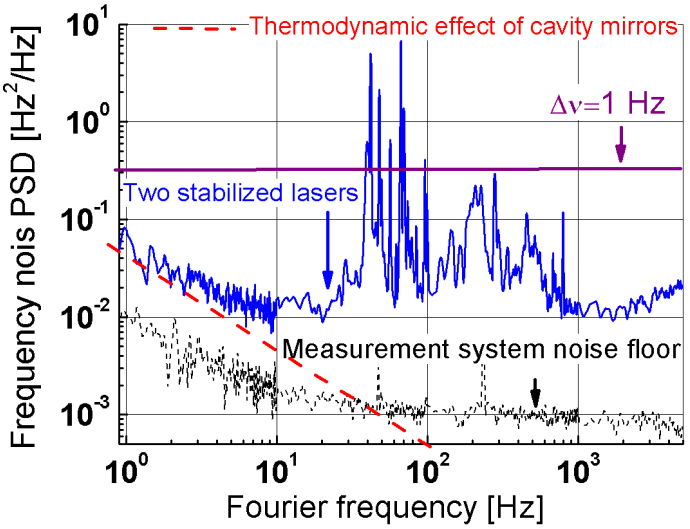


Figure 2.11: Frequency noise PSD of two cavity-stabilized lasers, the measurement system noise floor and the thermodynamic effect of cavity mirrors for two lasers.

The cavity-stabilized laser frequency noise is evaluated by using following steps. First, we detect the beat-note signal between two cavity-stabilized lasers with a photodiode. The beat-note signal is at a frequency of $\sim$ 380 MHz. The beat-note signal is down-converted to $\sim$ 25 MHz by mixing with an RF signal provided by a commercial synthesizer. The measurement system noise floor is dominated by the noise floor of a home-made low noise frequency-to-voltage converter. In order to reduce the influence of this floor, we multiply the $\sim$ 25 MHz signal by a factor of 4 by using low noise RF frequency multipliers. After that, we down-convert the multiplied signal ($\sim$ 100 MHz) to be 700 kHz with another commercial synthesizer. Then, we transform the laser frequency fluctuations to voltage variations with the low noise frequency-to-voltage converter. Finally, we evaluate the laser frequency noise by analyzing the converted voltage signal with a fast Fourier transformer (FFT). The frequency noise PSD of the two lasers is shown in Fig.2.11. In the range of 1 Hz to 10 kHz, it is well below that of a white

frequency noise dominated 1 Hz linewidth laser. The 1/f noise for low Fourier frequency is the contribution of the cavity mirrors' thermodynamic noise. The calculated value (red dashed line) well fits the experimental result.

### 2.5.4 Frequency noise of the free-running laser

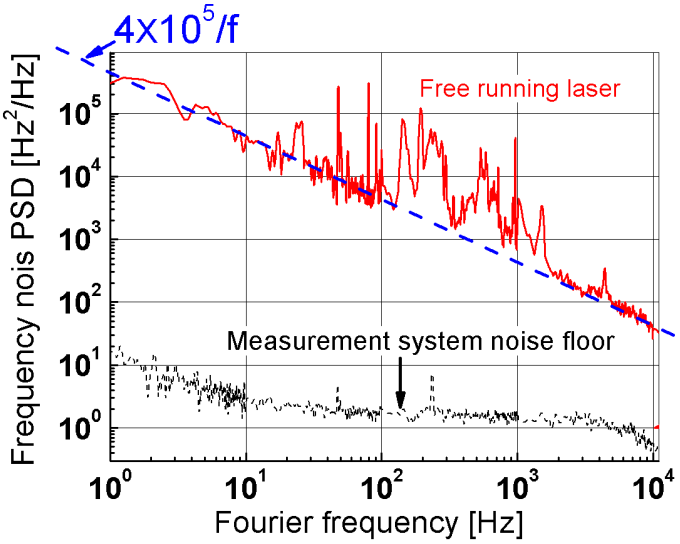


Figure 2.12: Frequency noise PSD of a free running fiber laser and the measurement system noise floor.

Fig.2.12 shows the free-running laser frequency noise. We use one cavity-stabilized laser as the frequency reference to measure the frequency noise of the free-running laser. The only difference from the last measurement is that we divide the beat-note frequency by a factor of 10 instead of multiplying by 4. This is because the frequency-to-voltage converter requires an input frequency in the range of 100 kHz − 1 MHz, whereas the free-running laser fluctuates by a few MHz during a measurement. Consequently, the measurement range is enlarged 40 times compared to the previous experiment, leading to ∼ 9 MHz. The measurement system noise floor, multiplied by a factor of $40^2$ (see Fig.2.12), is still negligible in comparison with the frequency noise of the free-running laser. The PSD of the laser frequency noise is about $4 \times 10^5/f$, where $f$ is the Fourier frequency.

### 2.5.5 Frequency fluctuation of the stabilized laser

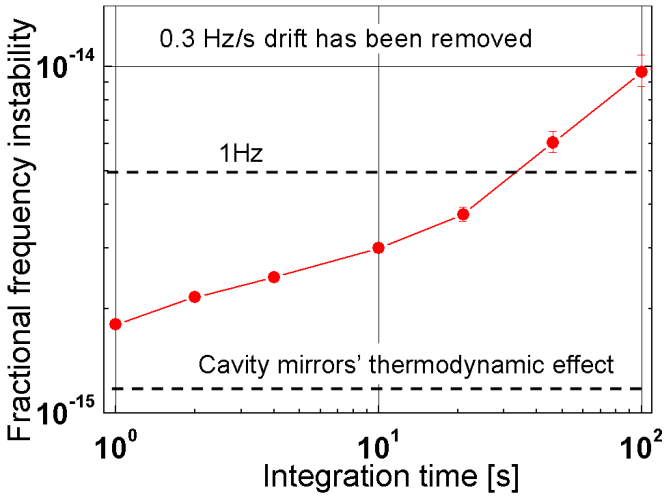


Figure 2.13: Fractional frequency instability of the two cavity-stabilized lasers (0.3 Hz/s frequency drift has been removed).

We evaluate the laser frequency stability using the overlapping Allan deviation of the beat-note frequency recorded with a Π-type counter. After removing a linear drift of about 0.3 Hz/s, the Allan deviation (see Fig.2.13) is less than $2 \times 10^{-15}$ for 1s integration time. The laser linewidth is less than 1Hz for a measurement time of $< 10$ s. The frequency instability of the ultra-stable cavity-stabilized laser is mainly limited by the thermodynamic effect of the cavity mirrors and environmental temperature fluctuations. By using lower thermodynamic effect materials (e.g. fused silica and cryogenically cooled sapphire) and a longer cavity, the cavity stability definitely can be further reduced. For a 10 cm cavity with fused-silica substrate mirrors, the instability can reach a level of a few $10^{-16}$ for 1 s integration time. However, these approaches lead to a significant extra complexity out of the scope of our work.

### 2.5.6 Vibration sensitivity

Fig.2.14 shows the vibration sensitivity of the cavity measured at 4 Hz Fourier frequency along the 3 directions. We measure them with following steps:

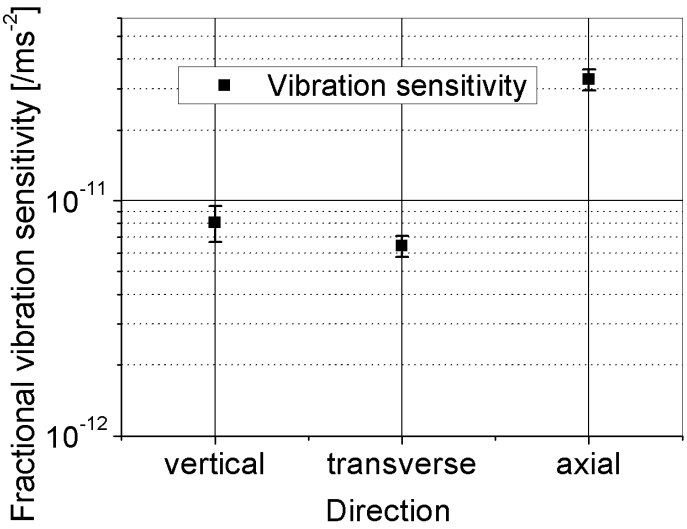


Figure 2.14: Vibration sensitivity of the cavity.

- First, we inject a sinusoidal 4 Hz modulation voltage signal to the feedback port of the active vibration isolation platform, producing a single tone vibration in one direction (vertical, transverse or axial direction of the cavity);
- Second, we measure the stabilized laser frequency, and simultaneously record the platform vibration with a low noise seismometer;
- Third, we calculate the laser frequency noise PSD $S_\nu(4\ \mathtt{Hz})$ and the vibration noise PSD $S_V(4\ \mathtt{Hz})$ by using the obtained data;
- Finally, the vibration sensitivity is determined to be $\frac{1}{\nu}\sqrt{\frac{S_\nu(4\ \mathtt{Hz})}{S_V(4\ \mathtt{Hz})}}$ ($\nu$: the laser frequency) at 4 $Hz$ Fourier frequency.

The error bars are due to the vibration crosstalk between different directions. These measured values are $2-3$ times higher than those of a similar cavity reported in Millo *et al.* (2009b), because the simple mounting (shown in Fig.2.2) can not guarantee restoring forces of the cavity support. With the vibration isolation platform, the vibration noise induces some peaks between 100 Hz and 1 kHz on the laser frequency noise spectrum (see Fig.2.11). Actually, one laser's vibration platform was not working well, when we did the measurement. However, it

does not dominate the laser frequency noise for low Fourier frequencies, and its contribution on the laser linewidth and stability is negligible.

## 2.6 Summary

In summary, we have developed two independent ultra-stable cavity-stabilized lasers with the PDH method. Their frequency noise is limited by the fundamental thermodynamic effect of the cavity mirrors for Fourier frequencies lower than $\sim$ 10 `Hz`. The laser linewidth is less than 1 `Hz` for a less than 10 `s` measurement. Its frequency instability is close to $10^{-15}$ for 1 `s` integration time. The laser performance exceeds the requirement of the optical link experiment (see later).

# Chapter 3

# Fiber-stabilized laser

This chapter is devoted to the technique of stabilizing laser frequency on an optical fiber delay. It introduces the operational principle and experimental setup of the fiber-stabilized laser in the first part. In succession, it gives the noise analysis of this system. The measurement results include the frequency noise spectra, instabilities and the linearity of the laser frequency sweep, in addition to a realization of digitally locking this laser to a cavity-stabilized laser. The vibration sensitivity of the reference fiber and techniques for reducing this sensitivity are discussed in the last part.

## 3.1 Introduction

The cavity-stabilized laser exhibits excellent performance. However, this approach requires fine alignment of free-space optical components and spatial mode matching. Moreover, a high-finesse cavity is expensive, bulky and fragile. Furthermore, the PDH method is not convenient to tune the laser frequency. To have a more robust, simpler, cheaper, transportable and frequency-tunable laser with low frequency noise, other stabilization techniques are required. An alternative method is to use an optical fiber as a reference to stabilize laser frequency. A pioneer experiment was done about 20 years ago, using the approach of stabilizing laser frequency onto a fiber delay (Chen, 1989). In this case, a fiber interferometer with two arms of different length was used to detect the laser frequency fluctuations.

In fact, as early as 1980, such a delayed interferometer was used for the measurement of laser frequency noise and laser linewidth (Okoshi *et al.*, 1980). The delay arm of the interferometer is usually an optical fiber, because the fiber is low noise, low-cost, low-loss,

easily-available and easily-splicable. When the delay line is longer than the coherence length of the laser, one can measure directly the laser linewidth. With a shorter delay line, the output of the interferometer gives the laser frequency fluctuation $\delta\nu$ for Fourier frequencies $f$ much below the inverse of the fiber delay time. Then, the laser frequency fluctuation $\delta\nu$ can be corrected by adding a frequency adjustment of $-\delta\nu$. In practice, we stabilize the interferometer output to an given value, which enables to stabilize the laser frequency.

Most of the previous experiments (Cliche *et al.*, 2006; Cranch, 2002) adopted an homodyne detection configuration with an about 100 m fiber delay line. The frequency noise **P**ower **S**pectral **D**ensity (PSD) has achieved about 10 $\mathrm{Hz}^2/\mathrm{Hz}$ ranging from 100 Hz to 1 kHz with a $1/f^2$ spectrum for lower Fourier frequencies. With a vacuum chamber and a double pendulum vibration isolation, a recent fiber-stabilized laser (Takahashi *et al.*, 2008) obtained a frequency noise PSD of a few $\mathrm{Hz}^2/\mathrm{Hz}$ ranging from 10 Hz to 100 Hz and a few tens of $\mathrm{Hz}^2/\mathrm{Hz}$ at 1 Hz. On the other hand, some other research groups focused on the frequency tunability of the fiber-stabilized laser (Boggs *et al.*, 1998; Greiner *et al.*, 1998). They have demonstrated the fast tunability (Gorju *et al.*, 2007) and high sweep linearity (Barber *et al.*, 2010; Roos *et al.*, 2009) of the fiber-stabilized laser.

In this chapter, I will present a fiber-stabilized laser (Kéfélian *et al.*, 2009a) with frequency noise PSD at least 20 dB lower than the previous reported results in the 1 Hz − 10 kHz range. This performance is due to the use of a heterodyne detection configuration and a longer fiber delay line (1 km) with appropriate environmental isolation. In addition, with a 2.5 km reference fiber we obtained even lower frequency noise for low Fourier frequencies and demonstrated that this laser maintains low noise feature when it is frequency swept at a few tens of MHz/s (Jiang *et al.*, 2010). The peak-to-peak non-linear error is about 50 Hz for a 40.5 MHz/s frequency sweep over a 600 MHz span.

## 3.2 Operational principle

This section discusses the operation principle, the transfer function and configurations of the interferometer, which is used to stabilize the laser frequency.

### 3.2.1 Laser frequency stabilization principle

As shown in Fig.3.1, the laser signal is fed into the interferometer which has two arms of different length. The laser frequency fluctuation is measured by the interferometer and

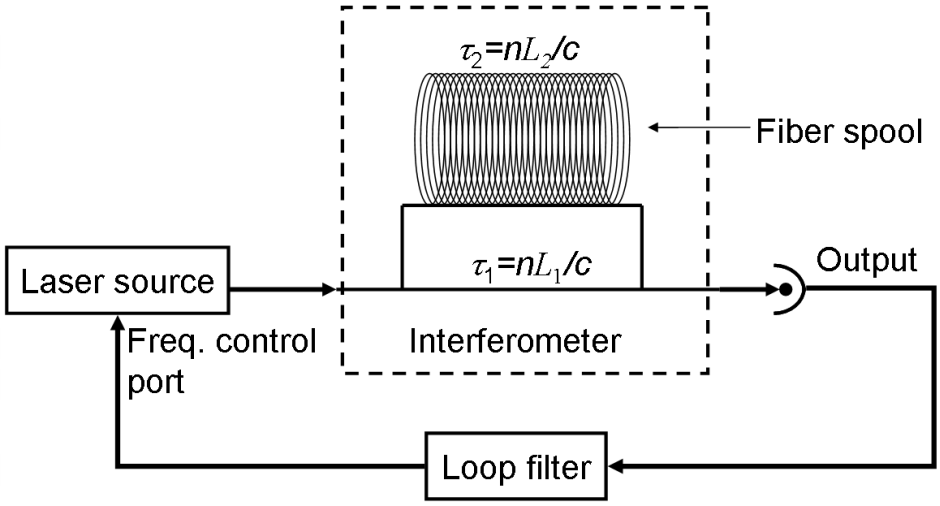


Figure 3.1: Principle scheme of a fiber-stabilized laser ($\tau = nL/c$).

suppressed by using a negative feedback at the laser frequency control port with a signal produced by the loop filter. The interferometer output depends on the laser phase difference between the two arms, thus it depends on $\tau_1 - \tau_2$ or $L_1 - L_2$. Usually, one arm (the fiber) is much longer than the other, which is as short as possible. As a result, the fiber delay time $\tau$ determines the stabilized laser frequency. To realize a low frequency noise laser, the reference fiber needs a good thermal and vibrational isolation. With a proper configuration (see later), this stabilization approach allows well controlled laser frequency tuning without physically acting on the interferometer reference.

### 3.2.2 Transfer function of a length unbalanced delay line interferometer

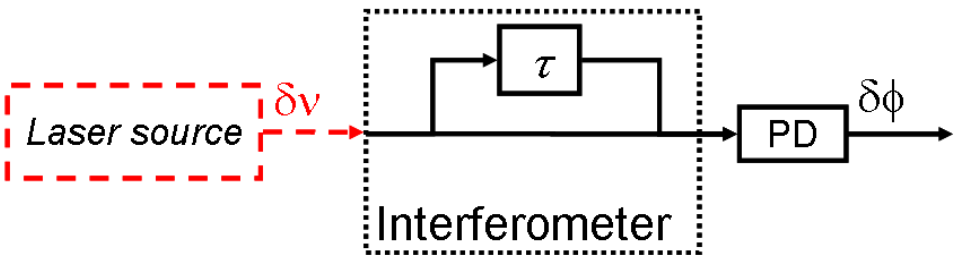


Figure 3.2: Length unbalanced interferometer (homodyne detection configuration).

The length unbalanced delay line interferometer is shown in Fig.3.2. We introduce the following notation:

- The laser phase $\varphi(t)$.
- The laser frequency $\nu(t) = \nu_0 + \delta\nu(t)$, where $\delta\nu(t)$ is the laser frequency fluctuation.
- The fiber length $L_f$.
- To simplify, we suppose that the short arm has null length and delay.
- The fiber length difference $L$ between two arms, $L$ is equal to $L_f$ or $2L_f$ depending on the interferometer configuration (see later).
- The fiber delay difference between two arms $\tau = \frac{nL}{c}$, where n is the effective refractive index, c the speed of light in vacuum.
- The detected phase difference $\phi(t) = \phi_0 + \delta\phi(t)$ between two arms, where $\delta\phi(t)$ is the phase fluctuation. One has $\phi(t) = \varphi(t) - \varphi(t-\tau) \approx 2\pi\nu(t)\tau$ when $\nu(t)$ is approximately constant during delay $\tau$.

The output of the interferometer is the beat-note signal obtained by combining the laser signals and detected by using a photodiode (PD). In our experiment, we use standard phase noise measurement methods (Goldberg, 2000) to analyze the output of the interferometer. Then, we define the transfer function of the interferometer as the ratio of $\delta\phi(t)$ to $\delta\nu(t)$. The transfer function in the frequency-domain is (Sheard *et al.*, 2006)

$$\begin{cases} T(f) & = & \frac{\widetilde{\delta\phi(f)}}{\widetilde{\delta\nu(f)}} = \frac{1-e^{-i2\pi f\tau}}{if}, [\texttt{rad/Hz}] \\ \widetilde{\delta\phi(t)} & \approx & 2\pi\tau\widetilde{\delta\nu(t)} \ \texttt{for} \ f \ll 1/\tau \end{cases}, \tag{3.1}$$

where $f$ is the Fourier frequency, $\widetilde{\delta\nu(f)}$ and $\widetilde{\delta\phi(f)}$ are Fourier transforms of $\delta\nu(t)$ and $\delta\phi(t)$. The numerator $1 - e^{-i2\pi f\tau}$ describes the beat-note between the laser frequencies at time $t$ and $t - \tau$. The denominator converts the frequency fluctuation to the phase fluctuation.

The frequency response of the interferometer is plotted both for phase (blue dashed line) and magnitude (black solid line) in Fig.3.3. At low frequencies ($f \ll 1/\tau$), the magnitude is approximately equal to $2\pi\tau$. A longer fiber leads to a higher detection sensitivity. However, the detection noise is not sensitive to the fiber length. Consequently, the longer fiber increases the signal-to-noise ratio, resulting in a less detection noise effect. We have also to consider

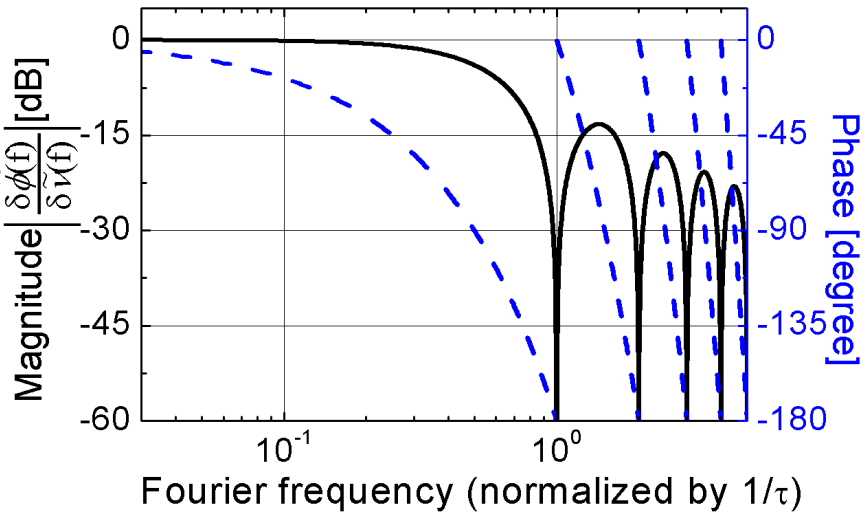


Figure 3.3: Frequency response of the interferometer, where the magnitude in dB is normalized to the low frequency response ($2\pi\tau$).

the effect of the fiber noise, since this fiber noise is coupled into the laser frequency when the laser is stabilized. Standard deviation of the total fiber delay fluctuations $\tau$, arising from spatially uncorrelated local delay fluctuations (e.g. intrinsic thermal noise), is proportional to $\sqrt{L_f}$ Wanser (1992), while the error signal scales as $L_f$. As a result, a longer fiber leads to a lower system noise. However, for a frequency of integer times $1/\tau$ ($= \frac{c}{nL_f}$ *or* $\frac{c}{2nL_f}$), the interferometer has null response, corresponding to zero gain points in the loop response. Maintaining a bandwidth much larger than $1/\tau$ is feasible, but requires a complex servo-loop design (Sheard *et al.*, 2006) and may suffer from system oscillations. The use of a complicated multiloop system (Yao & Maleki, 2000) can eliminate the oscillation problem. However, for a system containing only one interferometer, a trade-off between a lower noise floor and a higher noise rejection bandwidth has to be found.

We define the quality factor $Q = \nu_0 \frac{\delta\phi}{\delta\nu} = 2\pi\nu_0\tau$ of the interferometer by considering the discrimination slope at the stabilization frequency. This definition is the same as that of the PDH method. Using an interferometer with $L = 2$ km , the quality factor of the interferometer is $1.2 \times 10^{10}$ for a 1.542 $\mu$m wavelength laser, which is equivalent to the quality factor of a 10 cm cavity with a finesse about $9 \times 10^4$. Note that the high finesse cavities (Millo *et al.*,

2009b; Zhao *et al.*, 2009) have finesse of usually a few $10^5$, up to $1 \sim 2 \times 10^6$ for the best one.

Different types of interferometers can be used to stabilize the laser frequency onto the fiber delay time, and these different configurations may lead to different performances and different features, such as frequency tunability.

### 3.2.3 Homodyne detection and Heterodyne detection

In terms of the optical beat-note frequency, the detection configurations is either homodyne detection or heterodyne detection.

***Homodyne detection*** configuration shown in Fig.3.2 is the simplest configuration, in which there is only one optical frequency. The output detected by a photodiode is

$$V_{PD} = V_{dark} + V_{Opt} + K_{PD}\cos(\phi), \tag{3.2}$$

where $V_{dark}$ is the voltage caused by the photodiode dark current, $V_{Opt}$ is the voltage induced by the received average optical power, $K_{PD}$ is the detected beating amplitude. The last term of Eq.3.2 represents the laser frequency fluctuation. In this condition, the error signal is obtained by comparing the detected signal $V_{PD}$ with a given reference voltage $V_s$. The amplitude noise of the first two terms and the reference voltage $V_s$ directly superimposes on the error signal. In addition, the flicker electronic noise of the photo-detector for low Fourier frequencies degrades the detection signal. Consequently, it is difficult to achieve an ultra-low frequency noise detection floor. In closed loop, the phase $\phi$ takes a value $\phi_s$ imposed by $V_s$. Thus, the locked laser frequency $\nu$ is limited to a discrete series of values $[\phi_s/(2\pi) + q]/\tau$, where $q$ is an integer. $\phi_s/(2\pi)+q$ is the difference of optical wave cycles in two interferometer arms. The phase $\phi_s$ can be adjusted in a range of $[-\pi/2,\pi/2]$. Thus, the laser frequency can be tuned in a limited range of $1/2\tau$.

***Heterodyne detection*** is the configuration, in which the interferometer output is the beat-note signal between two optical waves of different frequencies. The interferometer converts the laser frequency fluctuation into the phase fluctuation of the detected radio-frequency (RF) signal. The effect of detection amplitude noises induced by $V_{dark}$ and $V_{Opt}$ is less than that of the homodyne detection, because the RF mixer has a low amplitude-to-phase conversion coefficient of $\sim 10^{-2}$. Moreover, that configuration does not require a voltage reference $V_s$, which can induce an additional noise. Furthermore, with a proper modulation frequency, the detection noise could be only dominated by the quantum noise floor. Consequently,

the heterodyne detection has a much lower noise floor compared with the homodyne detection. However, the heterodyne detection is more complex, because it has two extra stages: modulation and demodulation.

### 3.2.4 Heterodyne detection methods

There are two methods to generate heterodyne detection signal: phase modulation and frequency shift of the optical signal.

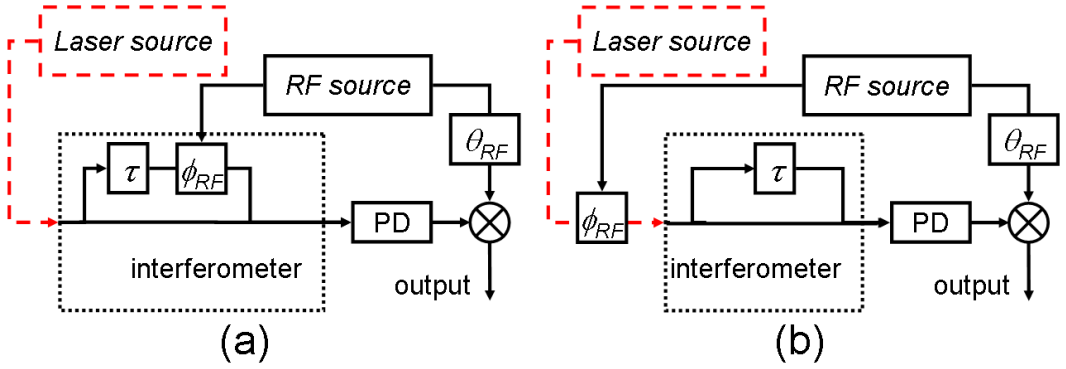


Figure 3.4: Heterodyne detection configurations with phase modulation methods (similar to the PDH method).

Fig.3.4a shows a heterodyne detection configuration by using a ***phase modulation*** method. An **E**lectro-**O**ptic **M**odulator (EOM) inserted in one arm of the interferometer modulates the phase of the optical signal. The photodiode output $V_{PD}$ is then $V_{dark} + V_{Opt} + K_{PD}cos[\phi + A_m sin(2\pi f_m t)]$, where $A_m$ and $f_m$ are the modulation depth and frequency. We assume that the phase of the demodulation signal is synchronized to the modulation signal by adjusting $\theta_{RF}$. Then, the demodulated signal at the output is

$$\begin{aligned} \langle V_{output} \rangle &= K_{eff} \langle \cos[\phi + A_m sin(2\pi f_m t)] sin(2\pi f_m t) \rangle \\ &= K_{eff} J_1(A_m) \sin(\phi) \end{aligned} , \tag{3.3}$$

where $K_{eff}$ is the detection efficiency, relevant to the optical power and converting efficiency of the photodiode and the RF mixer, $J_1(A_m)$ is the first order Bessel function. The laser frequency fluctuation $\delta\nu$ is then measured. The term $K_{eff} J_1(A_m)$ indicates that the maximum detection sensitivity occurs for a modulation depth of about 1.8 `rad`. The modulation depth is not a critical parameter if the laser frequency noise is not limited by the photo-detector's

noise. This configuration has a lower detection noise floor than the homodyne detection; and it can have a lower power consumption compared with the frequency shift heterodyne (see later), because an EOM can be driven by a lower RF power than an acousto-optic modulator (AOM). Another approach shown in Fig.3.4b has an equivalent function. However, there is no active component in the interferometer; therefore, a better environmental isolation can be done for the interferometer and a lower interferometer noise is expected than the first approach. It is worth noting that the laser frequency can not be tuned for either configuration.

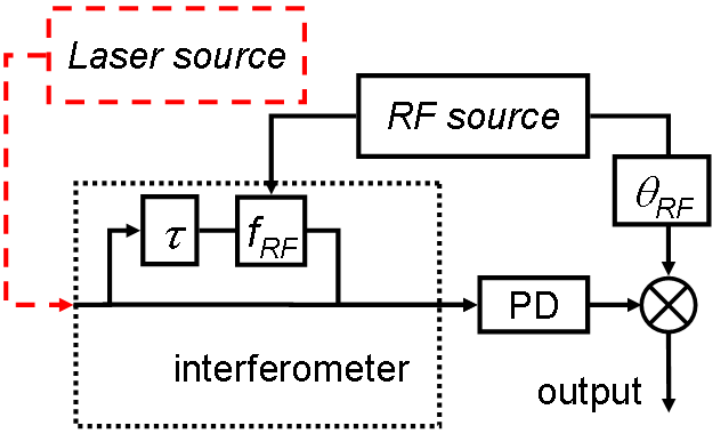


Figure 3.5: Heterodyne detection configuration with frequency shift method.

In order to tune the laser frequency in a wide range, the heterodyne signal has to be produced by using ***frequency shift*** method (see Fig.3.5) (Boggs *et al.*, 1998; Greiner *et al.*, 1998). An AOM added in one arm of the interferometer shifts the optical frequency from $\nu$ to $\nu + f_{RF}$. The photodiode RF output $K_{PD}\cos(\phi + 2\pi f_{RF}t)$ is demodulated, giving the error signal $K_{eff}cos(\phi + \theta_{RF})$ at the interferometer's output. By applying a negative feedback on the control port of the laser frequency, we can stabilize the phase $\phi + \theta_{RF}$ to be $\pi/2$ or $3\pi/2$, corresponding to the quadrature condition. Then, a phase adjustment $\delta\theta_{RF}$ of demodulation signal leads to a PD output phase shift $\delta\phi = -\delta\theta_{RF}$, corresponding to a laser frequency variation of $\delta\nu = \delta\phi/2\pi\tau$. The wide range tunability is the unique feature of the frequency shifted heterodyne configuration. It is not easy to shift the phase of a RF signal in a large

range by using a phase shifter. Thanks to the **D**irect **D**igital **S**ynthesizer (DDS), we can set a little frequency offset on the demodulation signal, which is equivalent to continuously adjusting the phase with a wide range. Assuming that we set a nearly arbitrary frequency offset $\Delta\nu_{RF}$ onto the demodulation signal while the locking loop is closed, the laser frequency follows the equation

$$\nu(t) = \frac{q + \frac{\phi(t)}{2\pi}}{\tau} = \frac{q + \frac{\phi(0)}{2\pi}}{\tau} - \frac{\delta\theta_{RF}(t)}{2\pi\tau} = \nu_0 - \int_0^t \frac{\Delta\nu_{RF}}{\tau} dt, \tag{3.4}$$

which indicates that the laser frequency is swept at a constant rate of $\frac{\Delta\nu_{RF}}{\tau}$.

### 3.2.5 Mach-Zehnder interferometer and Michelson interferometer

Both Mach-Zehnder and Michelson interferometer with length-unbalanced arms exhibit the laser frequency discriminating function.

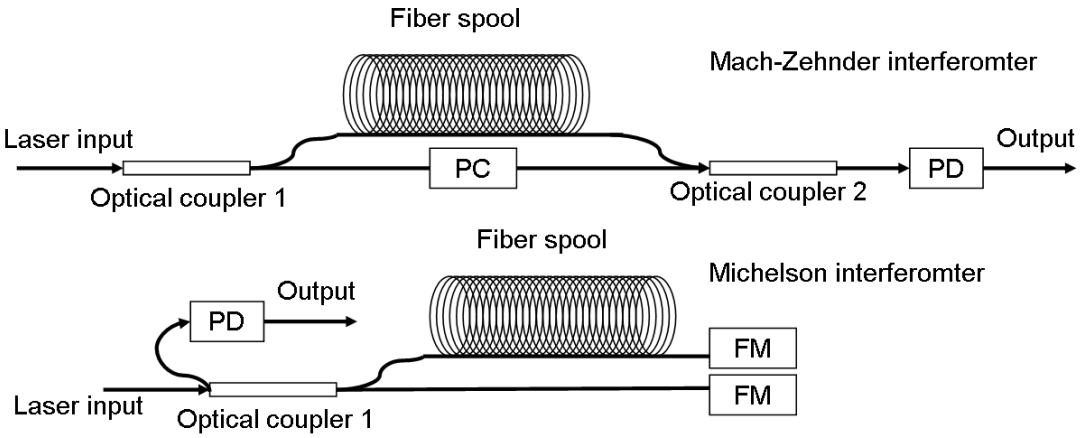


Figure 3.6: Mach-Zehnder interferometer and Michelson interferometer.

The ***Mach-Zehnder*** interferometer shown in the upper part of Fig.3.6 comprises two optical couplers and one **P**olarization **C**ontroller (PC). The PC is used for aligning the polarization states of the combined optical signals. It should be automatically controlled if the laser is expected to work without adjustment for a long time. This interferometer is immune to the first order optical reflections in the interferometer, for the first order reflections are not coupled in the photodiode. The optical reflections may significantly influence the

frequency noise of a swept laser for low Fourier frequencies. This effect will be discussed later.

The ***Michelson*** interferometer shown in the lower part of Fig.3.6 consists of one optical coupler (usually 50/50 splitting ratio) and two **F**araday **M**irrors (FM-45° for single pass). The FMs guarantee that the output polarization states are orthogonal to the input states for backward reflected fiber-optic links (Kersey *et al.*, 1991; Pistoni & Martinelli, 1991). Consequently, the two combined waves at the Michelson interferometer output always have the same polarization states, leading to a maximum beat-note amplitude without requiring any polarization controller. Clearly, the Michelson interferometer is more suitable to build a robust laser system. The cost is the doubling of the unbalanced delay time, which leads to a narrower laser noise control bandwidth or an increase of the fiber intrinsic thermal noise's effect (see later).

## 3.3 Experimental setup

In our experiment, we use the frequency shifted heterodyne Michelson interferometer to stabilize laser frequency. Since the laser frequency can be swept by setting a frequency offset onto the demodulation signal, we call the laser an "agile laser".

### 3.3.1 Structure of the agile laser

Fig.3.7 shows the scheme of the agile laser, where the optical signals, RF signals and low frequency signals are drawn in red solid, blue dot and black dashed lines respectively. An acousto-optic modulator (AOM1) is placed into one arm of the interferometer and modulated by a 70 `MHz` RF signal. Consequently, the heterodyne detection signal is at $2f_{AOM1}$ (140 `MHz`) frequency. We use a home-made low phase noise tunable synthesizer (Fig.3.9) providing a $2f_{AOM1} + \Delta\nu_{RF}(t)$ RF signal for demodulation. Successively, a loop filter (LF) converts the demodulated signal into laser frequency correction signals. These correction signals simultaneously act on a piezo-electric **T**ransducer (PZT) stretcher controlling the laser cavity length and a **V**oltage **C**ontrolled **O**scillator (VCO), which drives AOM0. The control of the PZT has a large dynamic range with a slow response; while the control of the AOM has a small dynamic range with a fast response. Here, we combine benefits of both control ports to correct the laser frequency noise with a high control bandwidth and a large dynamic range. For convenience, we use the AOM0 and the VCO, which we previously used in the experiment of

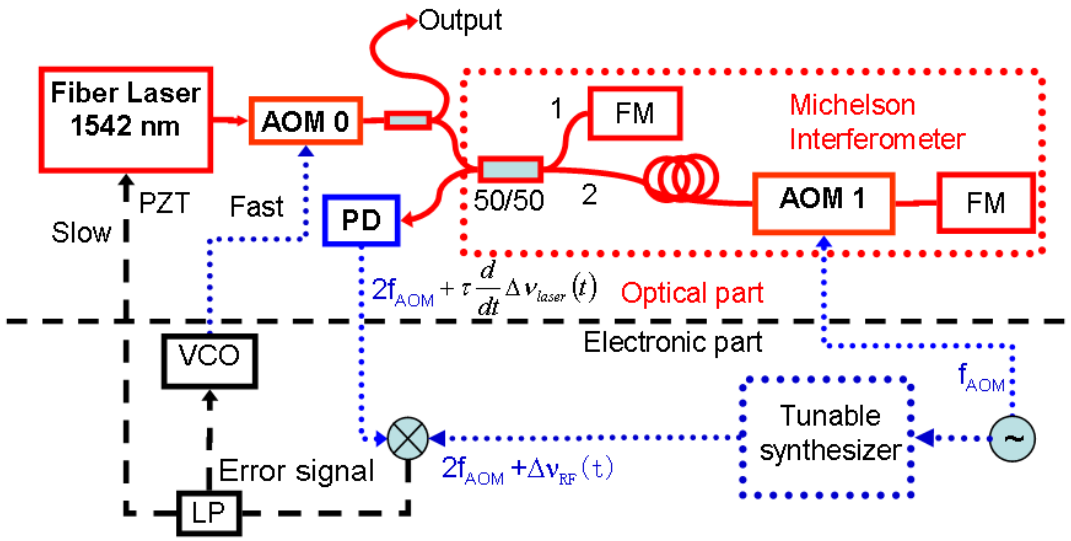


Figure 3.7: Experimental setup scheme.

stabilizing the laser frequency to an ultra-stable cavity. All interferometer components are pigtailed off-the-shelf fiber optical elements, which makes the system alignment-free, simple and robust. The reference fiber is standard single mode fiber (SMF-28), which is widely used in telecom system.

### 3.3.2 Electronic system

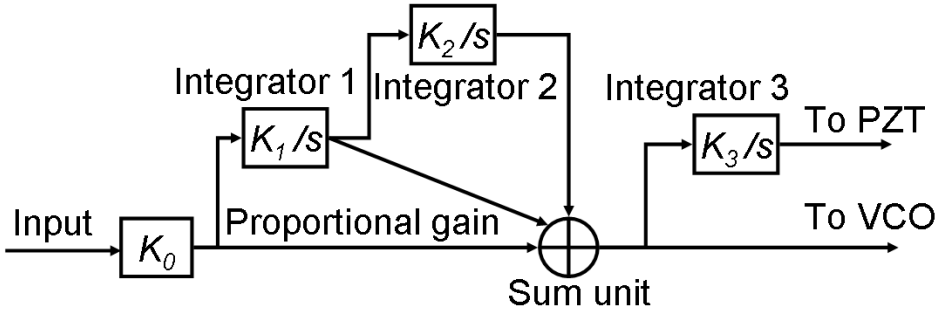


Figure 3.8: Loop filter scheme.

The loop filter scheme shown in Fig.3.8 has a maximum bandwidth of about 2 MHz with a proportional amplifier and 3 integrators. All the gains $K_0, K_1, K_2$ and $K_3$ are independently adjustable. The summed output of the proportional amplifier and first two integrators controls the VCO, leading to a fast laser frequency correction. The PZT stretcher port of the commercial fiber laser is controlled by a slowly integrated signal of the VCO control voltage for large range frequency corrections, which can not be achieved by adjusting the $f_{AOM0}$ due to the tuning range limited to $\pm 1$ MHz.

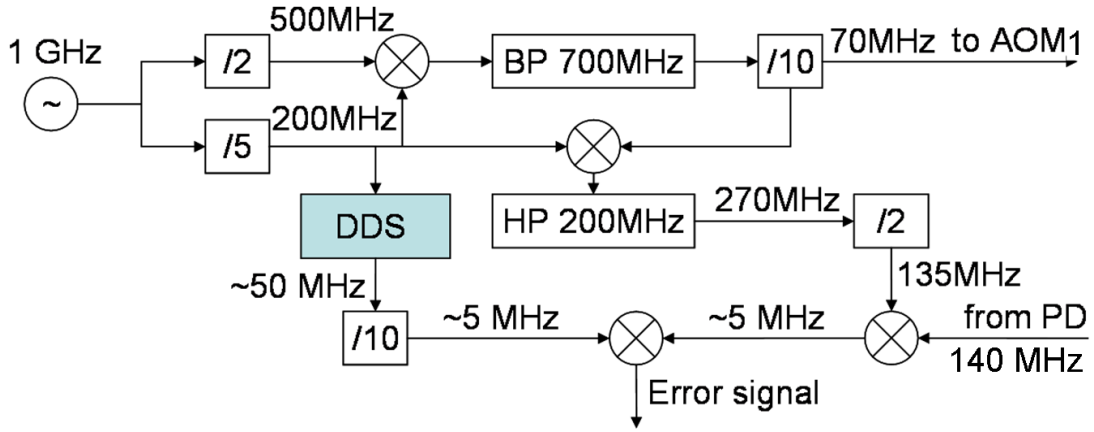


Figure 3.9: The scheme of the tunable synthesizer, BP (band-pass filter), HP (high-pass filter).

A crucial part of the electronic system is the tunable synthesizer, which is specially designed for this experiment. The synthesizer phase noise directly adds into the error signal at the demodulation stage. And the servo system converts the synthesizer phase noise into an equivalent laser frequency noise. Then, the synthesizer phase noise should be low enough. The scheme of this synthesizer is shown in Fig.3.9. All the signals are synthesized from a common 1 GHz source. The tuning function is realized by using a low noise Direct Digital Synthesizer - DDS (AD9852) with a 200 MHz clock frequency reference. To obtain a low phase noise tunable local signal, a double frequency conversion technique is used. We first down-convert the 140 MHz heterodyne signal to an intermediate frequency of $\sim$ 5 MHz, and then we mix it with a tunable DDS output signal at 5 MHz $+ \Delta\nu_{RF}(t)$ to produce a base-band error signal. We obtained the phase noise of the synthesizer shown in Fig.3.10 by analyzing the beat-note between this synthesizer and another commercial one (RFR2032A). In fact, we

believe that our synthesizer is less noisy than the commercial one consistent to its specified noise. The phase noise effect of the tunable synthesizer is negligible in our experiments (see section 3.4.6).

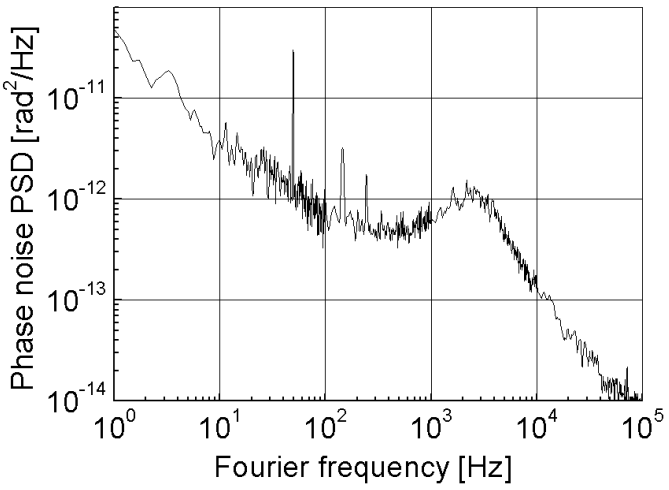


Figure 3.10: Phase noise PSD of $\sim$ 5 MHz demodulation signal.

## 3.4 Noise analysis

Since our target is the development of an ultra-low frequency noise laser, we have to carefully evaluate the noise contribution of each part in the system. In the negative feedback control system, the noises can be catalogued into two classes: in loop noise and out of loop noise.

The in loop noise includes the laser frequency noise and most of baseband electronic noises (e.g. 50 `Hz` noise). The control system measures and corrects these noises within the control bandwidth. The in-loop noise effect is proportional to $K/(1+G)$ in amplitude, where $G$ is the whole loop gain and $K$ is the gain from noise source to the error signal. Thus, we can limit this effect by setting proper loop gains $G$ and $K$.

The out of loop noise includes the fiber intrinsic thermal noise, environmental coupled fiber noise, stray optical reflections, the detection noise and the phase noise of modulation and demodulation signals. It is the noise of the system reference. In control bandwidth,

the control system does not correct these noises, but converts them into the laser frequency fluctuations. We can not reduce them by optimizing the control system.

In this section, we only discuss the out-of-loop noise.

### 3.4.1 Effect of fiber intrinsic thermal noise

The intrinsic thermal noise of the fiber caused by random temperature fluctuations within the fiber is a fundamental limitation of many fiber-based systems, such as acoustic sensors, magnetometers, accelerometers and gyroscopes. Both the length and the index of refraction are sensitive to the thermal motion of the fiber. In terms of the delay time, the effect on the refractive index is almost one order of magnitude larger than that on the fiber length with $dn/dT \approx 10^{-5}$ /K. These effects have been investigated theoretically (Glenn, 1989; Wanser, 1992) and experimentally (Knudsen *et al.*, 1995). Recent calculation has also considered the effect of a finite cladding (Foster *et al.*, 2007). This calculation leads to significant differences for Fourier frequencies lower than 10 Hz. The theoretical results agree with the measured phase noise PSDs within 3 dB for Fourier frequencies from 10 kHz to 100 kHz (Foster *et al.*, 2007; Knudsen *et al.*, 1995). However, these calculations have never been experimentally verified for low Fourier frequencies, due to other noise sources dominating the measurements. Here, we use Wanser's approach to estimate the thermal noise effect on the laser frequency; the thermal noise effect evaluated by using Foster's approach will also be shown for Fourier frequencies lower than 10 Hz.

According to Wanser's approach, the thermal noise PSD of a fiber follows

$$\Phi^2(f) = \frac{2\pi k_B T^2 L}{\kappa \lambda^2}\left(\frac{dn}{dT} + n\alpha_L\right)^2 \cdot \ln\left[\frac{k_{max}^4 + (2\pi f/D_{th})^2}{k_{min}^4 + (2\pi f/D_{th})^2}\right] \quad [\mathrm{rad}^2/\mathrm{Hz}], \tag{3.5}$$

where $\kappa$ is the thermal conductivity, $T$ is the temperature, $L$ is the fiber length, $\alpha_L$ is the thermal expansion coefficient, $\lambda$ is the optical wavelength, $D_{th}$ is the thermal diffusivity, $k_{min}$ and $k_{max}$ are boundary conditions (Wanser, 1992). The usual values of these parameters are listed in Tab.B.1. According to Eq.3.1, for low Fourier frequencies, the laser frequency noise PSD induced by the thermal noise is

$$\begin{cases} S_\nu^{thermal}(f) \simeq \left[\frac{\Phi(f)}{2\pi\tau}\right]^2 = \frac{\nu^2 k_B T^2}{L}\,\mathcal{F}(\kappa, n, \frac{dn}{dt}, k_{max}, k_{min}, D_{th}) \quad [\mathrm{Hz}^2/\mathrm{Hz}] \\ \mathcal{F}(\kappa, n, \frac{dn}{dt}, k_{max}, k_{min}, D_{th}) = \left(\frac{dn}{ndT} + \alpha_L\right)^2 \cdot \ln\left[\frac{k_{max}^4 + (2\pi f/D_{th})^2}{k_{min}^4 + (2\pi f/D_{th})^2}\right] \end{cases}. \tag{3.6}$$

It is clear that a longer fiber leads to a lower thermal noise floor. Fig.3.11 shows the intrinsic

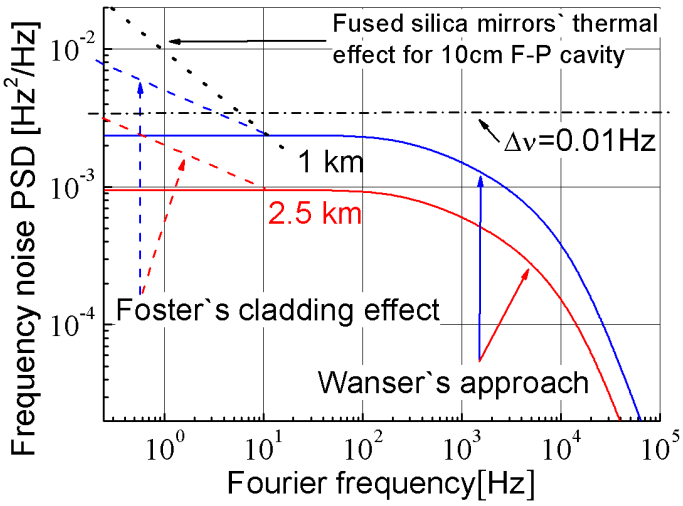


Figure 3.11: Intrinsic thermal noise effect.

thermodynamic floor for a 1.5 $\mu$m wavelength laser with different lengths of SMF-28 fiber. The cladding effect is also given for low Fourier frequencies, based on Foster's calculation result (Foster *et al.*, 2007). This effect is important only for Fourier frequencies lower than 10 Hz and roughly follows a $1/\sqrt{f}$ law. For Fourier frequencies higher than a few Hertz, this effect is well below $3 \times 10^{-3}$ $\mathrm{Hz}^2/\mathrm{Hz}$ for a 1 km fiber. Such a noise corresponds to a laser linewidth less than $3\pi \times 10^{-3}$ Hz $\approx 0.01$ Hz (Elliott *et al.*, 1982). For lower Fourier frequencies, it is less than that of a 10 cm ultra-stable cavity at the state-of-the-art (Alnis *et al.*, 2008; Ludlow *et al.*, 2007; Millo *et al.*, 2009b; Numata *et al.*, 2004; Webster *et al.*, 2008). Over all Fourier frequencies, the cladding effect is well below the frequency noise of all reported laser sources. This is the fundamental frequency noise limitation of a 1.5 $\mu$m wavelength laser when a SMF-28 fiber is used as the reference.

### 3.4.2 Environmental noise effect

Environmental noise includes acoustic noise, seismic noise, air flow and temperature fluctuation. Acoustic noise is mainly in the range from tens of hertz to hundreds of hertz. Seismic noise, air flow and temperature drift are usually more pronounced at low frequencies less than a few hertz. The length-unbalance interferometer is so sensitive to these noise sources that

it needs a good isolation and/or compensation. There are many methods to reduce these effects:

- Isolation of the reference fiber with an air-sealed or vacuum (Abraham & Cornell, 1998) chamber eliminates the effect of acoustic noise, air flow and temperature drift.
- Use of a box with foam can dramatically reduce the effect of acoustic noise and temperature fluctuation.
- With thermal isolations (i.e. Mylar) and/or an active temperature stabilization, the temperature fluctuation effect decreases.
- A vibration isolation platform usually filters out acoustic and seismic noises for Fourier frequencies higher than $\sim$ Hz.
- A very complex suspension system (Aso *et al.*, 2006) can cancel seismic noise effect for low Fourier frequencies $< 1$ Hz.
- Reducing the vibration sensitivities of the fiber decreases the influence of acoustic noise, seismic noise and air flow.

Environmental effects can be sufficiently suppressed by using these methods concurrently.

In our experiment, we use a free standing fiber spool as the reference. We place it in a toroidal shaped aluminum case for protection. After that, we put all the interferometer in an aluminum box ($0.26$ m $\times 0.26$ m $\times 0.165$ m) with thermal isolation (Mylar of film). The box is laid on a commercial compact passive vibration isolation platform (Minus K Inc., BM-10). Both the box and the platform are enclosed in an acoustic and thermal isolation box (Volume $= 0.125$ m$^3$) with acoustic-damping foam (thickness $= \sim 5$ cm) inside. Note that no active thermal control is used in this experiment. We estimate that the decay time for temperature changes is several hours and the acoustic noise insulation is $50 - 60$ dB.

### 3.4.3 Detection noise effect

Detection noise (Beenakker & Schonenberger, 2003) contains shot noise and Johnson noise at optical signal detection stage.

***Shot noise*** follows a Poisson distribution. It is relevant to the photodiode current, happening in the p-n junction. Its PSD, current variance per hertz of bandwidth, is given by

$$\overline{i_n{}^2} = \frac{2e^2\eta P_{opt}}{h\nu}, \tag{3.7}$$

where $e$ is unit of charge, $\eta$ is the detector quantum efficiency, $P_{opt}$ is the total detected optical power and $h\nu$ is the photon energy. The mean power of the signal is

$$\overline{{i_s}^2} = 2\left(\frac{e\eta}{h\nu}\right)^2 P_{opt1}P_{opt2}, \tag{3.8}$$

where $P_{opt1}$ and $P_{opt2}$ are optical powers received from the two interferometer arms. Then, the noise-to-signal PSD (double-sided) is given by

$$\Phi^2_{shot} = \frac{2\overline{{i_n}^2}}{\overline{{i_s}^2}} = \frac{2h\nu P_{opt}}{\eta P_{opt1}P_{opt2}} \quad [\mathtt{rad}^2/\mathtt{Hz}]. \tag{3.9}$$

According to Eq.3.1, for low Fourier frequencies the laser frequency noise PSD induced by shot noise is

$$S_{shot} = \frac{2h\nu P_{opt}}{(2\pi\tau)^2\eta P_{opt1}P_{opt2}} \quad [\mathtt{Hz}^2/\mathtt{Hz}]. \tag{3.10}$$

***Johnson noise*** is a thermal effect. Its PSD, voltage variance per hertz of bandwidth, is given by

$$\overline{{v_n}^2} = 4k_BTR, \tag{3.11}$$

where R is the equivalent source resistance at the primary RF amplifier's input in ohms. The signal power for the voltage received by the primary RF amplifier is

$$\begin{cases} \overline{{v_s}^2} = 2\left(\frac{e\eta}{h\nu}\right)^2 P_{opt1}P_{opt2}\frac{R^2}{10^{L_{in}/10}} \\ L_{in} = -10\log[1-\left(\frac{R-50}{R+50}\right)^2] \end{cases}, \tag{3.12}$$

where, $L_{in}$ is the transmission loss in decibels due to a mismatch between R and the input impedance of the primary RF amplifiers (50Ω). Thus, the noise-to-signal PSD (double sides) is given by

$$\Phi^2_{johnson} = \frac{2\overline{{v_n}^2}}{\overline{{v_s}^2}} = \left(\frac{h\nu}{e\eta}\right)^2 \frac{4k_BT10^{L_{in}/10}}{P_{opt1}P_{opt2}R} \quad [\mathtt{rad}^2/\mathtt{Hz}]. \tag{3.13}$$

According to Eq.3.1, for low Fourier frequencies the laser frequency noise PSD induced by Johnson noise is

$$S_{johnson} = \left(\frac{h\nu}{e\eta}\right)^2 \frac{4k_BT10^{L_{in}/10}}{(2\pi\tau)^2P_{opt1}P_{opt2}R} \ [\mathtt{Hz}^2/\mathtt{Hz}]. \tag{3.14}$$

Use of a longer fiber or higher input optical power leads to a lower detection quantum noise effect, according to Eq.3.10 and Eq.3.14. In our experiments, the splitting ratio of the coupler is 50/50; the transmission loss of AOM1 is about 3 `dB` for single pass; $\eta$ is 0.9; $R$ is 200Ω and the input power to the interferometer is about 200$\mu W$. For a 1 `km` fiber-stabilized laser, the shot noise effect on the laser frequency is about $10^{-6}$ $\mathtt{Hz}^2/\mathtt{Hz}$; the Johnson noise

effect is about $4\times10^{-5}$ $\mathtt{Hz}^2/\mathtt{Hz}$. These effects are negligible, because they are much lower than that of the fiber intrinsic thermal noise. In order to verify if there are other stronger detection noise effects, we gradually decrease the input optical power for a 1 $\mathtt{km}$ fiber interferometer. In this process, we increase the servo's gain to maintain the optimum loop gain. No laser frequency noise degradation is observed until the input optical power reaches a few $\mu$ $\mathtt{W}$. With such an input power, the Johnson noise dominates the detection floor, leading to an additional noise of $\sim 0.1$ $\mathtt{Hz}^2/\mathtt{Hz}$, in agreement with the theoretical analysis.

### 3.4.4 Effect of localized parasitic optical reflections

Parasitic optical reflections of the interferometer are mainly localized at splices, connectors and sharp bends of the fiber. The interaction of these reflected signals with the main signals generate RF signals roughly of the demodulation frequency at the interferometer output. After being demodulated, these RF signals are converted into parasitic disturbances on the interferometer error signal. These disturbances degrade the frequency coherence of the laser, especially when it is frequency swept. This part only discusses the effect of first-order stray reflections, for the effect due to high order reflections is much weaker.

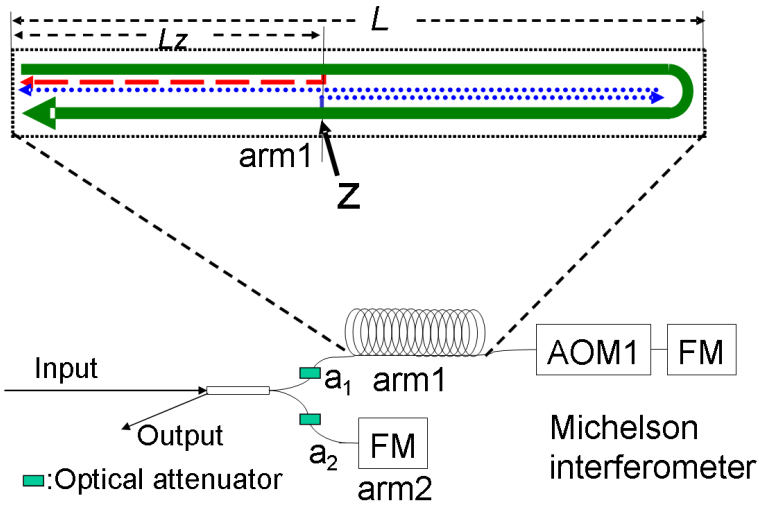


Figure 3.12: Parasitic reflection in the interferometer.

The scheme of parasitic optical reflection is shown in Fig.3.12. A stray reflection occurs at the location $Z$. We introduce the following notation:

- $L_Z$ is the distance from the coupler to the reflection's location.
- $\overrightarrow{E_{r1}(t)}$ is the backward parasitic reflected signal (red dash line) at the interferometer output.
- $\overrightarrow{E_{r2}(t)}$ is the forward parasitic reflected signal (blue dot line) at the interferometer output.
- $\overrightarrow{E_1(t)}$ is the main optical signal from arm1 (wide green line in arm1) at the interferometer output.
- $\overrightarrow{E_2(t)}$ is the main optical signal from arm2 at the interferometer output.
- $C_r(Z)$ is the reflection coefficient in amplitude at Z location. We assume that this parameter is in the same value for both parasitic reflections, because they are caused by the same "mismatch".
- $\alpha_{AOM1}$ is the transmission coefficient of AOM1 in power.
- $\alpha_1$ is the transmission coefficient of arm1's attenuator in power.
- $\alpha_2$ is the transmission coefficient of arm2's attenuator in power.
- We will neglect the optical loss of the fiber, which is typically 0.2 `dB/km` for $1.5\mu$ `m` wavelength laser.

To obtain the maximum detection value, the splitting ratio of the optical coupler is 50/50. The signals at the interferometer output can be expressed in complex representation as:

$$\begin{cases} \overrightarrow{E_1(t)} &= \frac{1}{2}\alpha_1\alpha_{AOM1}E_0\overrightarrow{e_0}e^{2\pi i\int_0^{t-\frac{2nL}{c}}[\nu(t')+2f_{AOM1}]dt'} \\ \overrightarrow{E_2(t)} &= \frac{1}{2}\alpha_2E_0\overrightarrow{e_0}e^{2\pi i\int_0^{t}\nu(t')dt'} \\ \overrightarrow{E_{r1}(t)} &= \frac{1}{2}\alpha_1E_0C_r(Z)\overrightarrow{e_{r1}}e^{2\pi i\int_0^{t-\frac{2nL_Z}{c}}\nu(t')dt'} \\ \overrightarrow{E_{r2}(t)} &= \frac{1}{2}\alpha_1\alpha_{AOM1}^2E_0C_r(Z)\overrightarrow{e_{r2}}e^{2\pi i\int_0^{t-\frac{4nL-2nL_Z}{c}}[\nu(t')+4f_{AOM1}]dt'} \end{cases}, \tag{3.15}$$

where $L$ is the fiber length, $n$ is the fiber refractive index, $E_0$ is the input signal amplitude, $\overrightarrow{e_0}$, $\overrightarrow{e_{r1}}$ and $\overrightarrow{e_{r2}}$ are unit polarization vectors of the signals.

If the laser frequency is swept at a constant rate $\nu'$, that is $(\nu(t) = \nu_0 + \nu' t)$, corresponding to $\Delta\nu_{RF} = -\frac{2Ln\nu'}{c}$, the beat-note signal between $E_1$ and $E_2$ is given by

$$I_{12}(t) = \frac{1}{2}\eta\alpha_1\alpha_2\alpha_{AOM1}E_0^2e^{2\pi i[(2f_{AOM1}-\frac{2Ln\nu'}{c})t+\phi_{12}]} + cc, \tag{3.16}$$

where $\phi_{12}$ is a constant phase. The beat-note signals between $\overrightarrow{E_1}$ and $\overrightarrow{E_{r1}}$ or $\overrightarrow{E_{r2}}$ are given by

$$\begin{cases} I_{1r1}(t,Z) &= \frac{1}{2}\left|\overrightarrow{e_0}\bullet\overrightarrow{e_{r1}}\right|\eta\alpha_1^2\alpha_{AOM1}C_r(Z)E_0^2e^{2\pi i[(2f_{AOM1}-\frac{2(L-L_Z)n\nu'}{c})t+\phi_{1r1}]}+cc \\ I_{1r2}(t,Z) &= \frac{1}{2}\left|\overrightarrow{e_0}\bullet\overrightarrow{e_{r2}}\right|\eta\alpha_1^2\alpha_{AOM1}^3C_r(Z)E_0^2e^{2\pi i[(2f_{AOM1}-\frac{2(L-L_Z)n\nu'}{c})t+\phi_{1r2}]}+cc \end{cases}, \tag{3.17}$$

where $\phi_{1r1}$ and $\phi_{1r2}$ are constant phases. Since $\alpha_{AOM1}$ is about 0.5, we neglect the effect ($I_{1r2}$) of the forward reflection signal. After mixing with the demodulation signal at a frequency of $2f_{AOM1}-\frac{2Ln\nu'}{c}$, $I_{1r1}$ gives a week disturbance on the main error signal produced by $I_{12}$. The detected phase error is the angle between equivalent vectors of $\overrightarrow{I_{12}(t)}$ and $\overrightarrow{I_{12}(t)}+\overrightarrow{I_{1r1}(t,Z)}$:

$$\begin{aligned} \theta(t,Z) &\approx \sin(\phi_0+\tfrac{2L_zn\nu'}{c}t)\left|\tfrac{I_{1r1}(t,Z)}{I_{12}(t)}\right| \\ &= \sin(\phi_0+\tfrac{2L_zn\nu'}{c}t)\left|\overrightarrow{e_0}\bullet\overrightarrow{e_{r1}}\right|\tfrac{\alpha_1C_r(Z)}{\alpha_2}\quad[\mathtt{rad}] \end{aligned}, \tag{3.18}$$

where $\phi_0$ is a constant phase.

In the worst case (i.e. $|\overrightarrow{e_0}\bullet\overrightarrow{e_{r1}}|=1$), this phase error leads to a laser frequency modulation (see Eq.3.1 for low Fourier frequencies)

$$\delta\nu(t,Z)=\frac{\theta(t,Z)}{2\pi\tau}\approx\sin(\phi_0+\frac{2L_zn\nu'}{c}t)\frac{\alpha_1C_r(Z)}{2\pi\alpha_2\tau}\quad[\mathtt{Hz}]. \tag{3.19}$$

We can estimate the localized reflection coefficient using the measured swept laser frequency, based on this equation.

The polarization state of the laser signal can significantly change over a transmission of a few meters, because the SMF-28 fiber does not maintain the polarization state of propagation signal. We assume that the polarization state of the parasitic reflection signal is statically uniformly distributed. The mean power of the phase modulation on the error signal is then

$$\begin{cases} P_\theta(f)\approx\frac{\langle|I_{1r1}(t,Z)|\rangle^2}{2\langle|I_{12}(t)|\rangle^2}=\frac{1}{4}\left[\frac{C_r(Z)\alpha_1}{\alpha_2}\right]^2\quad[\mathtt{rad}^2] \\ f=\frac{2L_Zn\nu'}{c} \end{cases}. \tag{3.20}$$

Consequently, the power of laser frequency noise induced by this stray reflection is

$$\begin{cases} P_\nu(f)=\frac{P_\theta(f)}{(2\pi\tau)^2}=\frac{1}{4}\left[\frac{C_r(Z)\alpha_1}{2\pi\alpha_2\tau}\right]^2\quad[\mathtt{Hz}^2] \\ f=\frac{2L_Zn\nu'}{c} \end{cases}. \tag{3.21}$$

For a non-swept laser, the parasitic reflected signal induces a laser frequency offset. This offset is partly determined by the fiber parameters ($\overrightarrow{e_{r1}}$, $Lz$, $\nu$ and $n$) according to Eq.3.18.

These parameters drift slowly because of temperature fluctuation. An excess frequency noise therefore occurs due to the stray reflection.

This effect of both swept and non-swept lasers can be suppressed by using following methods: reducing the stray reflection coefficients $C_r(Z)$, using a longer reference fiber and inserting more attenuation at the input of the long arm (see Fig.3.12) to decrease the ratio of $\alpha_1/\alpha_2$.

### 3.4.5 Effect of fiber Rayleigh backscattering

Rayleigh scattering is the elastic scattering of light by particles much smaller than the wavelength of light. In a single mode fiber, the Rayleigh scattering is due to the density fluctuations of silica glass. It leads to a loss about 0.15 `dB/km`, corresponding to a loss coefficient $\alpha_L \approx 3.5 \times 10^{-5}$ `/m` in power. A fraction $\alpha_B \approx 1/500$ (Hartog & Gold, 1984) of the scattered optical power is coupled into the backward propagation mode.

First of all, we consider the effect of first-order Rayleigh backscattering (RBS). This distributed reflection can be regarded as a series of reflections from a tiny length fiber located at $L_z \in [0, L]$ with length $\delta l$. Its reflection coefficient in amplitude is then $\sqrt{\delta l \alpha_L \alpha_B}$. According to Eq.3.21, the power of laser frequency noise and its corresponding span of Fourier frequency are

$$\begin{cases} P_\nu[Lz, Lz+\delta l] = \frac{1}{4}\left[\frac{\alpha_1\sqrt{\delta l \alpha_L \alpha_B}}{2\pi\alpha_2\tau}\right]^2 \\ \delta f = |f_{Lz} - f_{Lz+\delta l}| = \left|\frac{2L_Z n\nu'}{c} - \frac{2(L_Z+\delta l)n\nu'}{c}\right| = \delta l \frac{2n\nu'}{c} \end{cases} . \tag{3.22}$$

Consequently, the PSD of the RBS effect can be expressed as:

$$\begin{aligned} S_{\nu-SRBS}(f) &= \frac{P_\nu[Lz, Lz+\delta l]}{\delta f} \\ &= \begin{cases} \left(\frac{\alpha_1}{\alpha_2}\right)^2 \frac{\alpha_L\alpha_B c}{8n}\frac{1}{(2\pi\tau)^2\nu'} & , \quad f \le \tau\nu' = \Delta\nu_{RF} \\ 0 & , \quad f > \tau\nu' \end{cases} . \\ & \quad [\mathtt{Hz}^2/\mathtt{Hz}] \end{aligned} \tag{3.23}$$

The effect of the first-order RBS has the following characteristics:

- The induced frequency noise exists only for $f \le \tau\nu'$;
- The frequency noise PSD is inversely proportional to the sweep rate;
- This effect can be reduced with a longer reference fiber or additional attenuations at the input of arm1.

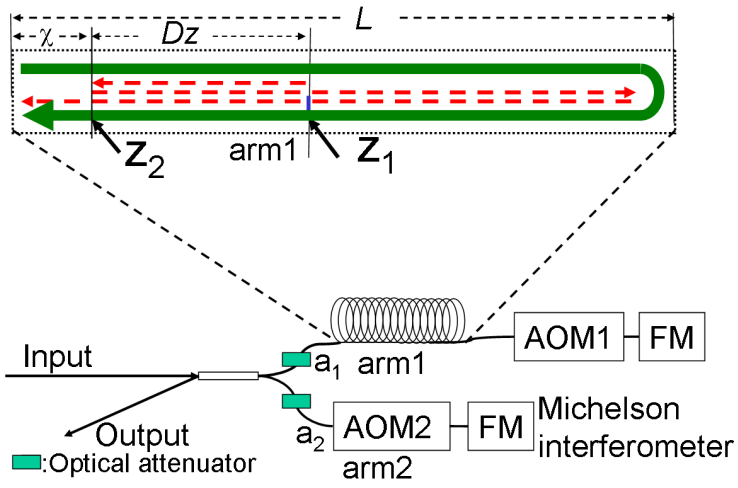


Figure 3.13: Enhanced Michelson interferometer scheme with single stray reflection immunity.

In fact, this effect can be eliminated by distinguishing the main signal of the short arm from the first-order reflection signals. Inserting AOM2 (see Fig.3.13) in the short arm leads to the interferometer output at frequency of $2f_{AOM1} - 2f_{AOM2}$. This frequency is different from any beat-note signal relevant to the single reflections of the long fiber. Consequently, the laser frequency is immune from all first order parasitic reflections, as it is when using the Mach-Zehnder interferometer. However, the double RBS effect can not be avoided in any configuration. It leads to a fundamental frequency noise limitation of the swept laser, which we now consider for the configuration in Fig.3.13, we have three signals at the interferometer output: the mirror reflected signal $\overrightarrow{E_1(t)}$ from arm1 (wide green line in arm1), the mirror reflected signal $\overrightarrow{E_2(t)}$ from arm2, and a summed signal $\overrightarrow{E_{Dz}(t)}$ of all double RBS[1] (red dash line) from arm1 with a distance range of $D_z$ to $D_z + \delta l, D_z \in [0, L)$, because only their beat-note signals are close to the demodulation frequency. These signals are

$$\begin{cases} \overrightarrow{E_1(t)} &= \frac{1}{2}\alpha_1\alpha_{AOM1}E_0\overrightarrow{e_0}e^{2\pi i\int_0^{t-\frac{2nL}{c}}[\nu(t')+2f_{AOM1}]dt'} \\ \overrightarrow{E_2(t)} &= \frac{1}{2}\alpha_2\alpha_{AOM2}E_0\overrightarrow{e_0}e^{2\pi i\int_0^{t}[\nu(t')+2f_{AOM2}]dt'} \\ \overrightarrow{E_{Dz}(t)} &= \frac{1}{2}\alpha_1\alpha_{AOM1}E_0C_{Dz}\overrightarrow{e_{Dz}}e^{2\pi i\int_0^{t-\frac{2n(D_Z+L)}{c}}[\nu(t')+2f_{AOM1}]dt'} \end{cases}, \tag{3.24}$$

where $\overrightarrow{e_{Dz}}$ is the unit polarization vector of this double RBS signal, $C_{Dz}$ is the corresponding reflection coefficient in amplitude. The double RBS occurs either before or after passing the

[1]The optical signal does not pass AOM1 between the two RBSs.

AOM1, therefore, this reflection coefficient is then

$$C_{Dz} = \sqrt{\delta l \times 2 \int_0^{L-Dz} (\alpha_L \alpha_B)^2 dx} = \alpha_L \alpha_B \sqrt{2\delta l (L - Dz)}, \tag{3.25}$$

where $x$ is the distance between the coupler and the close location of the backscatters, as shown in Fig.3.13.

When the laser frequency is swept at a constant rate $\nu'$, corresponding to $\Delta\nu_{RF} = -\frac{2Ln\nu'}{c}$, the beat-note signal between $\overrightarrow{E_1}$ and $\overrightarrow{E_2}$ is given by

$$I_{12}(t) = \frac{1}{2}\eta\alpha_1\alpha_2\alpha_{AOM1}\alpha_{AOM2}E_0^2 e^{2\pi i[(2f_{AOM1}-2f_{AOM2}-\frac{2Ln\nu'}{c})t+\phi_{12}]} + cc. \tag{3.26}$$

The beat-note signal between $\overrightarrow{E_2}$ and $\overrightarrow{E_{Dz}(t)}$ is given by

$$I_{2Dz}(t) = \frac{1}{2}\eta\left|\overrightarrow{e_0}\overrightarrow{e_{Dz}}\right|\alpha_1\alpha_2\alpha_{AOM1}\alpha_{AOM2}C_{Dz}E_0^2 e^{2\pi i\{[2f_{AOM1}-2f_{AOM2}-\frac{2n(Dz+L)\nu'}{c}]t+\phi_2\}} + cc, \tag{3.27}$$

where $\phi_2$ is an initial phase. After demodulation, $I_{12}$ generates a ideal discrimination signal of the laser frequency, while $I_{2Dz}$ causes a week modulation signal at a frequency of $\frac{2nDz\nu'}{c}$.

Using the same approach for calculating first-order RBS effect, the power of laser frequency noise and its corresponding span of Fourier frequency are given by

$$\begin{cases} P_\nu[Dz, Dz+\delta l] = \frac{1}{4}\left[\frac{C_{Dz}}{2\pi\tau}\right]^2 \\ \delta f = |f_{Dz} - f_{Dz+\delta l}| = \left|\frac{2D_Z n\nu'}{c} - \frac{2(D_Z+\delta l)n\nu'}{c}\right| = \delta l\frac{2n\nu'}{c} \end{cases}. \tag{3.28}$$

Then, the frequency noise PSD of double RBS effect is

$$\begin{aligned} S_{\nu-DRBS}(f) &= \frac{P_\nu[Dz,Dz+\delta l]}{\delta f} \\ &= \begin{cases} \frac{(\alpha_L\alpha_B)^2c^2}{32\pi^2n^2}\frac{1}{\tau\nu'}\left(1-\frac{f}{\tau\nu'}\right) & , \quad f \le \tau\nu' = \Delta\nu_{RF} \\ 0 & , \quad f > \tau\nu' \end{cases} . \\ &\quad [\mathtt{Hz^2/Hz}] \end{aligned} \tag{3.29}$$

This effect is inversely proportional to the swept rate of the laser. Down to 300 `kHz/s` swept rate, it is lower than the intrinsic thermal noise effect. This effect is not strong, and it still can be further suppressed by using following methods:

- Thermal treatments of the fiber to decrease the RBS reflection coefficient $\alpha_B$ (Tsujikawa *et al.*, 2000);
- Increase of the interferometer delay, which however may lead to a narrower laser frequency noise control bandwidth;

- modulating the input optical signal (Cranch *et al.*, 2003), which corresponds to an increase of the laser sweep rate $\nu'$. However, this would cause additional frequency noise of the stabilized-laser at the modulating frequency.

### 3.4.6 Effect of the modulation/demodulation signal phase noise

In the modulation and demodulation system, the tunable synthesizer is the most noisy component. Its phase noise causes a laser frequency noise, whose PSD is equal to this phase noise PSD (see Fig.3.10) divided by $(2\pi\tau)^2$ for low Fourier frequencies. This noise at 1 Hz Fourier frequency $\sim 6 \times 10^{-3}$ $\mathrm{Hz}^2/\mathrm{Hz}$ is comparable to the intrinsic thermal noise effect for a 1 km fiber-stabilized laser; it is lower than this fundamental limitation for higher Fourier frequencies. Then, using a 1 km or longer fiber, the laser frequency noise will not be limited by this synthesizer's phase noise for Fourier frequencies higher than 1 Hz. In fact, this effect is over-estimated, because the measured phase noise of the tunable synthesizer was limited by the measurement reference (the commercial synthesizer).

This effect should be lower than the fundamental noise limitation within the control bandwidth. Thus, the phase noise of the tunable synthesizer may need to be reduced when a fiber shorter than 100 m is used. This synthesizer phase noise can be reduced by using a following process:

- Mix the DDS output $\sim 5$ MHz with a $n \times 5$ MHz (e.g. 50 MHz) signal synthesized from the 1 GHz common frequency reference for producing a signal at $\sim 5n \pm$ MHz, where $n$ is an integer;

- Extract only one sideband signal (e.g. $\sim 55$ MHz) by using a tracking oscillator or a narrow bandwidth RF filter;

- Divide the extracted signal by $n \pm 1$ (e.g. 11) with a frequency divider to generate a new synthesized $\sim 5$ MHz signal.

The phase noise of the new synthesized signal would be reduced by a factor of $(n \pm 1)^2$ in power compared with that of the original one, if the additional phase noise due to frequency conversions is negligible.

## 3.5 Experimental performance of fiber-stabilized lasers

The measurement focuses on the frequency noise of fiber-stabilized lasers with different lengths of the reference fiber.

### 3.5.1 A 1 km fiber-stabilized laser

We return to the setup shown in Fig.3.7 of the fiber-stabilized laser with frequency shifted heterodyne Michelson interferometer. Fig.3.14 shows the optical part pictures of a 1 km fiber-stabilized laser, where the fiber, the optical coupler and the FM of short arm are in an aluminum case without being fixed. By monitoring the interferometer output, two control gain bumps are found at 40 kHz and 80 kHz, which are not far from $1/\tau = 100$ kHz. The high-frequency gain bumps indicate a strong gain of the control loop, which guarantees an efficient suppression of the in-loop frequency noise for low Fourier frequencies.

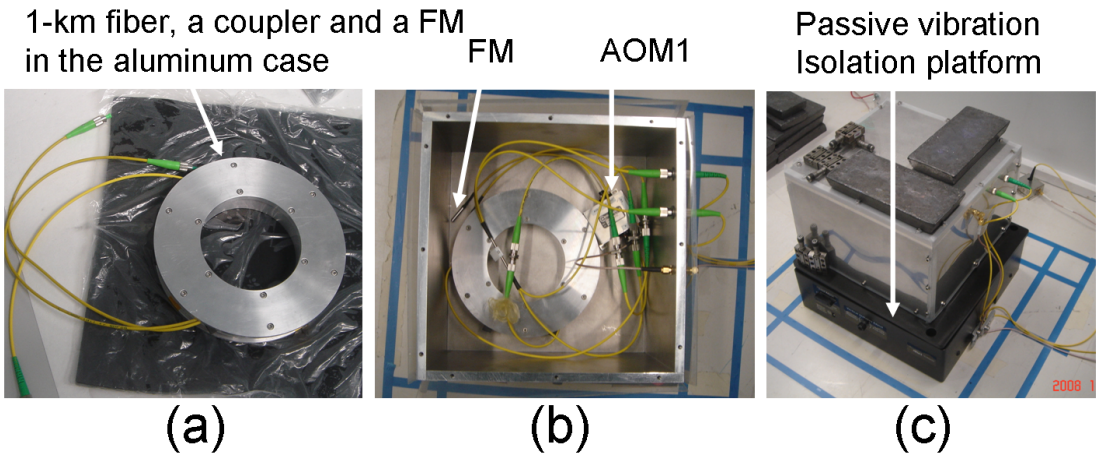


Figure 3.14: Optical part pictures of a 1 km fiber-stabilized laser.

The frequency noise measurement requires a conversion from the optical frequency noise to a measurable signal. The conversion process is:

- First, we beat the optical signal with an ultra-stable cavity-stabilized laser signal (see previous chapter) to generate a beat-note signal in RF domain ($\sim 50$ MHz).
- Second, we shift this beat-note signal to be about $700kHz$ by mixing it with an RF signal produced by a commercial synthesizer.

- After that, the frequency noise of the frequency shifted signal is converted into a voltage signal with a frequency-to-voltage converter, which demands an input frequency range of $0.1 \sim 1$ MHz.

- Finally, we measure the converted laser frequency noise, which is the sum contribution of both lasers, with a **F**ast **F**ourier **T**ransform (FFT) analyzer.

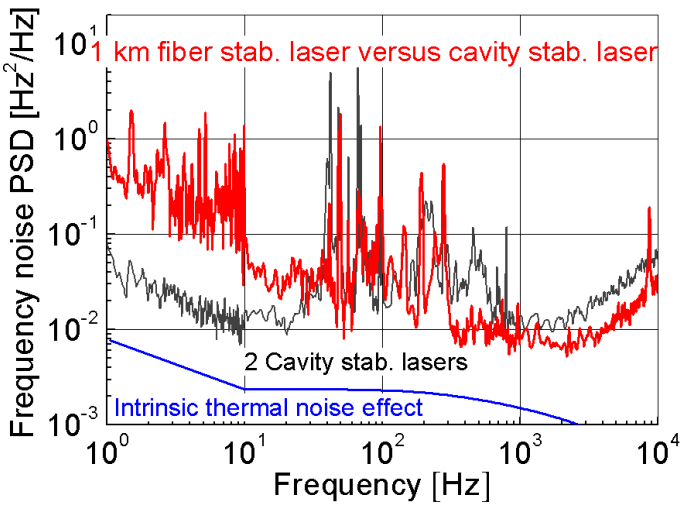


Figure 3.15: Frequency noise PSD of the 1 km fiber-stabilized laser versus cavity-stabilized laser, two cavity-stabilized lasers and the intrinsic thermal noise effect of the 1 km fiber-stabilized laser.

The frequency noise PSD (red solid line) of the beat-note signal between the 1 km fiber-stabilized laser and a cavity-stabilized laser is shown in Fig.3.15. Compared with the frequency noise (black dashed line) of two cavity-stabilized lasers, the frequency noise of the fiber-stabilized laser is at least as low as that of one cavity-stabilized laser for Fourier frequencies ranging from 30 Hz to 20 kHz. The frequency noise PSD (see Fig.3.16) of the free running laser is reduced $\geq 50$ dB for Fourier frequencies lower than 1 kHz. For Fourier frequencies lower than 30 Hz, the fiber-stabilized laser is more noisy than the cavity-stabilized laser. Nevertheless, over the range from 1 Hz to 20 kHz, the frequency noise PSD is well below 1 $\mathrm{Hz}^2/\mathrm{Hz}$.

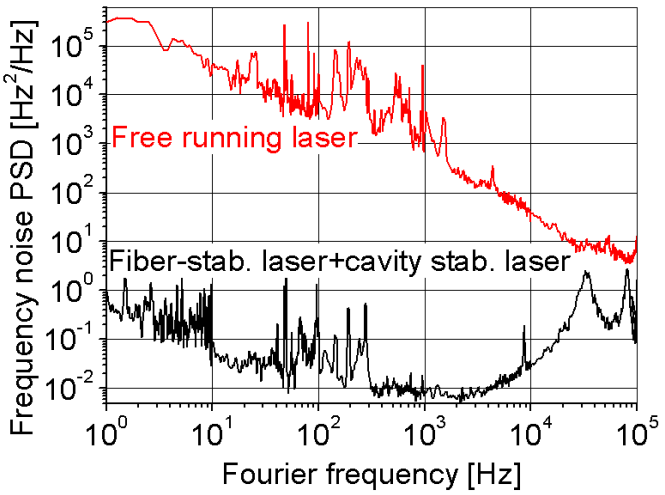


Figure 3.16: Frequency noise PSD of the 1 km fiber-stabilized laser versus a cavity-stabilized laser and the free running laser.

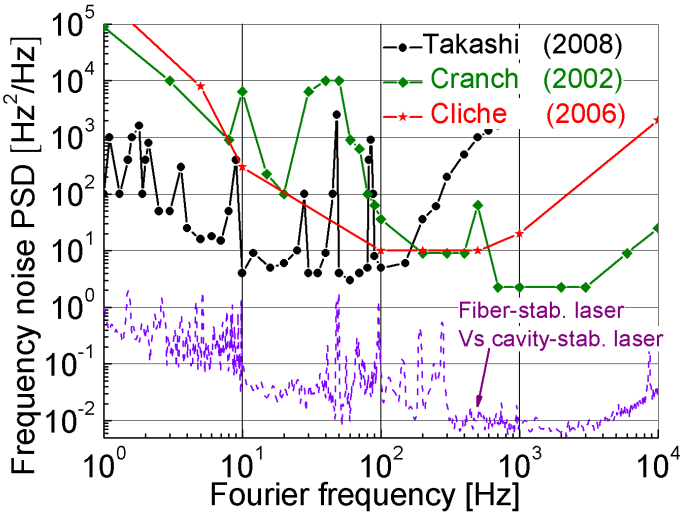


Figure 3.17: Frequency noise PSDs of the 1 km fiber-stabilized laser versus a cavity-stabilized laser and some previous reported ones.

The frequency noise PSD of a few previous fiber-stabilized lasers (Cliche *et al.*, 2006; Cranch, 2002; Takahashi *et al.*, 2008) is well represented by characteristic points in Fig.3.17. Over the range from 1 Hz to 10 kHz, the frequency noise PSD of our laser is at least 20dB lower than that of these lasers. This is mainly due to the use of a longer fiber and a heterodyne detection configuration.

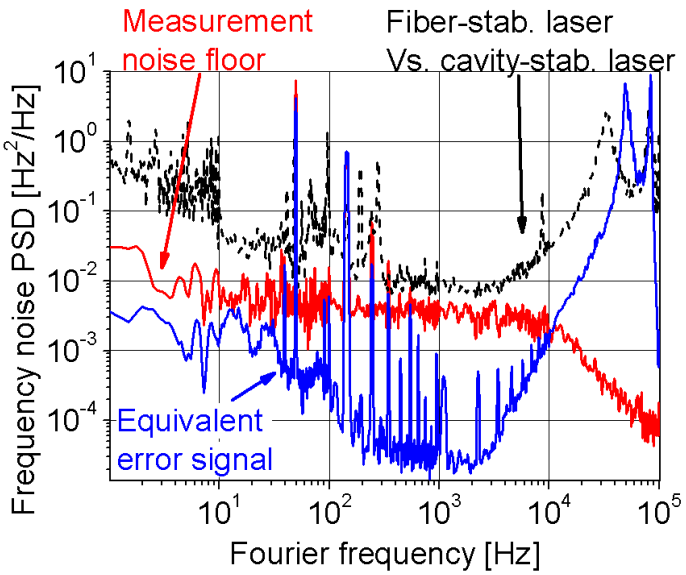


Figure 3.18: Measurement noise floor and the equivalent frequency noise of the error signal.

The equivalent frequency noise of the error signal and the measurement noise floor dominated by the noise of frequency-to-voltage converter are shown in Fig.3.18. For low Fourier frequencies, the measured laser frequency noise is not limited by the measurement noise floor and the in-loop noise; and neither the RF phase noise effect, nor the fundamental thermal effect corresponds to the measured noise level. Then, this noise source should be in the interferometer and induced by environmental noise such as: temperature fluctuations, air flow in the aluminum case and seismic vibration. In fact, considering the noise contribution of reference laser and measurement noise floor, the frequency noise is close to the thermal fundamental limitation ($\sim 1.5 \times 10^{-3}$ $\mathrm{Hz}^2/\mathrm{Hz}$) at a Fourier frequency around 1 kHz.

We measured the frequency noise (see Fig.3.19) of this laser without using the vibration isolation platform. Clearly, the isolation platform efficiently filters out the environmental

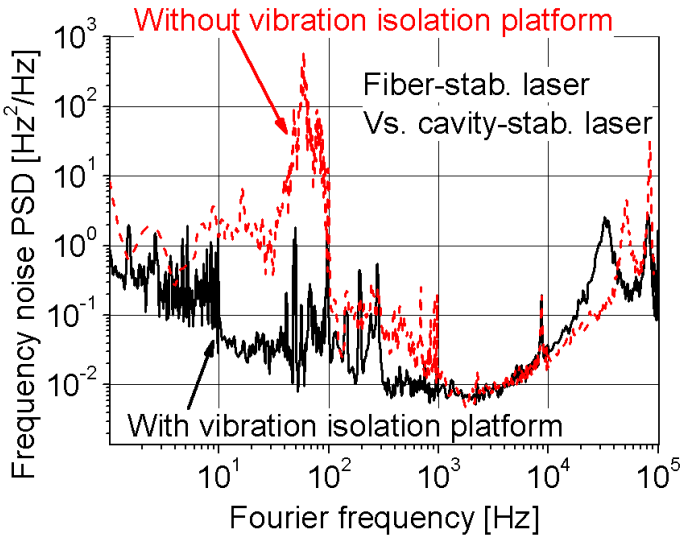


Figure 3.19: Frequency noise PSD of the 1 km fiber-stabilized laser (Vs. a cavity-stabilized laser) with/without a vibration isolation platform.

mechanical noise.

In order to verify if the noise introduced by the AOM, we also lock the laser frequency without the AOM using phase modulation method (see Fig.3.4a). We obtain a same frequency noise in the control bandwidth ($< 20$ kHz). It implies that the laser frequency noise is limited by the noise of the fibers.

The frequency noise is strongly divergent for Fourier frequencies lower than 1 Hz. Those low frequency noises cause the instability of the fiber-stabilized laser to be always higher than $10^{-13}$ at 1 s integration time for a tens of seconds measurement after removing a linear drift of a few kHz/s.

### 3.5.2 A 2.5 km fiber-stabilized laser

Since we believed that the measured frequency noise of the laser was limited by environmental noise, we made a better isolation for a 2.5 km reference fiber. We laid the fiber into an air-sealed can and put multi-layer isolator (MLI) outside the large aluminum box to reduce the thermal effect, which exists mainly in low Fourier frequencies.

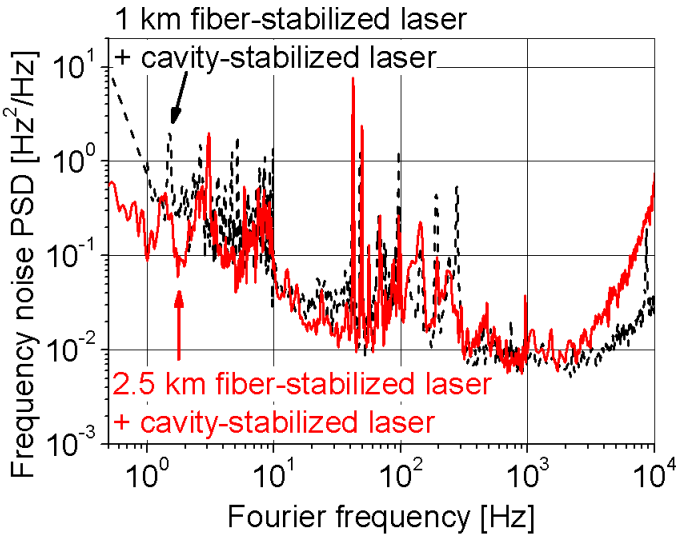


Figure 3.20: Frequency noise PSD of a 1 km/2.5 km fiber-stabilized laser.

The frequency noise (see Fig.3.20) of this fiber-stabilized laser is lower than that of the 1 km fiber-stabilized laser for Fourier frequencies lower than a few Hertz. However, the longer fiber leads to a smaller control bandwidth, resulting in higher laser frequency noise at Fourier frequencies of $2 - 10$ kHz.

The fractional frequency instabilities are also measured by counting the frequency of the beat-note signal between the fiber-stabilized laser and the cavity-stabilized laser. The counter is a dead time free Π-type counter, which is equivalent to a phase recorder. The normalized overlapping Allan deviation is calculated after removing a linear drift of less than 1.5 kHz/s. This deviation (see Fig.3.21) is about $10^{-14}$ at 0.1 s and 1 s integration times. The best result for a 35 s measurement shows a potential instability of a few $10^{-15}$ at 1 s integration time.

## 3.6 Digital lock of the fiber-stabilized laser

In this part, we show that this type of laser can be easily locked to an optical signal or an atomic transition.

The experiment scheme with control parameters is shown in Fig.3.22. The gate-time of

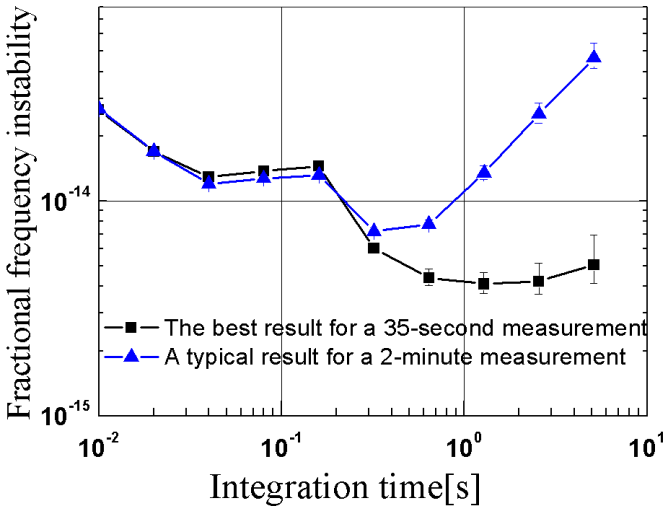


Figure 3.21: Fractional frequency instability of the 2.5 km fiber-stabilized laser after removing linear drifts.

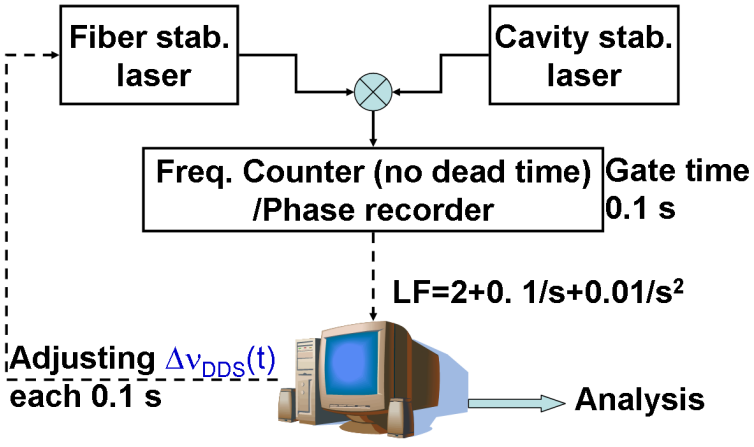


Figure 3.22: Digital phase-lock experiment scheme.

the phase recorder is 0.1 s. The error signal is the difference between a given frequency and the optical beat-note frequency between two lasers. According to this error, the programme gives an adjustment of $\Delta\nu_{DDS}$ and updates it to the DDS each 0.1 s. The control loop has proportional and integral gains with a bandwidth of 2 Hz.

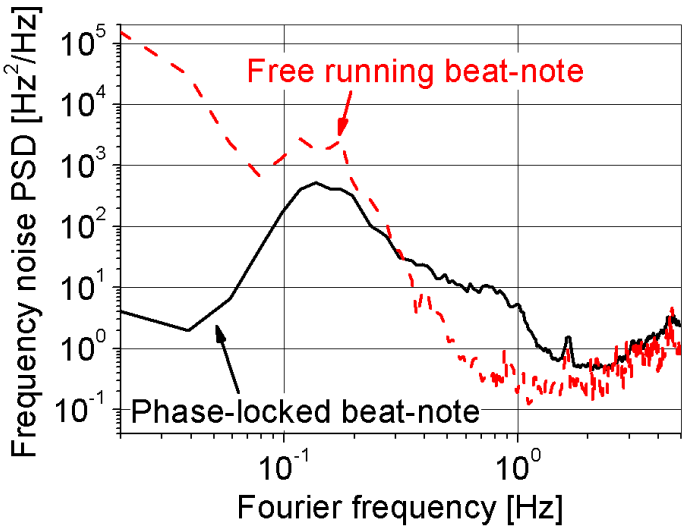


Figure 3.23: The locked and free-running frequency noise PSDs of the optical beat-note (the bump about 0.1 Hz, we attribute to RBS, for no RBS suppression yet).

We obtain the locked and free-running beat-note frequency noise PSD (see Fig.3.23) by Fourier transforming the recorded phase. The locking effect is obvious for low Fourier frequencies. An excess noise occurs in the range from 0.3 Hz to 2 Hz, because of the optical stray reflections of the interferometer. It definitely can be reduced by using single reflection immune configuration (see Fig.3.13).

## 3.7 Experimental performance of the tunable laser

One advantage of fiber-stabilized laser is the large range frequency tunability. This section describes experiments on the laser frequency noise, stability and frequency sweep linearity.

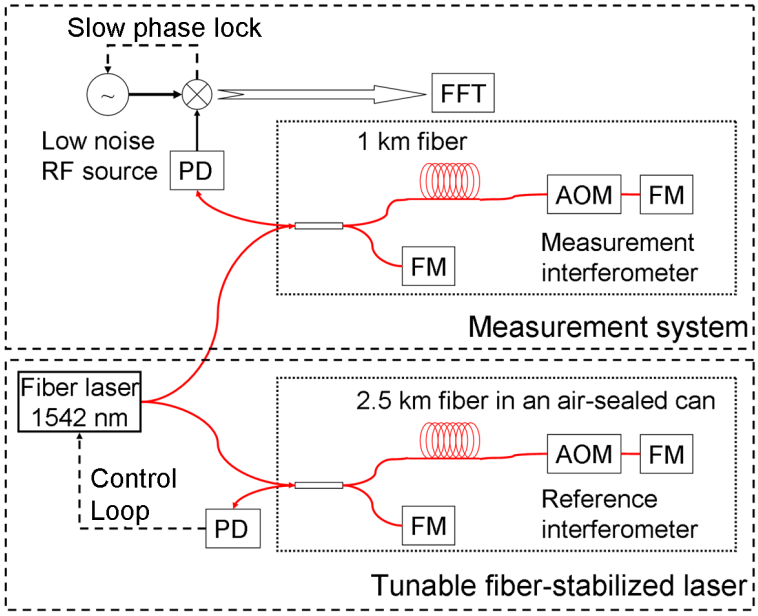


Figure 3.24: Scheme of the tunable laser frequency noise measurement using another demodulation interferometer.

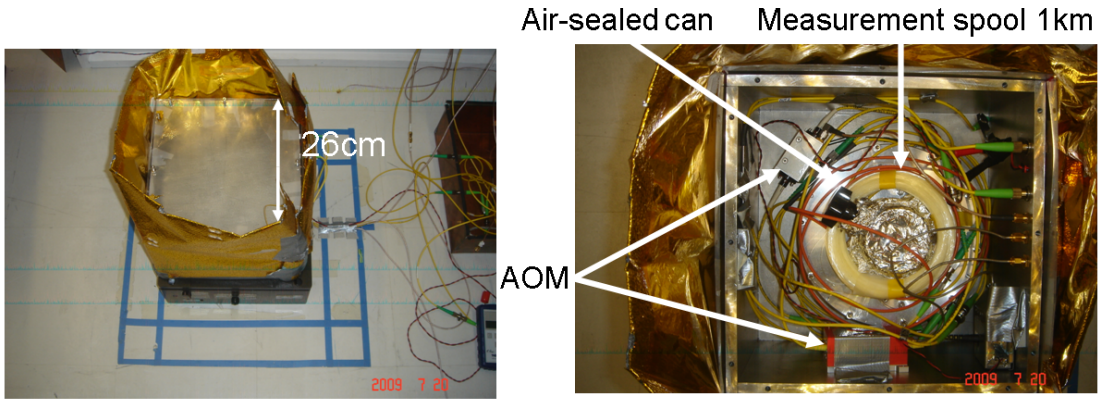


Figure 3.25: Pictures of two interferometers.

### 3.7.1 The frequency noise of the tunable laser

The frequency noise of a frequency-swept laser cannot be simply measured with the same frequency-to-voltage technique used for the non-swept laser. Indeed the operating range of the frequency-to-voltage converter is limited to about 1 MHz, much less than the hundreds MHz sweeping range in our experiment. Extending the range by digital frequency division would severely degrade the measurement noise floor. We present two alternative solutions to overcome the limitation of the frequency-to-voltage conversion technique. One is based on the sampling of the frequency by a high resolution counter, which will be shown later to be interesting for low Fourier frequencies ($< 30$ Hz). In this experiment, a different solution is used. We exploit a second 1 km Michelson frequency-shifted interferometer to convert the laser frequency noise into an RF phase noise with a larger bandwidth. With this technique, a linear optical frequency sweep is converted into a constant RF frequency shift. Fig.3.24 shows the measurement scheme. Fig.3.25 shows photos of the interferometers. The phase noise of the beat-note signal at the output of the measurement interferometer is evaluated with a standard phase noise measurement technique. We use a low phase noise quartz oscillator loosely phase locked on the RF output signal of the measurement interferometer ($\sim 1$ Hz bandwidth). Thus, we obtain the phase noise, which is measured using a FFT analyzer, at the output of the phase detector for Fourier frequencies higher than the control bandwidth. The phase noise PSD is converted into an optical frequency noise PSD using the scaling factor of $1/(2\pi\tau)^2$, where $\tau$ is the measurement interferometer delay. With this technique, the noise PSD is the sum of both interferometer contributions and the measurement noise floor is relatively high, about 2 $\text{Hz}^2/\text{Hz}$. Nevertheless, it is sufficient to reveal the effect of Rayleigh backscattering.

The measured frequency noise PSD is plotted in Fig.3.26 for 1 MHz/s and 2 MHz/s sweeping rates. The spectra are significantly degraded with respect to the non-tuned situation and exhibit a quite peculiar shape characterized by several peaks and two steps. The peaks at 19 Hz, 38 Hz and 44 Hz, we attribute to the effect of localized stray reflection; the steps at 10 Hz and 25 Hz for 1 MHz/s sweep, 20 Hz and 50 Hz for 2 MHz/s sweep, are a clear sign of Rayleigh backscattering in both the reference and measurement fibers. We would expect measured noise due to RBS for $f < \nu'\tau = \nu 2nL/c$ (see section 3.23), which gives $f < 10$ Hz ($L = 1$ km), $f < 25$ Hz ($L = 2.5$ km) at $\nu' = 1$ MHz and $f < 20$ Hz ($L = 1$ km), $f < 50$ Hz ($L = 2.5$ km) at $\nu' = 2$ MHz in exact agreement with our observation. By fitting

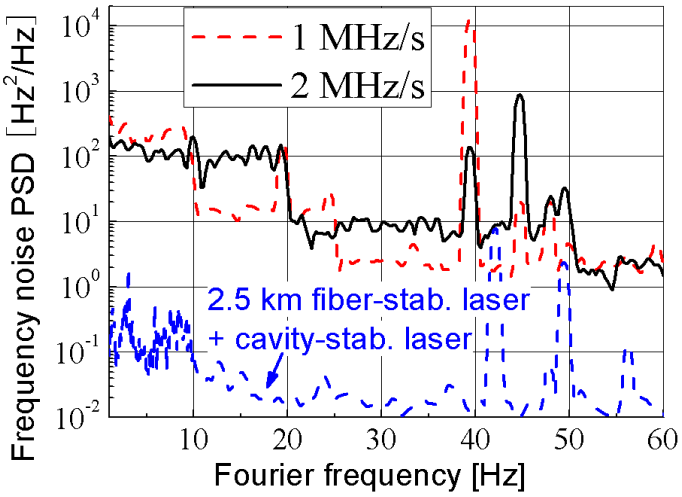


Figure 3.26: Frequency noise PSD of the laser at frequency sweep rates of 1 and 2 MHz/s.

the measurements with Eq.3.23, we found $\alpha_1/\alpha_2 = 0.7$ and $\alpha_1/\alpha_2 = 0.5$ for the measurement and reference interferometer respectively. These values are smaller than 1, which can be explained by

- An additional splicing loss at the input of the long arm;
- An additional fiber loss due to a sharp bend at the input of the air-sealed can for the reference interferometer.

### 3.7.2 First-order stray reflection immune laser

In order to remove the first-order parasitic reflection effects, especially RBS effect, we adopt the single reflection immune configuration for the 2.5 km system (see Fig.3.13). We expect to have a lower frequency noise for low Fourier frequencies. Then, we have to use other measurement method instead of the previous one with 2 $Hz^2/Hz$ noise floor. We record the beat-note frequency between this swept fiber-stabilized laser and the cavity-stabilized laser by using a dead-time free counter model FX80 (KK Messtechnik). This counter is set in the fastest working mode with a gate-time of 1ms. The absolute frequency resolution of this counter is about $\sim 10^{-3}/\tau$, where $\tau$ is the integration time in second 1 mHz at $\tau = 1$ s. This

resolution is much lower than the corresponding deviation between two laser frequencies. As a result, the noise contribution from this counter is negligible. The frequency noise PSD of the beat-note signal is calculated by Fourier transform of the frequency samples. The spectral analysis range is limited to 500 Hz (half the inverse of the counter gate-time) and the spectral power density is degraded by aliasing effect, which produces an measured excess noise of $10^{-4} f^2$ $\mathrm{Hz}^2/\mathrm{Hz}$. This method exhibits a lower noise floor than the previous one for Fourier frequencies lower than $\sim 100$ Hz.

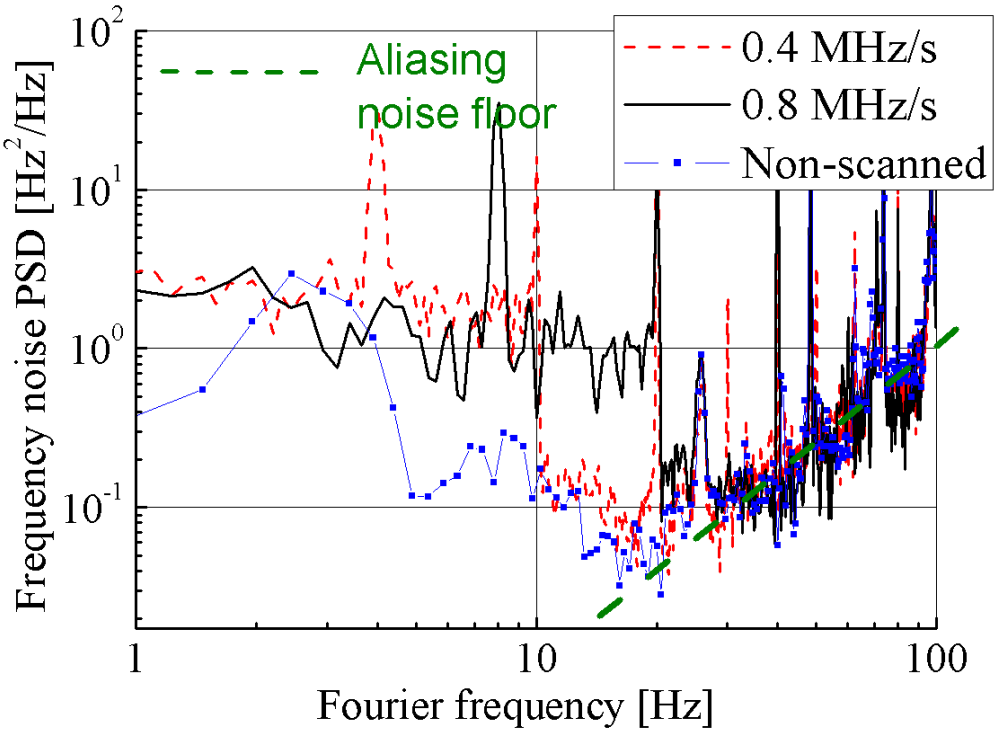


Figure 3.27: Frequency noise of the single-reflection-immune fiber-stabilized laser for various frequency sweep rates, where the aliasing noise floor is the green dashed line.

Fig.3.27 shows the laser frequency noise spectra. In non-swept conditions, the measured noise is close to that of Fig.3.20 up to about 20 Hz. For higher Fourier frequencies, aliasing effect plays a significant role and limits the measurement noise floor. In swept conditions, the noise level reaches the measurement noise floor at Fourier frequencies higher than $\Delta\nu_{RF}$.

At frequency $\Delta\nu_{RF}$, however, each spectrum still exhibits a step, which is characteristic of the single RBS effect (see Eq.3.23). Assuming that a fraction of main signal is reflected twice in the long arm and does not pass through AOM1 between two reflections, it will be in the same frequency and propagation direction as before. Consequently, it contributes to the beat-note signal at frequency $2(f_{AOM1} - f_{AOM2})$ and induces a frequency noise. If the localized reflections in the middle of fiber, the step of induced frequency noise will be at a frequency of $< \Delta\nu_{RF}$ (see Eq.3.28). Then, this noise should be induced by a double reflection, which contains a single RBS and a localized stray reflection close to one end of the reference fiber. This noise follows Eq.3.23 by substituting $(\alpha_1/\alpha_2)^2$ with $2 \times R$, where $R$ is the power reflection coefficient of the localized reflection. The factor of 2 is due to this double reflection occurs either before or after passing through AOM1. Indeed, the RF signal at the interferometer output displayed on a RF spectrum analyzer shows bright lines at $2f_{AOM1}$ and $2f_{AOM2}$ frequencies, which indicates $\sim 1\%$ optical stray reflections located between the optical coupler and AOM1 or AOM2. We attribute this localized reflection to the fiber's sharp bend at the entrance of the air-sealed can. Under this supposition, the calculated laser frequency noise PSD well fits the measured one. In principle, the stray reflections can be reduced to a level of $\sim 10^{-4}$ or better, corresponding to a 20 dB lower frequency noise than this measured one.

The instability of the fiber-stabilized laser (see Fig.3.28) is also measured in this configuration. After removing a linear drift, the swept laser shows instabilities of $\sim 10^{-14}$ for integration time from 0.1 s to 1 s. The frequency instabilities of swept and non-swept laser are same for integration time shorter than 10 ms, corresponding to a phase jitter of $\sim 0.4$ rad. The phase jitter is much smaller than 1. Then, we can track a linear frequency drift optical signal (e.g. a stable signal from a satellite) by using this laser with a control bandwidth of $\sim 100$ Hz.

### 3.7.3 Linearity of the frequency-swept fiber-stabilized laser

For an agile laser, the tuning linearity is an important feature. The chromatic dispersion of the fiber, parasitic reflections, the variation of fiber delay $\delta\tau$ and the change of fiber delay drift $\delta\tau'$ simultaneously degrade the laser tuning linearity.

The fiber chromatic dispersion $D(\lambda)$ leads to a fiber delay change. As a result, the chirping

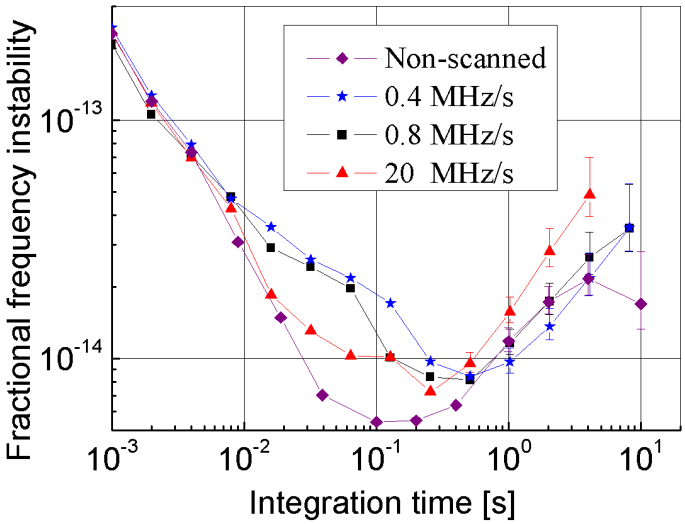


Figure 3.28: Fractional frequency instability of the single RBS immune fiber-stabilized laser for various sweep rates (linear drifts has been removed).

rate becomes

$$\nu' = \frac{\Delta\nu_{RF}}{\tau[1 - \frac{D(\lambda)\lambda c}{n}]}. \tag{3.30}$$

The Sellmeier equation (Sellmeier, 1971) based on Cauchy's equation for modeling dispersion (Jenkins & White, 1981) describes the dispersion of light. For the SMF-28 fiber, the chromatic dispersion is the differentiated Sellmeier equation

$$D(\lambda) \approx \frac{S_0}{4}\left(\lambda - \frac{\lambda_{0D}^4}{\lambda^3}\right), \ \frac{ps}{nm \cdot km}, \ 1200nm \leq \lambda \leq 1600nm, \tag{3.31}$$

where $S_0$ [0.092 $\mathtt{ps/(nm^2.km)}$] is the zero dispersion slope, $\lambda_{0D}(1302\ \mathtt{nm} < \lambda_{0D} < 1322\ \mathtt{nm})$ is the zero dispersion wavelength, $\lambda$ (1542 nm) is the operation wavelength. Eq.3.31 and Eq.3.30 determine a relative non-linearity term $[d\nu'/(\nu' d\lambda) \approx 1.8 \times 10^{-5}\ (\mathtt{nm^{-1}})$ or $d\nu'/(\nu' d\nu) \approx 1.4 \times 10^{-7}\ (\mathtt{GHz^{-1}})]$ due to the fiber chromatic dispersion.

In practice, the residual fiber delay fluctuations due to temperature drift, vibrations and parasitic reflection effects cause much stronger non-linearity than the chromatic dispersion effect for a sweep of span less than $\sim$ GHz. We sweep the laser at a rate of 40.5 MHz/s (see Fig.3.29 trace 1) over a 600 MHz range. In order to clearly demonstrate the sweep linearity, we

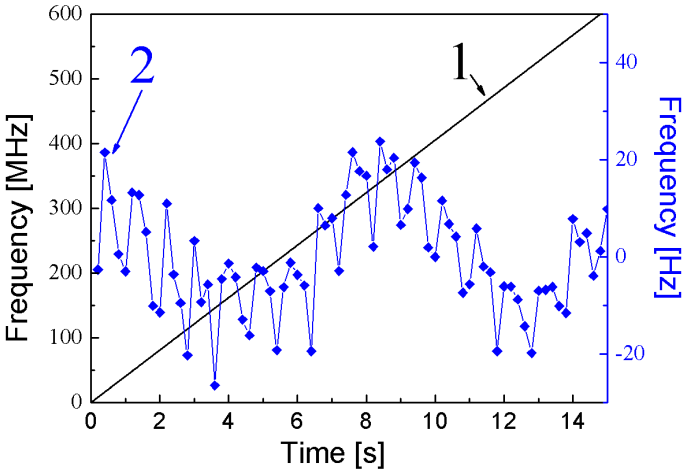


Figure 3.29: The beat-note between swept laser and cavity laser and its fluctuations without the linear drift.

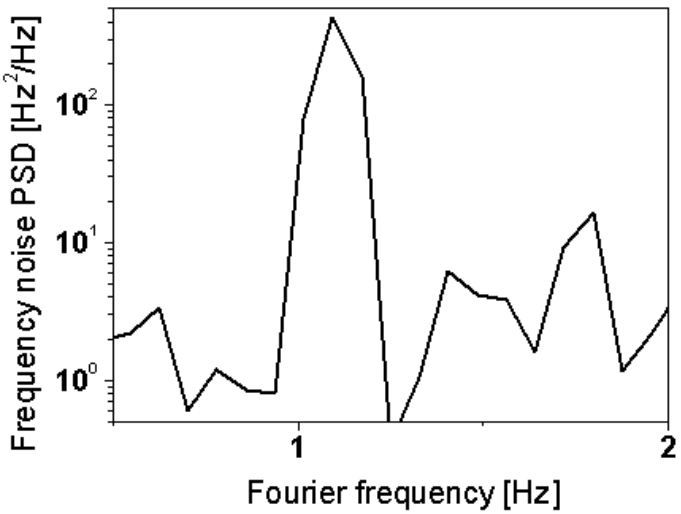


Figure 3.30: The frequency noise PSD of the swept laser.

removed the linear change from the recorded beat-note frequency (see Fig.3.29 trace 2). The

non-linearity is mainly due to the localized stray reflections' effect characterized by periodic variations. This characteristic can be easily found from its plot and spectrum (see Fig.3.30). The periodic variations correspond to parasitic fiber Fabry-Perot interferometers of $\sim 2.5$ m and $\sim 30$ cm with free spectral ranges of $\sim 40$ MHz and $\sim 350$ MHz. The peak-to-peak frequency deviation is about 50 Hz, which is much larger than that due to the fiber chromatic dispersion.

To calibrate the relative sweep accuracy, we have to determine the delay time $\tau$ with the following procedure. We measure for a few seconds the frequency of the beat-note signal with the reference laser using the dead time free counter as shown before. We set sequentially $\Delta\nu_{RF}$ to 40 Hz and $-40$ Hz, and then we experimentally determine the sweep rates. This procedure cancels out the fiber delay time drift during the measurement. The timing of the measurement is very well known and only limited by the counter timebase. The difference of the sweep rates (32.44037 MHz), corresponding to an 80 Hz $\Delta\nu_{RF}$, is then calculated. Using Eq.3.4 we precisely determine $\tau$ to $2.466064 \times 10^{-5}$ s. This accurate calibration holds for a short period of time (about 1 hour) limited by temperature drift. On the long term, an accuracy of $10^{-6}$ or better is achievable with temperature stabilization (in the level of 0.1 K) and/or by using a fiber with lower thermal sensitivity. Then we sweep the laser at different rates ranging from 0.4 MHz/s to 40 MHz/s. The sweep rate error is the frequency difference between the measured and expected sweep rates. The expected rate equals to the sum of a constant laser drift measured prior to the sweep and a linear frequency ramp calculated using the $\tau$ and $\Delta\nu_{RF}$. To avoid the transient error of the laser and the counter degrading the measurement accuracy, hundreds of samplings following the sweep rate shift is removed. Note that the transient time of this laser is estimated to be $< 1$ ms. We evaluate the relative sweep rate accuracy (see Fig.3.31), which is defined by the ratio between the sweep rate error and the nominal sweep rate. It is about 1 part per million (ppm). Each measurement of the sweep rate lasts about 4 s, and the error bars are calculated by using the measured frequency instabilities of the swept laser at 4 s integration time.

This measurement demonstrates the potential of the technique, although the frequency drift ($< 1.5$ kHz/s) still limits the accuracy especially at low sweep rates. With careful temperature control the drift can be reduced at least below 100 Hz/s, or maybe even much less if temperature insensitive fibers become available. Beyond 10 MHz/s, the non-linear error is below 1 ppm. It is worth recalling that with the present drift rate of the laser, this result requires a frequency reference for periodically calibrating the drift (each 5-10 minutes). The

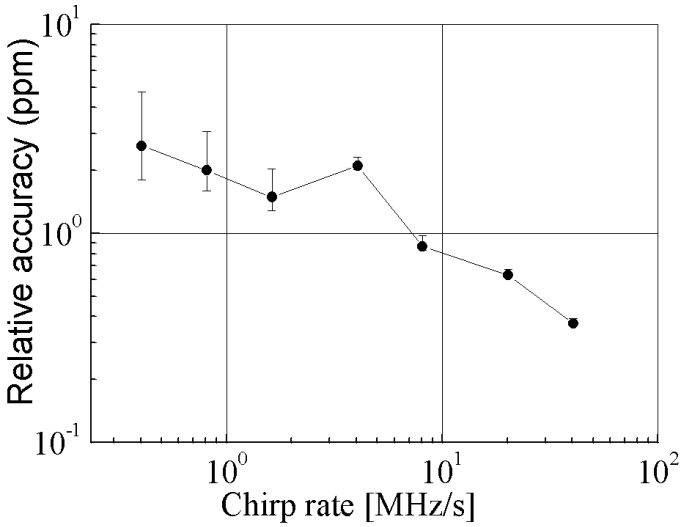


Figure 3.31: The relative chirp rate accuracy with respect to the sweep rate.

reference can be either a molecular transition (Knabe *et al.*, 2009) or a low drift cavity (< a few Hz/s).

The maximum sweep rate of our system is presently about 60 MHz/s limited by the fact that the piezoelectric transducer response was not optimized. We expect that a well engineered setup could achieve at least one order of magnitude larger frequency sweep rates still exhibiting low frequency noise.

## 3.8 The vibration sensitivity of the fiber-spool

The fiber-spool vibration sensitivity $\Gamma$ is the relative variation of the fiber delay time with respect to the acceleration. It is defined as $\Delta\tau/(\tau\Delta V)$, where $\Delta V$ is the acceleration variation in unit of $ms^{-2}$. For the free-standing 1 km fiber-spool used in previous experiments, the vibration sensitivity is $1 - 2 \times 10^{-10}$ /$\mathrm{ms}^{-2}$ at a few Hz Fourier frequency. This result is obtained by comparing simultaneously measured PSD of the laser frequency noise and the fiber-spool vibration at the Fourier frequency ($\sim$ 7 Hz), where the laser frequency noise is dominated by the vibration noise effect. Our ultra-low frequency noise lasers are realized in the condition of using a vibration isolation platform. However, the platform is unsuitable for

many applications. In order to develop a laser with the similar performance as previously shown results without using the platform, the vibration sensitivity of the fiber-spool needs to be reduced. This section discusses a technique for decreasing the fiber vibration sensitivity and several preliminary experiments.

### 3.8.1 Introduction

The first report on an ultra-low vibration sensitivity fiber-spool ($\sim 10^{-11}/ms^{-2}$) is Huang *et al.* (2000). In that experiment, they wound fiber-spools onto two cylinders of same size. The vibration sensitivity of the fiber-spools in the axial direction ($\sim 3 \times 10^{-10}/ms^{-2}$) is tens times higher than that in radial directions ($0.5 - 1 \times 10^{-11}$ /$\mathtt{ms}^{-2}$). In order to reduce the vibration sensitivity, they fixed the two cylinders at symmetric positions with respect to the axial direction and spliced the two fiber-spools into one. In terms of the axial direction, the fiber delay responses of the two parts are inverse each other, leading to a low vibration sensitivity for the total fiber. In fact, a systematic approach based on the same principle (i.e. compensation) has been used for designing ultra-stable cavities mounted vertically (Chen *et al.*, 2006; Ludlow *et al.*, 2007; Notcutt *et al.*, 2005) or horizontally (Millo *et al.*, 2009b; Nazarova *et al.*, 2006; Webster *et al.*, 2007). They study the cavity deformation by using a finite element method. For a well designed 10 $\mathtt{cm}$ cavity, the compensation effect leads to a vibration sensitivity $\leq 10^{-11}$ /$\mathtt{ms}^{-2}$ in all directions. We will follow the same route to reduce the fiber-spool's vibration sensitivity.

Assuming that the fiber delay time variation $\delta\tau$ is proportional to the fiber deformation $\delta l$, a compensation of the fiber deformation is equivalent to that of the delay time. It is nearly impossible to simulate the deformation of a free standing fiber, because it has too many degrees of freedom. However, by tightly winding the fiber onto a rigid support, we can estimate the deformation of the fiber by using a finite element analysis to the support. The winding tension ought to be high enough to guarantee that the fiber deformation $\delta l$ follows the deformation of the support linearly. Moreover, it should not be too high to maintain a low fiber loss and a linear relation between $\delta\tau$ and $\delta l$. With a proper winding tension, the fiber delay variation could be approximately expressed by a function of geometric parameters of the support and its held positions. Theoretically, in this condition we can determine and optimize the vibration sensitivity in the axial direction of the support.

The optimization process may not be so straightforward as that of the cavity design for two reasons. First, the fiber delay variation with respect to the support deformation is more

complex than that for a cavity, the distance between two central points of mirrors. In other words, we need to do an extra step to transform the support deformation into the fiber length variation. A finite element analysis would not enable to determine directly the variation, due to the fact that the fiber is soft and contains several layers with very different mechanical characters. An alternative solution is to evaluate this variation by using an empirical transforming equation obtained from experiments. Second, we want this fiber-stabilized laser to be transportable, which requires a tight holding of the support. Consequently, the forces acting on the support at holding positions are difficult to model.

In Huang's approach, they used two separated supports. We propose to use only one symmetric support held at the middle for simplifying the holding device. ***The target*** is to have a reproducible vibration sensitivity in axial direction comparable with that of other directions ($\leq 10^{-11}$ $/\mathtt{ms}^{-2}$). We will minimize the vibration sensitivity by using following process:

- Step1 : Create a simple ideal model for simulation the fiber vibration sensitivity or refine the model according to the experimental result obtained in step3.
- Step2 : Design supports and determine the holding method for minimizing the vibration sensitivity or verifying the simulation model.
- Step3 : Measure the vibration sensitivity of the fiber-spools wound onto these supports. This process is finished once the target is realized, or else go back to step1.

Further reduction of vibration sensitivity in all directions can be done by choosing the support materials with a higher specific stiffness $E/\rho$, where $E$ is the Young's modulus and $\rho$ is the density, because the deformation of the support is proportional to $E/\rho$ of the material.

### 3.8.2 Experimental setup

Fig.C.2 is the drawing of the support, which is designed following a preliminary finite element analysis. In addition to this support, we built three cylinders with the same profile as the designed support and a hole ($\sim$ 2 $\mathtt{cm}$ diameter) through the axes. All of these supports are made of Titanium, because Titanium is relatively easy to be machined, stiff ($E/\rho \approx 2.6 \times 10^7$ $\mathtt{m}^2/\mathtt{s}^2$) and not sensitive to the temperature fluctuation, which is more than 10 $\mathtt{K}$ during the measurement. We wind SMF-28 fiber (see appendix C) onto the designed support and two cylinders, and polyimide-coated fiber onto the third cylinder. The winding tension

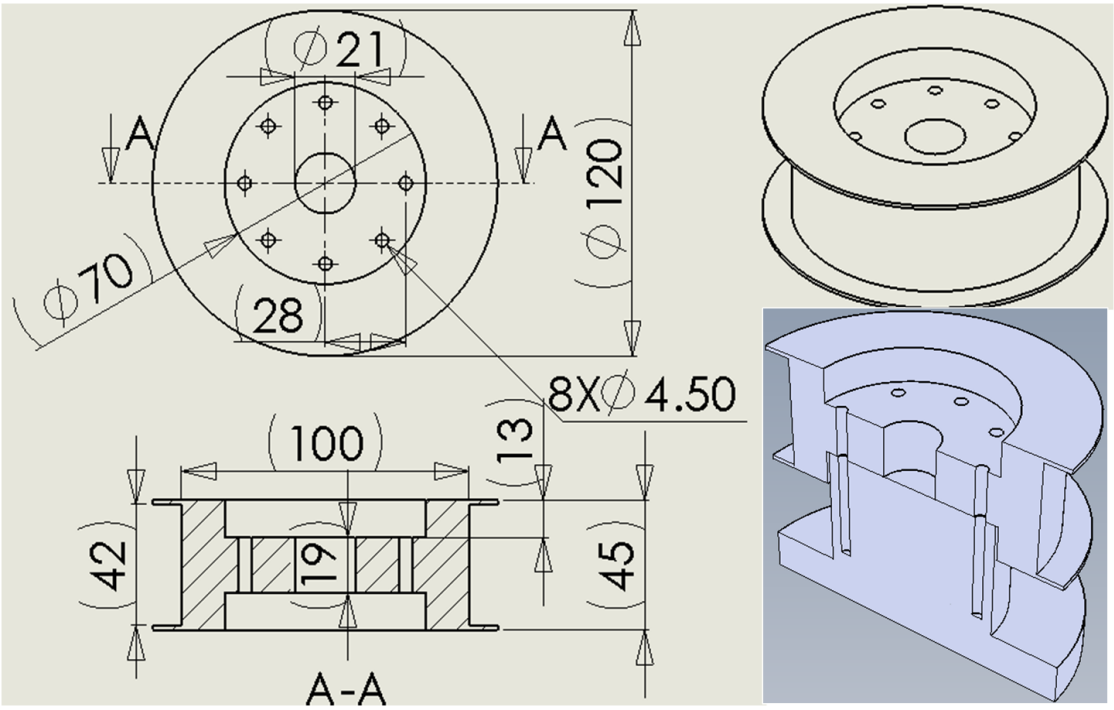


Figure 3.32: Drawing of the designed support (in mm).

is about 0.1 N for all the fiber-spools. We also make use of two 500 m glued fiber-spools to verify the compensation effect due to a symmetric structure.

We did these experiments in Boulder (USA) with colleagues from NIST. Their laboratory has a vibration platform, which can generate white-like vibrations in a given Fourier frequency range. This platform has been used in the vibration sensitivity measurement of RF oscillators, such as optoelectronic oscillators (OEO) (Howe *et al.*, 2007; Taylor *et al.*, 2008). With this platform, we can evaluate the vibration sensitivity in a broad Fourier frequency range instead of a single frequency.

The measurement setup is shown in Fig.3.33. We use a Michelson interferometer with a frequency shifted heterodyne configuration to measure the vibration sensitivity of the fiber-spool. One arm of the interferometer is the measured fiber-spool placed onto the vibration platform, which generates vibrations with the PSD of $S_a(f)$ $(\mathrm{ms}^{-2})^2/\mathrm{Hz}$. The other arm (reference arm) is a fiber-spool with the same length as the measured one. This length-balanced interferometer is not sensitive to the laser frequency noise (see Eq.3.1), allowing a less critical requirement for the laser frequency noise. The AOM is driven by a 95 MHz RF

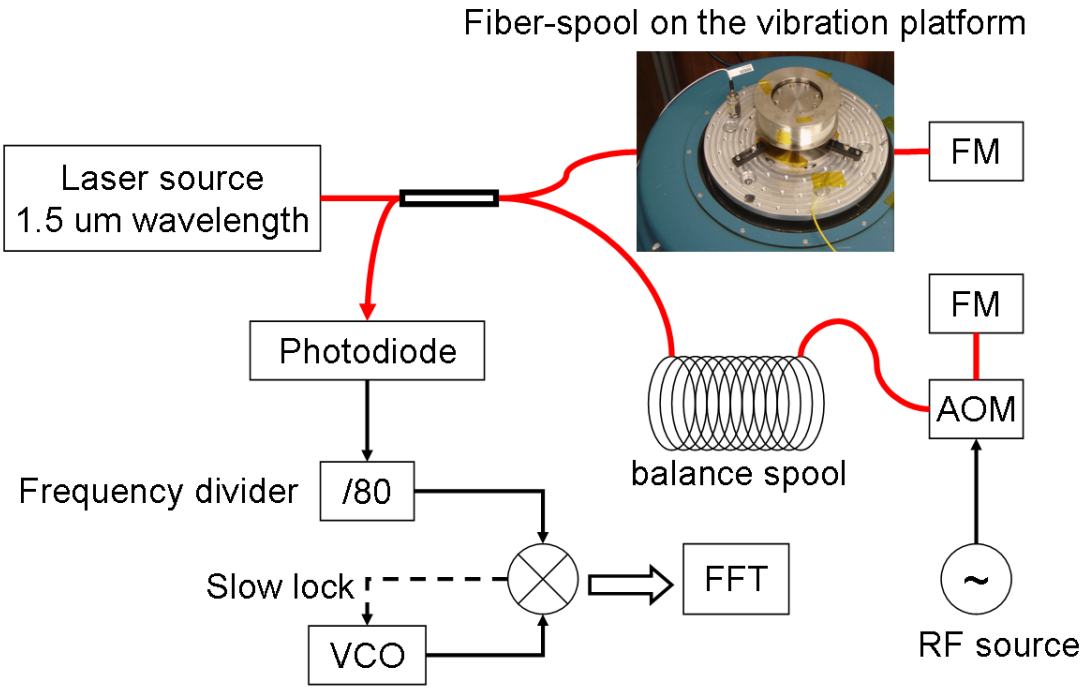


Figure 3.33: The measurement scheme of the fiber-spool vibration sensitivity.

signal, leading to a 190 MHz detected signal. We divide the frequency of the detected signal to 2.375 MHz by using a digital frequency divider (/80), in order to enlarge the detection dynamic range. The phase noise of this 2.375 MHz signal can be measured with a standard phase noise measurement technique. We use a low phase noise commercial synthesizer loosely phase locked on this signal with a control bandwidth of $\sim 1$ Hz. Thus, we obtain the phase noise $S_\phi(f)$ $\mathrm{rad}^2/\mathrm{Hz}$, which is measured by using a FFT, at the output of the phase detector for Fourier frequencies higher than the control bandwidth. We introduce strong vibrations so that the phase noise $S_\phi(f)$ is mainly determined by the effect of vibrations $S_a(f)$. The vibration sensitivity is then

$$\Gamma = \frac{\Delta\tau(f)}{\tau\sqrt{S_a(f)}} = 80\frac{c}{2\pi nL\nu}\sqrt{\frac{S_\phi(f)}{S_a(f)}}\ [/\mathrm{ms}^{-2}], \tag{3.32}$$

where $L$ is the fiber length multiplied by 2.

### 3.8.3 Measurement results

According to previously published results (Howe *et al.*, 2007; Huang *et al.*, 2000; Taylor *et al.*, 2008) and the preliminary finite element analyses, the vibration sensitivity in the axial direction of the rigid support is one to two orders of magnitude higher than that in the radial direction. Therefore, we only focus on the vibration sensitivity of the fiber-spool in this direction.

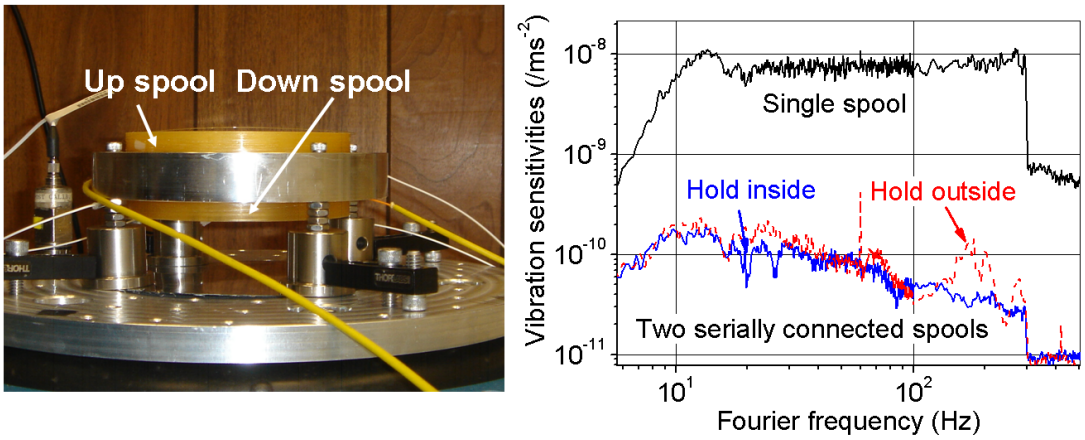


Figure 3.34: The two glued fiber-spools and their vibration sensitivities.

The first experiment aims at proving the compensation effect by using a symmetric structure. We glue two 500 m glued fiber-spools onto two sides of an aluminum disc (see Fig.3.34). Due to the symmetric structure, the vibration responses in axial (vertical) direction of the fiber-spools are inverse. When the two fiber-spools are spliced in series, the vibration sensitivity shown in Fig.3.34 is much lower than each of them. Over the measuring range from 10 Hz to 300 Hz, the vibration sensitivity ($\sim 10^{-10}$ /ms$^{-2}$) is reduced more than 40 times. This vibration sensitivity is stable and reproducible, nearly independent of the holding positions on the disc. Clearly, the symmetric structure efficiently compensates the fiber-spool vibration sensitivity. The reducing ratio is a few tens, which is comparable to the ratio of the sensitivities between axial and radial directions. It demonstrates that using a highly symmetric structure for axial direction can realize our target. Note that the winding direction is irrelevant, only the holding geometry matter.

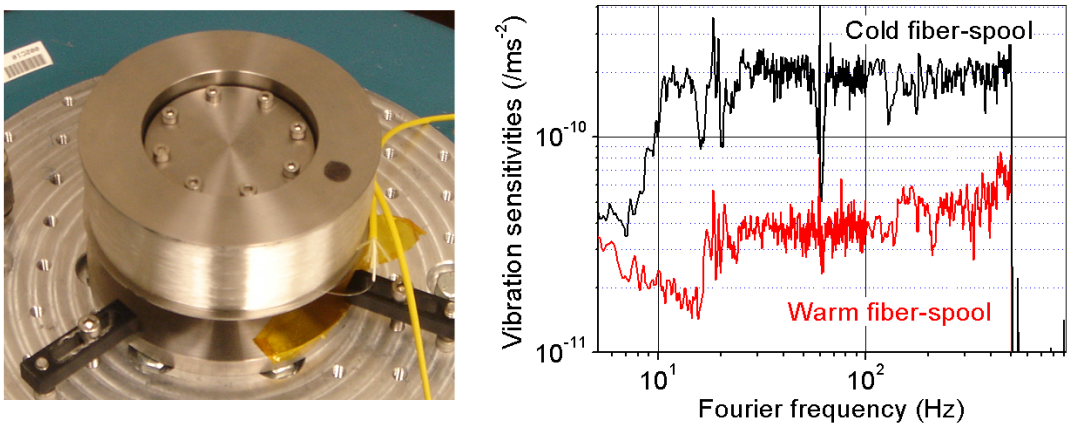


Figure 3.35: The measured fiber-spool and its vibration sensitivity.

The second experiment is to measure the vibration sensitivity of a 2.1 km SMF-28 fiber wound onto the designed support with 0.1 N winding tension. This support is tightly fixed onto an Invar post by using 8 screws (see Fig.C.2 and Fig.3.35). The measured vibration sensitivity is about $2 \times 10^{-10}$ /ms$^{-2}$ in the measurement frequency range of $10 - 500$ Hz at the onset of the experiment. We continually redo the same measurement, while the operation temperature rises up more than 10 K during hours. The temperature increase is due to a great amount of heat energy produced by the operating vibration platform. Ultimately, the vibration sensitivity gradually decreases to the level of about $4 \times 10^{-11}$ /ms$^{-2}$ in the Fourier frequency range of $20-500$ Hz. Furthermore, putting hundreds grams mass on the top surface (not center) of the support causes an obvious sensitivity variation. A reasonable explanation is that the 0.1 N winding tension is not enough to make the fiber length variation well following the cylinder deformation. As a result, the temperature drift or the force action leads to a winding tension variation, resulting in a change of the vibration sensitivity. We suppose that a higher temperature corresponds to a tighter fiber tension. Thus, a tighter winding may lead to a lower vibration sensitivity.

In the third experiment, we rewind the fiber onto the designed support with a 0.75 N wound tension. The losses of the fiber-spool are less than 1 dB, which is acceptable. The vibration sensitivity shown in Fig.3.36 is about $7 \times 10^{-11}$ /ms$^{-2}$. The white-like vibration sensitivity is a signal, indicating that a better compensation can be done. This vibration sensitivity

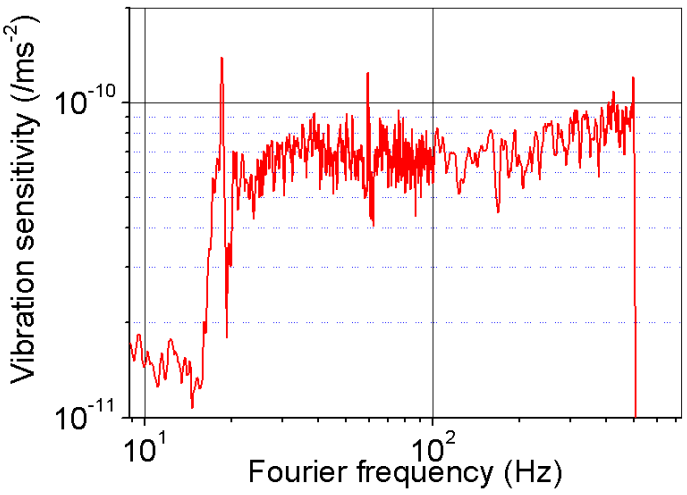


Figure 3.36: The vibration sensitivity of fiber-spool with a 0.75 N tension.

shows very robust features such as: it is independent of the temperature fluctuation. It is also independent of putting mass on the top surface of the support and roughly same for many times measurement (even mounting the support upside-down). These robust features indicate that the fiber-spool delay time variation well follows the cylinder deformation and more tension would not improve. This result tells us that the feasible winding tension should be between 0.1 N and 0.75 N. We also turned the fiber spool over (upside-down) and held at different position (see Fig.3.37). The measured vibration sensitivities are in the range of from $\sim 2 \times 10^{-11}$ /ms$^{-2}$ to $\sim 7 \times 10^{-11}$ /ms$^{-2}$. Major differences are induced by asymmetrically winding of spool. Compared with the target, these vibration sensitivities still need to be reduced by a factor of a few to ten. Nevertheless, they are close to that of a 10 cm ultra-stable cavity at the current state-of-the-art of $\sim 10^{-11}$ /ms$^{-2}$(Ludlow *et al.*, 2007; Millo *et al.*, 2009b; Nazarova *et al.*, 2006; Seel *et al.*, 1997; Webster *et al.*, 2007). Note that the specific stiffness $E/\rho$ is similar for Titanium and cavity-used Ultra-Low Expansion (ULE) glass.

We also measured the vibration sensitivity of a 650 m ployimide-coated fiber, which is wound onto a cylinder with 0.1 N winding tension. This kind of fiber has the same core and cladding dimensions as the SMF-28 fiber as shown in Appendix C. For protection, SMF-28 fiber has three extra layers from inner to outer: extremely soft coating $\sim 30$ $\mu$m, hard coating $\sim 30$ $\mu$m and tight buffer $\sim 325$ $\mu$m. However, ployimide fiber just has one layer of thin ($\sim 20$ $\mu$m)

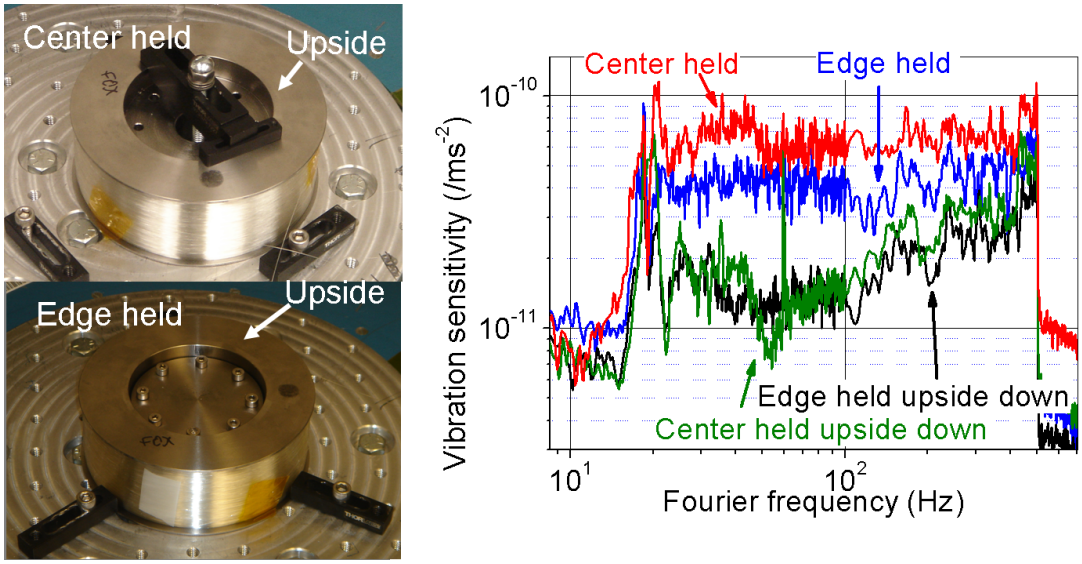


Figure 3.37: The fiber-spool with other held methods and its vibration sensitivity (0.75 N 2.1 km SMF-28 fiber spool).

and very hard polyimide coating out of cladding as shown in Appendix C, which allows it working in vacuum or high temperature environments. We suppose that the polyimide-coated fiber in similar manner as a bare fiber, may be easier to be analyzed with a finite element method. Fig.3.38 shows the holding method and the vibration sensitivity of the polyimide-coated fiber-spool. Over the measured range of $20-500$ Hz, the vibration sensitivity is mainly in the range of $10^{-11}$ /ms$^{-2}$. However, the sensitivity is strongly frequency dependent, when the cylinder is held in the center (see A of Fig.3.38). It should be due to the fact that the winding tension of 0.1 N is not enough.

Finally, we measured the vibration sensitivity of fiber-spools with different length and holding way. These fiber-spools are wound with different tensions (0.75 N and 0.1 N) onto cylinders. The measured vibration sensitivities are in the range of $3\times10^{-10}$ to $1.5\times10^{-9}$ for Fourier frequencies of $20-500$ Hz.

In summary, the preliminary results indicate some positive conclusions:

- The symmetric compensation effect could be efficient enough to realize a reproducible vibration sensitivity of the fiber-spool($\leq 10^{-11}/ms^{-2}$) in axial direction compatible with that of other directions.

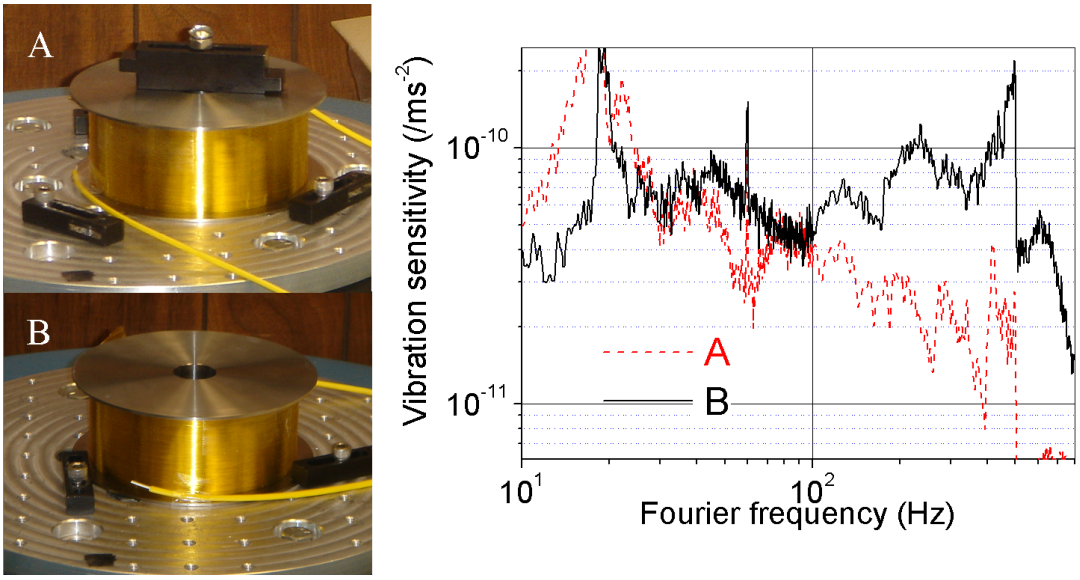


Figure 3.38: The polyimide-coated fiber-spool and its vibration sensitivity (650 m 0.1 N), A: center holding, B: edge holding.

- The feasible winding tension exists for SMF-28 fiber; the optimum tension should be a value in the range of [0.1,0.75] Newton.
- The measured vibration sensitivity ($\sim 7 \times 10^{-11}$ /ms$^{-2}$, see Fig.3.36) is stable and frequency independent when the designed support is fixed on the Invar post at the center. And it definitely can be further minimized in this configuration.

In addition, we have several extra measurement results, which may be helpful for establishing the simulation model. It is worth noting that there are uncertainties (e.g. winding quality) in these experiments, making the relation between support deformation and fiber delay variation complex. However, the vibration sensitivity is only $\sim 10$ times higher than the target and further improvement can definitely be done. We believe that our target can be achieved in near future.

## 3.9 Summary and prospectives

This chapter has introduced the technique of laser frequency stabilization on a fiber delay, analyzed the various noise effects and given the noise rejection methods. With appropriate

configuration and fiber length, our fiber-stabilized lasers show following features:

- Ultra-low frequency noise: their frequency noise PSDs are more than 20 dB below those of the previous published fiber-stabilized lasers, and comparable with that of an ultra-stable cavity-stabilized laser for Fourier frequencies higher than 30 Hz.
- Ultra-high sweep linearity: 50 Hz peak-to-peak non-linear error in a $\sim$ 600 MHz sweep range.
- High short-term stability: with a 2.5 km reference fiber in an air-sealed can, the instability of both non-swept and swept lasers is about $10^{-14}$ for $0.1 - 1$ s integration times after removing the linear drift.

Furthermore, this laser is simple, robust and low cost.

These fiber-stabilized lasers can be used in many applications, including optical tracking oscillator (including phase coherent tracking of optical signal from a satellite)(Wolf *et al.*, 2009), optical frequency-modulated continuous-wave reflectometry (Geng *et al.*, 2005), low noise interferometric sensors (Hough & Rowan, 2005), optical processing of RF signals (Lavielle *et al.*, 2003) and so on.

In all experiments, the reference fiber is placed onto a vibration isolation platform, which is not convenient for manipulating. Furthermore, once the thermal effect is greatly suppressed, the vibration noise effect may not be negligible for low Fourier frequencies even with a vibration isolation platform. Especially, one want to use the laser used in a noisy environment. We have done a few preliminary experiments for reducing the fiber vibration sensitivity. These measured fiber-spools have shown the vibration sensitivity in the range of high $10^{-11}$ /ms$^{-2}$. The result implies that a $\leq 10^{-11}$ /ms$^{-2}$ vibration sensibility is achievable.

Considering the drift of the non-swept laser, the instability of the 2.5 km fiber-stabilized laser is in the range of $10^{-12}$ at 1s integration time. This instability can definitely be reduced by a factor of 10 by adding additional thermal isolations for the interferometer. Even in this condition, the laser instability is still much higher than that of an ULE glass cavity-stabilized laser. This is due to the fact that the temperature coefficient of SMF-28 fiber is about $10^{-5}$ /K, which is $\geq 10^3$ times higher than that of ULE spacer. This effect can be reduced by periodic calibrations with a more stable reference. However, the best solution should be reduction of the fiber temperature coefficient. A possible approach is use of a low temperature coefficient fiber or different type fibers canceling out their temperature drift effect.

# Chapter 4

# Long distance ultra-stable optical frequency transmission

This chapter is devoted to the technique of ultra-stable optical frequency transmission via optical fiber networks. In the first part, I explain the principle and limitations of the noise cancellation. Then, I introduce the experimental setup and show several experiments of the optical link, including optical frequency transfers over 86 km, $2 \times 86$ km and 108 km urban fiber networks. Finally, a 150 km + 150 km cascaded link with a repeater station is demonstrated over optical fibers simultaneously carrying Internet data traffic.

## 4.1 Introduction

Ultra-stable frequency transmission between distant laboratories is required by many applications: time and frequency metrology (Amy-Klein *et al.*, 2004; Bauch *et al.*, 2006; Ludlow *et al.*, 2008; Musha *et al.*, 2008; Terra *et al.*, 2009), fundamental physics (Shelkovnikov *et al.*, 2008), particle accelerators (Pellegrini, 2006; Wilcox *et al.*, 2009), the synchronization of deep-space network and astronomy antenna arrays (Calhoun *et al.*, 2007; Layland & Rauch, 1997). The field of optical frequency standards is rapidly progressing, and the fractional uncertainty level of $10^{-16} - 10^{-17}$ has been already demonstrated (Campbell *et al.*, 2008; Chou *et al.*, 2010). And these accurate frequency standards are complex, expensive and bulky equipments, and usually located in different countries. As a consequence, an ultra-stable frequency transmission with a fractional frequency instability of $10^{-18}$ (or below) at one day is required to compare the frequency of present (and future) optical clocks over large distances.

## 4. LONG DISTANCE ULTRA-STABLE OPTICAL FREQUENCY TRANSMISSION

Long-distance frequency comparisons of ultra-stable clocks enable to evaluate not only the performance of these clocks, but also the geoid fluctuations. The geoid was mapped by years of observations of terrestrial gravity and satellite orbits. The altitude is estimated with a typical uncertainty of $30 - 50$ cm per year, corresponding to a frequency gravitational redshift change of a few $10^{-17}$ (Kleppner, 2006; Margolis, 2010; Pavlis & Weiss, 2003).

The mature satellite-based links for frequency comparison show a fractional instability of about $10^{-15}$ for one day integration. Currently developed satellite-based links for advanced space missions, Atomic Clocks Ensemble in Space (ACES) (Cacciapuoti & Salomon, 2009) and Time Transfer by Laser Link (T2L2) (Samain *et al.*, 2009), have been designed with the goal of comparing frequency in the level of $< 10^{-16}$ at one day. However, the performance of these free-space links is also determined by the location and atmosphere conditions. Nevertheless, ground links with better stability are required to compare the frequency of the best optical clocks in the near future.

Fibre networks are the best candidates for the ground links to transfer an ultra stable frequency, due to their good intrinsic stability, low loss, reliability and wide accessibility. There are three methods to transfer frequency via the fiber networks (Foreman *et al.*, 2007a): amplitude modulation (AM) frequency transfer of a radio frequency (RF) or microwave signal. (Calhoun *et al.*, 2007; Daussy *et al.*, 2005; Kumagai *et al.*, 2009; Lopez *et al.*, 2008, 2010a; Lutes, 1980; Narbonneau *et al.*, 2006; Shillue *et al.*, 2004; Wilcox *et al.*, 2009; Ye *et al.*, 2003), optical frequency comb transfer (Holman *et al.*, 2004; Kim *et al.*, 2008; Marra *et al.*, 2010) and optical carrier frequency transfer (Foreman *et al.*, 2007b; Grosche *et al.*, 2009; Hong *et al.*, 2009; Jiang *et al.*, 2008; Kéfélian *et al.*, 2009b; Lopez *et al.*, 2010b; Ma *et al.*, 1994; Musha *et al.*, 2008; Newbury *et al.*, 2007; Terra *et al.*, 2009, 2010; Williams *et al.*, 2008). The optical carrier frequency transfer presents the lowest instability among these methods. Thus, it is suitable to realize long-distance ultra-stable frequency transfers at $\sim 1000$ km scale or even longer, and compare the frequencies of optical clocks in all Europe. Usually, the transferred laser signal is at a wavelength of $\sim 1.5$ $\mu$m, corresponding to the lowest fiber transmission loss window ($\sim 0.2$ dB/km). Recently, optical links have been developed in several countries. They all exhibited a fractional frequency instability of $\sim 10^{-19}$ or lower for $100 - 200$ km frequency transfer, although not all evaluated with an equivalent statistics tool.

We transferred the frequency of an ultra-stable laser signal over 86 km and $2 \times 86$ km urban dedicated fiber. The compensated link showed a fractional frequency instability of a few $10^{-16}$ at 1 s integration time and a few $10^{-19}$ at $10^4$ s (Jiang *et al.*, 2008). In addition,

we transferred the same optical frequency over 108 km link using a section of public fiber networks. This link presented a fractional frequency stability of a few $10^{-16}$ at 1 s and below $10^{-19}$ at $10^4$ s (Kéfélian *et al.*, 2009b). This experiment opens the way of using the public telecom networks to transfer the ultra-stable optical frequency. Recently, we transferred optical signal over a $150km + 150km$ cascaded multiplexed link with a repeater station. This link showed a stability of $3 \times 10^{-15}$ at 1 s and $4 \times 10^{-19}$ at $10^4$ s (Lopez *et al.*, 2010b). The objective is development of a $\sim$ 1000 km optical link with a $\leq 10^{-18}$ instability at one-day integration time.

## 4.2 Principle of the optical link

This part explains the operational principle of the optical link, and gives detailed analyses on the noise cancellation technique.

### 4.2.1 Introduction

The goal of an optical link is to reproduce a local frequency reference at the remote end of the fiber link. Several noises accumulated along the optical fiber degrade the transferred frequency signal by perturbing its phase. For instance, thermal and mechanical fluctuations change the optical path through the fiber, thus inducing fluctuations of the propagation delay. The delay fluctuations correspond to phase/frequency variations of the transferred signal.

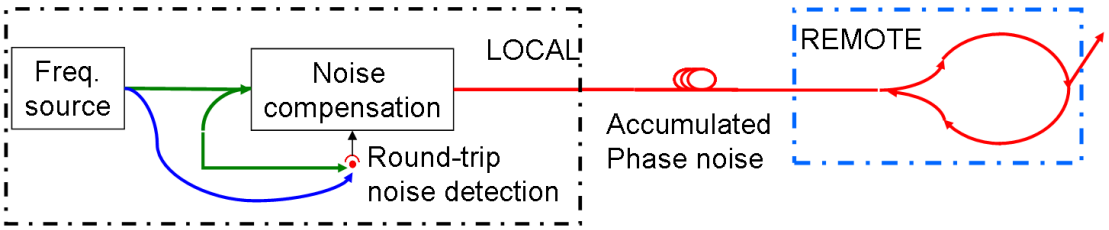


Figure 4.1: General scheme for the noise compensation of frequency transfer.

The so-called "Doppler cancellation technique" was originally used in the free space frequency transmission about 30 years ago (Vessot *et al.*, 1980). Optical frequency transfer with the same principle was done later (Ma *et al.*, 1994). The scheme is shown in Fig.4.1, where the link can be the optical fiber or any other media. It is actually a general scheme of

Doppler noise cancellation for the signal transmission. The local system compares the round-trip signal to the local signal, therefore, measures the sum of the forward and backward phase fluctuations of the propagating signals. The phase fluctuation of the fibre is mainly induced by the length and refractive index variations, which equally impact the forward and backward propagation phase approximately. Therefore, phase fluctuation of forward transmission is half of the round-trip phase fluctuation, and it can be measured and compensated.

This noise cancellation technique enables to compensate laser phase fluctuations which are identical for both propagation directions. However, for some noises [e.g. due to the polarization mode dispersion (PMD)] this is not case, leading to an imperfect noise cancellation. Moreover, fibre delay leads to a detection delay, resulting in limitations on the control bandwidth and noise rejection ratio (Newbury *et al.*, 2007).

### 4.2.2 Link noise determination and compensation

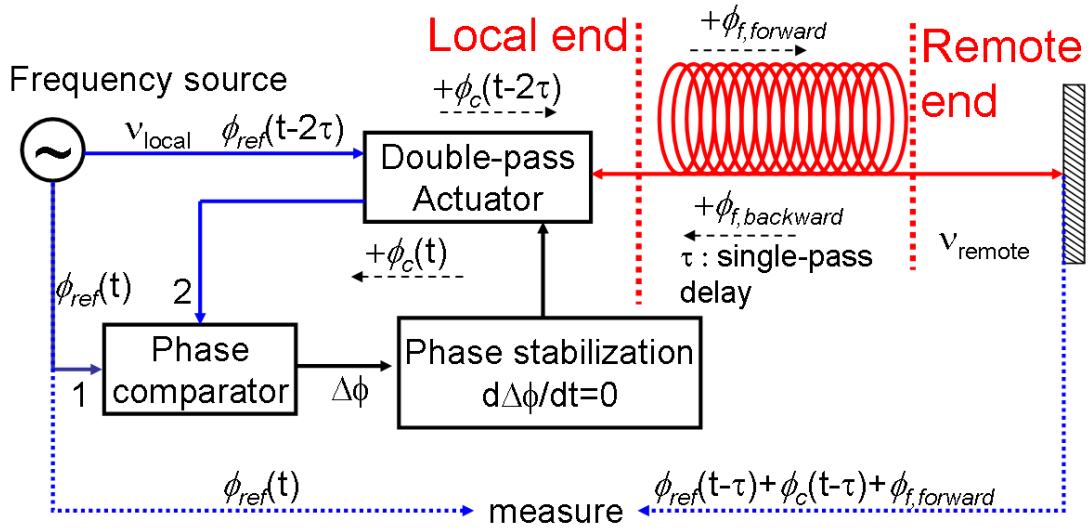


Figure 4.2: Scheme of a compensated fiber link (with time-domain notations).

Fig.4.2 shows the scheme of a compensated fiber link. It can be used to transfer the frequency of an RF/microwave amplitude modulation (AM) signal, a pulsed laser signal (i.e. optical comb) or an optical carrier. The actuator can be piezo-controlled fiber-stretchers and thermally controlled fiber spools. In the case of an optical carrier frequency transfer,

the actuator is usually an acousto-optic modulator (AOM). The effect of an AOM on the polarization states of the optical signal, which can lead to a PMD noise, is much weaker than that of a fiber-stretcher.

The link is modeled as an ideal link and a noise source, which produces a phase noise $\phi_f$. The frequency signal $\nu_{local}$ is fed into the fiber link after passing the phase actuator. In this part, we suppose that $\nu_{local}$ $[= d\phi_{ref}(t)/dt]$ is an ideal source independent of time. At the remote end the received frequency is

$$\nu_{remote} = \frac{d[\phi_{ref}(t-\tau) + \phi_c(t-\tau) + \phi_{f,forward}]}{dt} = \nu_{local} + \frac{d[\phi_c(t-\tau) + \phi_{f,forward}]}{dt}, \quad (4.1)$$

where $\phi_{ref}$ is the phase of the frequency reference source, $\phi_f$ is the phase noise of the link, $\phi_c$ is the compensation phase and $\tau$ is the delay time of the fiber link for a one-way transfer. By using a mirror or a circulator, a fraction of the optical signal is retro-reflected into the link at the remote end. This reflected signal arrives at the local end, and passes the phase actuator again. After that, a phase comparator compares the phase difference between this signal and the local signal, yielding the round-trip phase fluctuation

$$\Delta\phi = \phi_{ref}(t) - \phi_{ref}(t-2\tau) - \phi_c(t) - \phi_c(t-2\tau) - \phi_{f,forward} - \phi_{f,backward}. \quad (4.2)$$

Finally, $\Delta\phi$ is stabilized to be a constant value by controlling the phase with the actuator. Thus, we can obtain

$$\frac{d\phi_{ref}(t)}{dt} = \frac{d[\phi_{ref}(t-2\tau) + \phi_c(t) + \phi_c(t-2\tau) + \phi_{f,forward} + \phi_{f,backward}]}{dt}. \quad (4.3)$$

This noise cancellation is only effective for the low Fourier frequencies $f \ll 1/(4\tau)$, where

$$\begin{cases} \frac{d\phi_{f,forward}}{dt} \approx \frac{d\phi_{f,backward}}{dt} \\ \frac{d\phi_c(t)}{dt} \approx \frac{\phi_c(t-\tau)}{dt} \approx \frac{\phi_c(t-2\tau)}{dt} \end{cases}. \quad (4.4)$$

Eq.4.1, Eq.4.3 and Eq.4.4 give

$$\begin{cases} \frac{d[\phi_c(t-\tau)+\phi_{f,forward}]}{dt} \approx 0 \\ \nu_{remote} \approx \nu_{local} \end{cases}. \quad (4.5)$$

Thus, the link noise is compensated.

## 4.3 Operational requirements

### 4.3.1 Requirement of a robust phase-locked loop

As shown in the principle scheme (see Fig.4.2), the compensation system is a phase-locked loop (PLL). In fact, the main PLL contains a few PLLs acting as narrow bandwidth RF filters.

The rule of thumb for a PLL is that the phase jitter, $\phi_{rms}$ at the input of phase comparator, has to be much less than $1rad$, so as to prevent the PLL from loss of cycles or unlock. This jitter is dominated by the noise for Fourier frequencies higher than the loop control bandwidth, because it is an in-loop noise. Consequently, we can guarantee that the PLL is robust if $\phi_{rms}(f_l, f_h) \ll 1\ rad$ (see Appendix A), where $f_l$ is the control bandwidth and $f_h$ is the upper bound of the detection bandwidth.

For the main PLL, $f_l$ is less than $1/4\tau$, and the phase jitter of the link $\phi_{rms-opt}$ is usually more than $1rad$. In order to maintain the PLL operating properly for a long time, we have to divide the frequency (by a factor of $n$) of the link noise detection signal to reduce the in-loop phase jitter (i.e. $\phi_{rms} = \phi_{rms-opt}/n \ll 1$ `rad`).

### 4.3.2 Frequency shift at the remote end

The forward and backward propagation signals, for the round-trip noise determination, should have a frequency difference of $\Delta\nu_{shift}$.

The phase comparator (Fig.4.2) contains a photodiode which produces beat-notes of optical signals. In additional to the round-trip signal for link noise cancellation, a lot of stray reflected signals are also coupled into the photodiode. For a $100km$ optical link, even though there are no localized parasitic reflections, the Rayleigh backscattering leads to a stray reflected signal of $\sim 0.2\%$ of the incident power. This result is calculated, based on the parameters of 0.15 `dB/km` Rayleigh loss, $\sim 1/500$ (Hartog & Gold, 1984) coupling ratio in power from Rayleigh loss to the backward propagation mode and 0.2 `dB/km` propagation loss. Clearly, the effect of these stray reflections is not negligible if the round-trip signal is at the frequency of these signals. In order to avoid this effect, the frequency of the round-trip signal has to be shifted at the remote end. Thus, the round-trip signal is at a different frequency than these stray reflections. Consequently, the beat-note signal between the round-trip signal and the local reference signal can be selected by using an RF bandpass filter, while the beat-note signal related with stray reflections is filtered out, see Ma *et al.* (1994).

## 4.4 Fundamental and technical limitations

In this part, I discuss fundamental limitations and noise effects of the optical link.

### 4.4.1 Fundamental limitation due to the delay

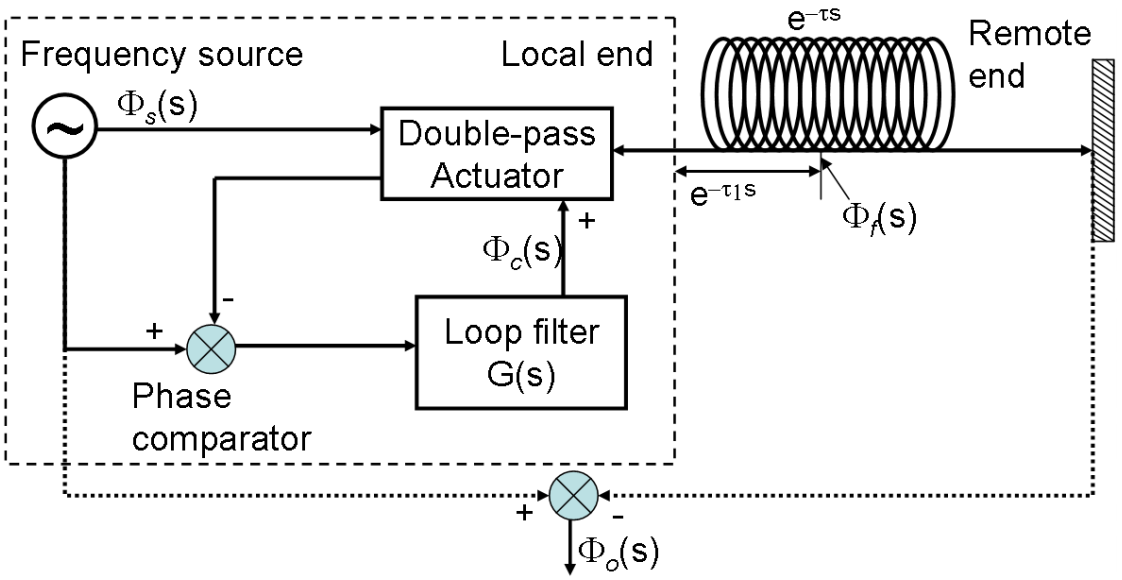


Figure 4.3: Scheme of an actively compensated fiber link (with Laplace-domain notations).

The compensated link has a limited control bandwidth and noise rejection ratio, because of the fiber delay, as first pointed out by Newbury *et al.* (2007); Williams *et al.* (2008). Fig.4.3 shows the link scheme with Laplace-domain notations. It gives

$$\begin{cases} \Phi_c(s) &= \{\Phi_s(s) - [\Phi_s(s) + \Phi_c(s)]e^{-2\tau s} - \Phi_c(s) \\ & \quad -\Phi_f(s)e^{-(2\tau-\tau_1)s} - \Phi_f(s)e^{-\tau_1 s}\}G(s) \\ \Phi_o(s) &= \Phi_s(s) - [\Phi_s(s) + \Phi_c(s)]e^{-\tau s} - \Phi_f(s)e^{-(\tau-\tau_1)s} \end{cases}, \tag{4.6}$$

where $\Phi_s(s)$ is the phase noise of the frequency source, $\Phi_f(s)$ is the phase noise of the link occurring at time $\tau_1$ from the local end, $\Phi_c(s)$ is the compensation phase, $\Phi_o(s)$ is the end-to-end beat-note (baseband), which corresponds to the phase noise of the link, $\tau$ is the laser propagation delay from the local end to the remote end, $G(s)$ is the transfer function of the loop filter. We assume that the source produces an ideal frequency signal, i.e. $\Phi_s(s) = 0$. According to Eq.4.6, the transfer function from fiber noise to the compensated link noise is

given by

$$\frac{\Phi_o(s)}{\Phi_f(s)} = -\frac{1+(1-e^{-2\tau_1 s})G(s)}{1+(1+e^{-2\tau s})G(s)}e^{\tau_1 s-\tau s}. \tag{4.7}$$

At low Fourier frequency ($f \ll 1/4\tau$), the frequency response magnitude of this transfer function decreases, while the gain of the loop filter increases. However, this magnitude can not be reduced arbitrarily, even if an infinite gain is applied by the loop filter. The minimum magnitude of the frequency response is

$$\begin{array}{rcl} \lim\limits_{|G(s)|\to+\infty}\left|\frac{\Phi_o(s)}{\Phi_f(s)}\right| & = & \left|\frac{1-e^{-2\tau_1 s}}{1+e^{-2\tau s}}\right| \\ & = & \left|\frac{\sin(2\pi\tau_1 f)}{\cos(2\pi\tau f)}\right| \\ & = & 2\pi\tau_1 f, \texttt{ for } f \ll \frac{1}{4\tau} \end{array}, \tag{4.8}$$

where $s = 2\pi j f$ is the Laplace variable, $f$ is the Fourier frequency. For low Fourier frequencies, the minimum residual phase noise is the free-running link noise scaled by $2\pi\tau_1 f$. However, a high control gain would significantly amplify the link noise around the frequency of $\sim \frac{1}{4\tau}$, according to Eq.4.8. In order to obtain a high link stability, a trade-off should be found between a lower feedback gain at the frequency of $\sim \frac{1}{4\tau}$ and a higher feedback gain for lower frequencies.

Assuming that the noise is uniformly distributed and uncorrelated over the link, the mean residual noise ratio in power would be not less than:

$$R_p(f) = \int_0^\tau \frac{(2\pi\tau_1 f)^2}{\tau} d\tau_1 = \frac{1}{3}(2\pi\tau f)^2, \texttt{ for } f \ll 1/(4\tau). \tag{4.9}$$

The link phase noise in amplitude is proportional to the square root of the link length $L$; while the noise rejection limit is inversely proportional to the link length. Consequently, the link residual phase noise (in amplitude) presents a $L^{3/2}$ law for low Fourier frequencies for uniformly distributed noises (Williams *et al.*, 2008).

### 4.4.2 Laser source noise effect

The phase noise of the laser source also affects the measured link performance. In order to evaluate this effect, we assume that the link is ideal (i.e. $\Phi_f(s) = 0$). According to Eq.4.6, the transfer function from the laser noise to the compensated link noise is given by

$$\frac{\Phi_o(s)}{\Phi_s(s)} = (1-e^{-\tau s})\frac{1+(1-e^{-\tau s})G(s)}{1+(1+e^{-2\tau s})G(s)}. \tag{4.10}$$

The first factor $(1 - e^{-\tau s})$ corresponds to the link noise detection system acting as a delayed self-heterodyne interferometer (DSHI). It contributes to the phase/frequency power noise with a factor of $4sin^2(\pi f \tau)$ (Okoshi *et al.*, 1980; Rubiola *et al.*, 2005).

The second factor is the contribution of the link compensation, which is unity for $G(s) = 0$ (i.e. no control). The magnitude of this factor is the same than the right side of Eq.4.7 with $\tau_1 = \tau/2$, corresponding to the link position at the middle. On the other hand, the mean residual ratio of the free-running link noise is comparable to the residual noise ratio at the middle position (see Eq.4.7 and Eq.4.9). Thus, ***the laser source frequency/phase noise effect is negligible if the $\tau$-time DSHI output of the laser noise is much less than the free-running link noise.***

### 4.4.3 Detection noise effect

For the optical carrier frequency transfer, the photodiode yields an heterodyne detected signal of about hundred `MHz`. At such a frequency, the detection noise is usually dominated by wide bandwidth noises: shot noise and Johnson noise.

Shot noise follows a Poisson distribution related to the photodiode current. Its phase noise power spectral density (PSD) is given by

$$\Phi^2_{shot} = \frac{h\nu(P_{opt1} + P_{opt2})}{\eta P_{opt1} P_{opt2}} \approx \frac{h\nu}{\eta P_{opt2}} \; rad^2/Hz \; \texttt{for} \; P_{opt1} \gg P_{opt2}. \tag{4.11}$$

where $\eta$ is the detector quantum efficiency, $h\nu$ is the photon energy, $P_{opt1}$ and $P_{opt2}$ are optical power of the reference and retro-reflected signals received by the phase comparator.

Johnson noise is due to thermal effect inside a resistor. The standard resistance of the RF system is 50 Ω, Thus, the phase noise PSD induced by Johnson noise can be approximately written as

$$\Phi^2_{johnson} = \left(\frac{h\nu}{e\eta}\right)^2 \frac{2k_B T}{50 P_{opt1} P_{opt2}} \quad [\texttt{rad}^2/\texttt{Hz}], \tag{4.12}$$

where $T$ is the temperature in Kelvin, $k_B$ is Boltzmann's constant.

According to Eq.4.11 and Eq.4.12, shot noise effect is equal to Johnson noise effect for $P_{opt1} = 1$ `mW`. The detected signal-to-noise ratio can not be efficiently improved by further increasing the power of $P_{opt1}(= 1$ `mW`$)$, because shot noise is independent of $P_{opt1}$. Consequently, the reference signal power should be about 1 `mW` or higher, in order to obtain a low noise detection.

For instance, both the local reference and link injected powers are 1 mW for a 200 km link. The round-trip signal will be in the range of $10^{-9}$ mW without any optical amplifier. The detected phase noise will be in the order of $10^{-7}$ $\mathrm{rad}^2/\mathrm{Hz}$. This phase noise corresponds to a phase jitter of $\sim 1$ rad for a few MHz detection bandwidth, which can lead to the main PLL loss of cycles or out of lock. This noise effect could be efficiently reduced by increasing the round-trip signal's power.

However, the input optical power of the link is limited by stimulated Brillouin scattering (SBS). The origin of SBS is a physical phenomenon called electrostriction. Electrostriction is a property of all electrical non-conductors, or dielectrics, that causes them to change their shape under the application of an electric field. Due to this effect, a high density laser beam stimulates acoustic vibrations and backscattered Stokes light in the fiber. The fiber refractive index is then modulated, forming a moving Bragg grating, which enhances the backscattering effect. Once the input laser density is over a threshold, the reflected power increases rapidly. The threshold is usually a few mW for the SMF-28 fiber, and depends on the fiber length. Note that the SBS signal frequency is downshifted about 11 GHz, far away from the frequency of detected signals. As a result, the SBS effect does not directly disturb the compensation system. It is negligible when the input optical power of the link is below the SBS threshold.

In order to get a low noise detection, optical amplifiers (see below) have to be used for a long distance link (e.g. $\sim 200$ km).

### 4.4.4 System noise floor

The link noise cancellation technique is based on the assumption that phase fluctuations are identical for forward and backward propagation directions. We have discussed the fundamental limitation due to the fiber delay, which is relevant to the time asymmetry with respect to noise detection and compensation for the two propagation directions. In addition to this limitation, there are a few limitations induced by the path, frequency and group delay asymmetries. These limitations may lead to a system noise floor of the fractional frequency instability higher than that caused by the fiber delay for long integration times.

#### 4.4.4.1 Non-common optical fibers

A few fibers in the system are not part of the main PLL (see blue lines in Fig.4.2). The noise occurring in these fibers, mainly induced by the temperature fluctuation, may determine the floor of the measurement system for long terms. The fiber (SMF-28) has a temperature

coefficient $C_T$ of $\sim 10^{-5}$ /K. Assuming that the temperature fluctuations of these fibers are homogenous, the frequency fractional instability due to this fluctuation will be

$$\sigma_y(\tau) \approx \frac{\Delta\tau}{\tau} = \frac{C_T \Delta T n l_a}{c\tau} \approx 5 \times 10^{-14} \frac{l_a \Delta T}{\tau}, \tag{4.13}$$

where $\Delta\tau$ is the delay time fluctuation of the compensated link, $l_a$ is the asymmetry length of fiber in meter, $\Delta T$ is the temperature fluctuation in Kelvin during time $\tau$. The asymmetry length is the length difference between the local reference arm and non-common part of round-trip arm at local end (blue and green lines in Fig.4.1).

In our laboratory, the temperature fluctuation is about 1 Kelvin peak-to-peak with a period of about 400 s, corresponding to an instability of a few $10^{-16}$ at 200 s integration time for 1 m length asymmetry (see Eq.4.13). In order to realize and measure an ultra-stable frequency transfer, it is essential to minimize and match the non-common fiber lengths and make a good thermal isolation for the optical system. The isolation also reduces effects induced by the acoustic noise and the air flow.

#### 4.4.4.2 Forward and backward frequency shift

The forward and backward propagation signals have a frequency difference of $\nu_{shift}$, in order to reduce stray reflection effect (70 MHz in our case). This frequency shift results in an imperfect phase noise compensation, because a delay change corresponds to different phase variations for the forward and backward signals.

Assuming the link noise induces an equal delay fluctuation $\Delta\tau$ for both forward and backward signals, the phase change of the backward propagation signal is

$$\begin{aligned} \Delta\phi_{back} &= \Delta\tau \times \nu_{back} \\ &= \Delta\tau \times \nu_{for}(1 + \tfrac{\nu_{shift}}{\nu_{for}}) \\ &\approx \Delta\phi_{for}(1 + 3.5 \times 10^{-7}) \end{aligned} \quad , \tag{4.14}$$

where $\Delta\phi_{for}$ and $\Delta\phi_{back}$ are phase variations, $\nu_{for}$ and $\nu_{back}$ are frequencies of the forward and backward propagation signals.

Since the noise correction system imposes $\phi_c = -\frac{\Delta\phi_{back}+\Delta\phi_{for}}{2}$, it leaves an uncorrected phase fluctuation: $\Delta\phi_{for} + \phi_c \approx 2 \times 10^{-7}\Delta\phi_{for}$. Thus, the instability of the compensated link is then

$$\sigma_y(\tau)_{link} \approx 2 \times 10^{-7} \sigma_y(\tau)_{free}, \tag{4.15}$$

where $\sigma_y(\tau)_{free}$ is the free-running link instability for an integration time of $\tau$. This effect limits the residual instability no less than $\sim 2 \times 10^{-7}$ of the free-running link instability

for a single span transfer. It can be reduced by decreasing $\nu_{RF}$ or with a digital frequency processing.

#### 4.4.4.3 Chromatic dispersion effect

The forward and backward frequency shift $\nu_{shift}$ also causes an imperfect phase noise compensation due to the chromatic dispersion of SMF-28 fiber, which is $\sim$ 17 $\mathtt{ps}/(\mathtt{nm} \cdot \mathtt{km})$ at 1542 $\mathtt{nm}$. The backward propagation delay fluctuation $\Delta\tau_{back}$ can be approximated as:

$$\begin{array}{rcl} \Delta\tau_{back} & = & \Delta\tau_{for}[1 + D(\lambda)\Delta\lambda c/n] \\ & \approx & \Delta\tau_{for}(1 - 2 \times 10^{-9}) \end{array} , \tag{4.16}$$

where $\Delta\tau_{for}$ is the forward propagation delay fluctuation, $\Delta\lambda$ is wavelength difference with respect to $\nu_{RF}$, $c$ is the speed of light, $n$ is the fiber index. Clearly, the chromatic dispersion effect is negligible by comparing 4.16 and 4.14.

#### 4.4.4.4 Polarization mode dispersion effect

The birefringence of SMF-28 fiber typically leads to a PMD of $\leq 0.1$ $\mathtt{ps}/\sqrt{\mathtt{km}}$, corresponding to $\leq 1$ $\mathtt{ps}$ for a $\sim 100$ $\mathtt{km}$ fiber link.

In the paper of Lopez *et al.* (2008), the PMD effect of an 86 $\mathtt{km}$ RF modulation frequency transfer leads to a fractional instability of $\sim 10^{-16}$ at $10^4$ $\mathtt{s}$ integration time. This instability, corresponding to the worst specified value of the PMD effect, is too high to transfer an ultra-stable signal. Fortunately, this effect can be averaged out by scrambling the polarization of the laser signal. Experimentally, the long-term instability is reduced by more than 1 order of magnitude with this approach (Lopez *et al.*, 2008, 2010a)

However, we have never observed the PMD fluctuation effect in the level of a few $10^{-15}/\tau$ up to $10^4$ $\mathtt{s}$ for $86 - 300$ $\mathtt{km}$ optical carrier frequency transfers. This is due to the fact that the actuator (an AOM) causes much less polarization variation of the optical signals than the fiber stretcher used for the RF modulation frequency transfer. On the other hand, the fiber is buried in the ground, and well fixed and isolated. Consequently, PMD fluctuations of the fiber link are slow, and its effect is negligible. Note that the wavelength-dependant PMD effect is also negligible, because the frequency of the laser source is ultra-stable.

## 4.5 Experimental setup

In this part, I introduce the setup of the first experiment and some considerations of the system design. This setup is partly modified in successive experiments.

### 4.5.1 Fiber link


Figure 4.4: The telecom link between SYRTE and LPL.

The fiber link consists of two parallel 43 km fibers, which connects two laboratories in Paris area (LNE-SYRTE at Observatory de Paris and LPL at University Paris 13) (see Fig.4.4). Both fibers are made of a few different sections of buried fibers, which are spliced together. We connect these two fibers to realize an 86 km urban link with both ends at the same place. The losses and length were measured with the optical time domain reflectometry method. Total losses are 20 dB for the 86 km link. This link has been used to transfer the microwave frequency (Daussy *et al.*, 2005; Grosche *et al.*, 2007; Lopez *et al.*, 2008, 2010a; Narbonneau *et al.*, 2006).

### 4.5.2 Optical system

Fig.4.5 shows the optical part of the 86 km fiber link experiment.

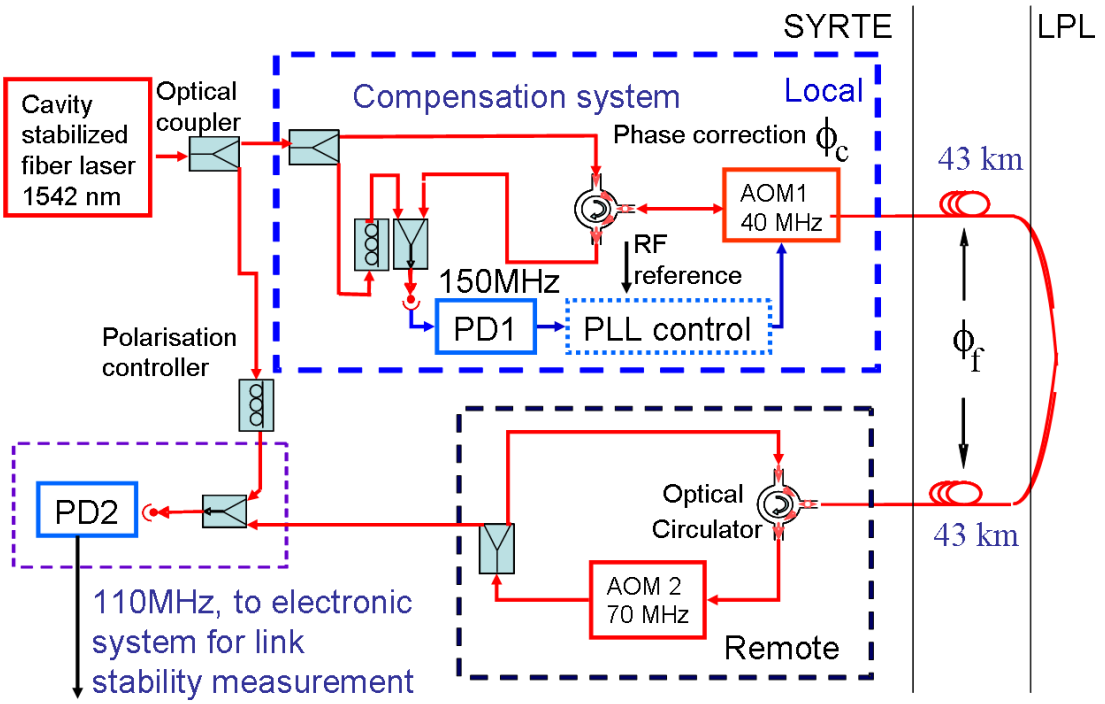


Figure 4.5: Scheme of the 86 km fiber link (AOM: acousto-optic modulator, PLL: phase locked loop, PD: photodiode).

The laser source is an ultra-stable cavity-stabilized laser. The laser light is split into three parts with two fiber couplers. Two of them are the reference signals for measuring the link stability and the phase noise of the round-trip signal. The third signal is injected into the fiber link through an optical circulator followed by an acousto-optic modulator (AOM1 with frequency $f_1 \approx 40$ MHz). To compensate the phase noise $\phi_f$ accumulated along the fiber, part of the signal at the remote end is reinjected into the link through another optical circulator after being frequency-shifted by AOM2 (with frequency $f_2 = 70$ MHz). This return signal, which passes twice through the link and experiences a phase noise $\sim 2\phi_f$, is mixed at the local end with the reference signal on photodiode PD1. The round-trip signal is shifted by the frequency $2f_1 + f_2$ from the local signal before arriving at PD1 (see Fig.4.5), which distinguishes it from the stray reflected light and makes the detection system immune to parasitic reflections. The output of PD1 at frequency $2f_1 + f_2$ carries the round-trip phase fluctuations. It is phase-locked to a synthesized RF signal by using a voltage-controlled oscillator to control the phase of AOM1.

The PLL applies the correction $\phi_c(f)(\approx -\phi_f(f))$ to the AOM1 frequency $f_1$ for low Fourier frequencies ($\ll 1/4\tau$).

The reference optical power at the input of the polarization controllers is $\sim 1$ mW; the link input power is $\sim 1$ mW; the insertion loss of AOMs is $\sim 3$ dB; the insert loss of the circulators is $\sim 2$ dB; the coupling ratios to the photodiode are 10% of the reference signal and 90% of the round-trip signal in power.

We measure the optical frequency instability by analyzing the beat-note at frequency $f_1 + f_2$ provided by mixing the single-trip and reference signals on photodiode PD2. Two polarization controllers are employed for optimizing the beat-note signal amplitudes.

The optical system is entirely composed of commercial off-the-shelf pigtailed telecommunications components. The unmatched fiber length of the optical system is less than 20 cm. In order to further reduce the system noise floor, this system is enclosed in a $\sim 60$ cm $\times 80$ cm $\times 30$ cm space with thick aluminum plates, Mylar, bubble wrap and aluminum foils.

### 4.5.3 Electronic system

Fig.4.6 shows the scheme of the electronic system with following components and functions:

- A 150 MHz narrow bandpass filter ($\sim 5$ MHz) is used for filtering out not only the signals related with stray reflections (e.g. at 80 MHz) of the link but also the wide bandwidth detection noise. The bandwidth of the 110 MHz bandpass filter is not very critical (it is a few tens of MHz), because the received optical power is much higher and thus the detection noise is negligible.

- A logarithmic amplifier is one whose output voltage $V_{out}$ is $K$ times the natural logarithm of the input voltage $V_{in}$. This can be expressed as

$$V_{out} = K \log(\frac{V_{in}}{V_{ref}}), \tag{4.17}$$

  where $V_{ref}$ is the normalization constant in voltages and $K$ is the scale factor in voltage. By controlling the $V_{ref}$ to be proportional to $V_{in}$, $V_{out}$ can be stabilized to be constant, even though the input power $P_{in} = \langle V_{in}^2 \rangle / 50\Omega$ fluctuates by a few tens of dB. The logarithmic amplifiers are used to stabilize the detected RF powers, allowing the gain of the control system to be insensitive to the amplitude variations at photodiodes'

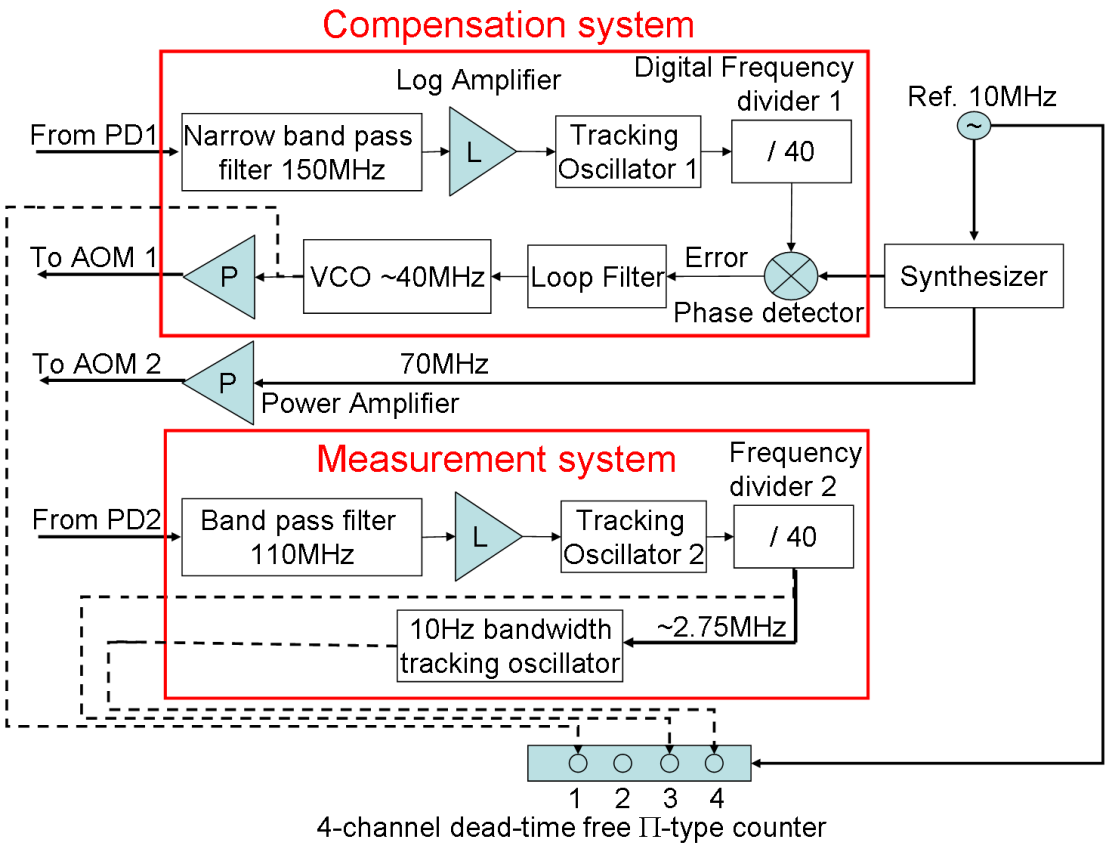


Figure 4.6: Scheme of the electronic system and instability measurement, L: RF logarithmic amplifier, P: RF power amplifier, PD: photodiode.

output. These variations are mainly due to the polarization fluctuations of optical signals.

- A tracking oscillators is a low noise oscillator whose phase is locked to an input signal in a control bandwidth. For Fourier frequencies below the control bandwidth, its output follows the phase fluctuation of the input signal. For Fourier frequencies higher than the control bandwidth, it exhibits its own phase noise. Here, the tracking oscillators are used as ultra-narrow bandwidth RF filters. The control bandwidths of tracking oscillator 1 and 2 are $\sim$ 100 kHz, which is a trade-off between reducing the broadband detection noise and capturing the link noise. The third tracking oscillator, having a 10 Hz control bandwidth, is used for filtering out the high frequency link noise. Note

that we have to verify if these PLLs are robust, i.e. $\phi_{rms}(f_l, f_h) \ll 1$ rad. In order to obtain a measurement noise floor of $\leq 10^{-16}/\tau$, the instability of the third tracking oscillator should be about or below $10^{-10}$ at 1 s. We develop a home-made tracking oscillator as shown in Fig.4.7. The 100 MHz oscillator is a commercial OCXO (oven controlled crystal oscillator) with a typical instability of $\leq 10^{-11}$ at 1 s. Although the 2.75 MHz signal in Fig.4.6 is mixed up to 5 MHz, which almost doubles the requirement of the oscillator's stability, this oscillator is still good enough for this application. The loop filter gives a proportional gain of $\sim$ 10 Hz bandwidth and an integral gain for frequencies below $\sim$ 2 Hz.

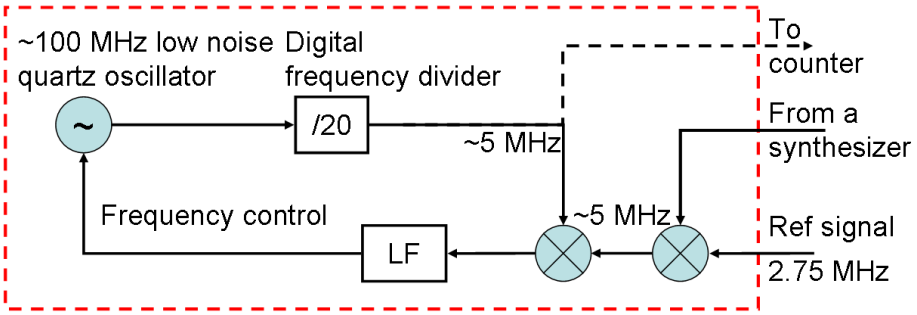


Figure 4.7: Scheme of the 10 Hz bandwidth tracking oscillator, where LF is the loop filter.

- The digital frequency dividers are suitable for the RF signal in the range of 100 MHz – 1 GHz. They are used to enlarge the compensation control dynamic and hence improve the robustness of the main PLL. This is essential for the long distance optical carrier frequency transfer. In these experiments, the residual phase jitter of the round-trip signal is usually comparable to or higher than 1 rad. Especially in real telecom link, noise due to human activities is not stationary, and can be several times higher than the average level. The dividing ratio, dependent on the link noise and length, should be higher for longer or noisier links.

- The phase detectors are RF double-balanced mixers.

- The loop filter (LP) is a simple proportional-integral amplifier. The transfer function $G(s)$ of the LP and the VCO can be written as $(K_1 + K_2/s)/s$, where $K_1$ and $K_2$ are proportional and integral gains.

- The frequency counter (K+K GmbH) is a high resolution dead-time free Π-type counter, which is equivalent to a phase recorder. The range of input frequency is from hundreds kHz to $\sim 64$ MHz, and the measurement error for a 10 MHz signal is lower than $0.02\pi$ rad for integration time from 1 s to $10^4$ s. We use three channels simultaneously to record the frequency of the compensation signal, full bandwidth and 10 Hz bandwidth end-to-end beat-note.

- The shift frequency of AOM2, the RF reference of the frequency counter and link noise demodulation signal are synthesized from a 10 MHz common signal reference.

This design is highly robust, allowing a long time locking. According to Eq.4.11, Eq.4.12 and the parameters of the optical system, the effects of shot noise and Johnson noise on the end-to-end beat-note are estimated to be a few $10^{-11}$ $\text{rad}^2/\text{Hz}$ and a few $10^{-10}$ $\text{rad}^2/\text{Hz}$ respectively. The detection noise effect, accumulated over the detection bandwidth of a few MHz, is much less than 1 rad. Thus, the tracking oscillator for the link noise compensation (150 MHz) can work properly.

## 4.6 Experimental results of a dedicated link

In this section, I show the experimental results of the 86 km urban dedicated link.

### 4.6.1 The 86 km link

Fig.4.8 shows the phase noise PSD of the 86 km free-running and compensated link.

The phase noise of the free-running link is obtained by using the end-to-end beat-note after the tracking oscillator and a frequency-division by 40. It is connected to the counter channel #3 (see Fig.4.6). Alternatively, we down-convert this signal to the baseband by mixing it with a 2.75 MHz signal produced by a synthesizer. The phase variation of this signal is much less than $\pi/2$ during a phase noise measurement. The phase noise is measured by analyzing the baseband signal with a fast Fourier transformer (FFT). In this measurement, AOM1 is driven by a stable 40 MHz signal provided by the synthesizer instead of the VCO output.

The contribution of the laser source noise (see Fig4.8) on the 86 km free-running link measurement is calculated according to Eq.4.10 and the measured laser phase noise (see

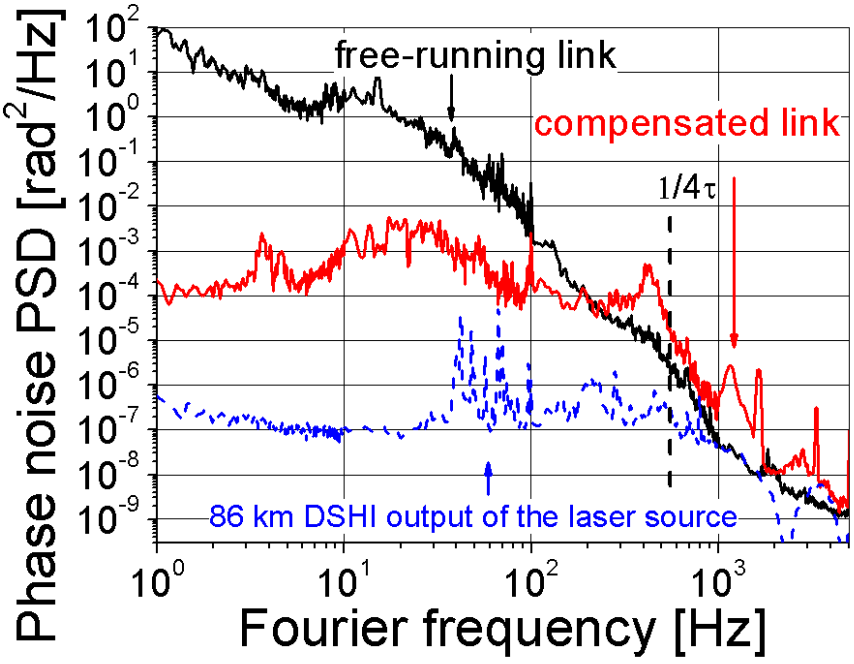


Figure 4.8: Phase noise PSD of the 86 km free-running and compensated links and the laser source noise contribution to the 86 km free-running link measurement.

previous chapter). This contribution is much lower than the measured phase noise of the free-running link for Fourier frequencies lower than $\sim$ 1 kHz, and thus for Fourier frequencies below $1/4\tau$ ($\sim$ 580 Hz). The effect of the laser source's phase noise is negligible on the measurement for these Fourier frequencies (see previous section). For higher Fourier frequencies, this effect is also negligible, according to the integrated phase noise of the compensated link shown in Fig.4.9. Clearly, most of the noise energy of the compensated link is in the bandwidth from 20 Hz to $\sim$ 500 Hz, because of the free-running link noise distribution and the noise rejection limitation due to propagation delay. The phase jitter is about $\sqrt{0.16} = 0.4$ rad for Fourier frequencies higher than 1 Hz. It means that the optical signal transmitted over the 86 km urban link is still coherent to the local signal. Note that the loop filter has been optimized to minimize the phase jitter $\phi_{rms}(1\ \text{Hz}, 100\ \text{kHz})$ of the link.

Fig.4.10 shows the fiber noise compensation response of the link with the ratio of the phase

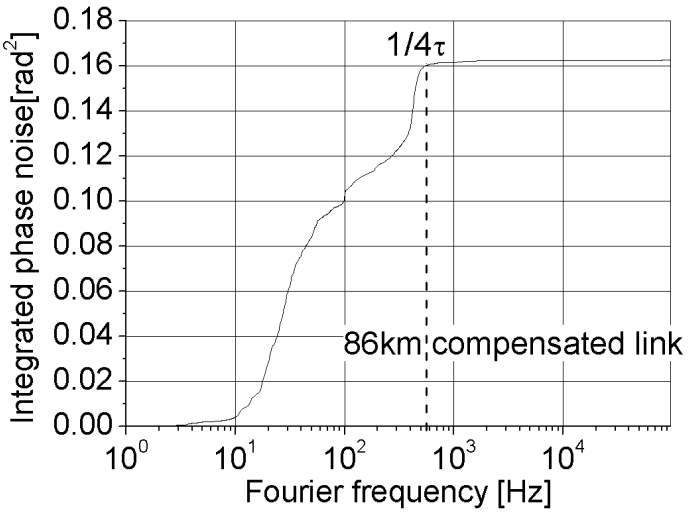


Figure 4.9: Integrated phase noise of the 86 km compensated link.

noise PSD of the compensated link to the free-running link. By fitting the experimental result with Eq.4.7, we determine that the loop filter has a proportional gain of $1/\tau$ ($\sim$ 2300 Hz) and an integral gain of $\sim 50Hz$ [i.e. G(s)=(2300+50/s)/s][1]. This response exhibits three sections: the proportional gain limited span between $\sim$ 20 Hz to $\sim$ 220 Hz, the integral gain limited span between a few Hz to $\sim$ 20 Hz and the delay limited range below a few Hz.

As shown in Fig.4.6, a dead-time free Π-type counter simultaneously samples the frequency of the VCO output (i.e. the free-running link, channel #1), the full bandwidth end-to-end beat-note ($\sim$ 100 kHz limited by the tracking oscillator2, channel #3), and the $\sim$ 10 Hz bandwidth end-to-end beat-note (channel #4). Overlapping Allan deviation of these signals are then calculated and shown in Fig4.11. With a 10 Hz measurement bandwidth, the link instability is $\sim 1.5\times10^{-16}$ at 1 s, $2\times10^{-18}$ at 100 s and a few $10^{-19}$ at $10^4$ s. It is limited by the system noise floor for integration time longer than 100 s. The instability decreases as $1/\tau$ for short times, which is consistent with the fact that the transferred signal is dominated by high frequency noise, because a first-order filter does not suppressed the noise at higher frequency sufficiently. Note that the air conditioning degrades the instability at $\sim$ 200 s, and this system noise floor can be reduced by better length-balancing and isolating the optical

[1]The outer 1/s indicates the VCO.

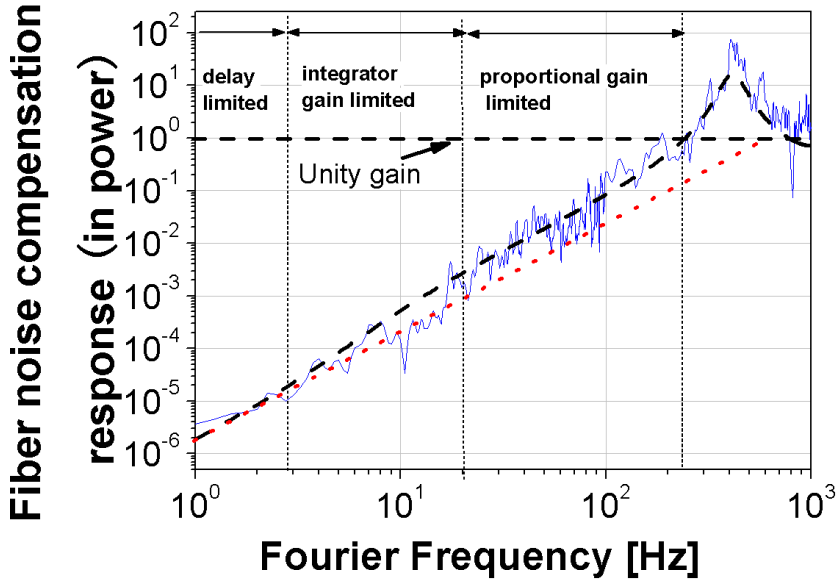


Figure 4.10: phase noise PSD ratio of the compensated link to the free-running link: the measured result (blue trace), the simulated result (black dashed line) and the limitation due to fiber delay (red dotted line).

system.

Regarding the ultra-stable frequency dissemination, the transferred signal can be tracked with a local ultra-stable laser source, whose phase is locked to the incoming signal with a low control bandwidth (e.g. 10 Hz), in order to filter out the high frequency link noise in the optical domain. For instance, we use our ultra-stable laser source as this tracking oscillator at the remote end of the 86 km link, and assume that an ideal PLL control with 10 Hz bandwidth for the tracking is done. Thus, the output of the tracking laser will exhibit the phase noise of the link at frequencies lower than 10 Hz and of its own for frequencies higher than 10 Hz (see solid lines in Fig.4.12). The phase jitter of this optical oscillator, with respected to the ultra-stable transferred signal, is less than 0.02 $\mathrm{rad}^2$, corresponding to $\sim 0.1$ rad phase jitter and a fractional frequency instability of $\sigma_y(\tau) =\sim 10^{-16}/\tau$. The optimum control bandwidth of the tracking oscillator depends on the noise level of the link and the optical oscillator. It is worth noting that the noise of the transferred signal for high frequencies is also filtered out

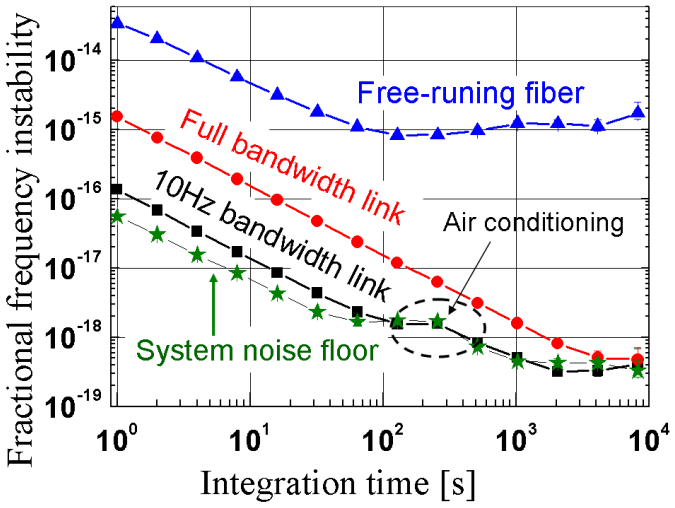


Figure 4.11: Overlapping Allan deviation of the 86 km free-running fiber, the 86km full bandwidth link, the 86 km 10 Hz bandwidth link and the measurement noise floor (i.e. 0 km link).

by the tracking oscillator. However, we are usually more interested in the long-term stability, which is not sensitive to the high frequency noise.

### 4.6.2 A 2 X 86 km link

Grosche *et al.* (2007); Newbury *et al.* (2007); Williams *et al.* (2008) have reported the performance of longer links extended by adding spooled fiber to urban links. To implement a longer link with a more realistic setup, in 2008 we devised a scheme to pass twice through the 86 km link, leading to a $2 \times 86$ km full urban link.

#### 4.6.2.1 Experimental setup

Fig.4.13 displays the scheme of the $2 \times 86$ km link. The signal passes twice through the 86 km link, with AOM shifters to mark the paths of the signals, and erbium-doped fiber amplifiers (EDFA) to amplify the optical signal.

The round-trip optical losses of the passive $2 \times 86$ km link is about 80 dB. Considering the other extra losses (e.g. due to AOMs), the detection quantum noise is $\sim 10^{-7}$ $\mathrm{rad}^2/\mathrm{Hz}$

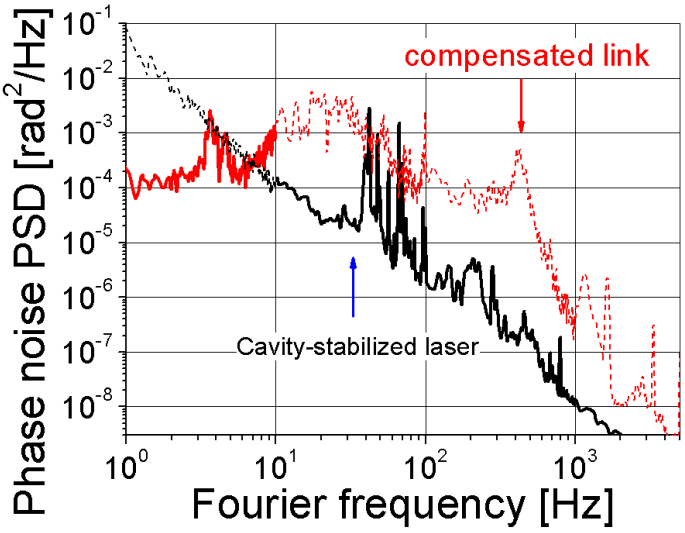


Figure 4.12: Phase noise PSD of the 86 km compensated link (red) and the ultra-stable laser stabilized to a free-running reference cavity (black).

according to Eq.4.11 and Eq.4.12. The detected phase jitter of the tracking oscillator 1 (out of the control bandwidth, i.e. $> 100$ kHz) is $\sim 1$ rad after passing through the 5 MHz bandpass filter. Such a phase jitter can lead to an unlock of tracking oscillator 1 (see Fig.4.6). In order to realize a stable operation, we have to improve the signal-to-noise ratio by amplifying the optical signal with EDFA.

At that time, we had only unidirectional EDFAs, which are not suitable to be thermally isolated because of their high power consumption. When the EDFAs are used as out-of-loop components, it significantly degrades the link performance. Consequently, we had to cancel the noise of EDFAs in addition to the noise of the link with a scheme shown in Fig.4.13.

The optical signal is fed into the 86 km link through an optical coupler. At the other end of the 86 km link, the signal is reflected by a "frequency shift mirror", which consists of an optical circulator, an erbium-doped fiber amplifier (EDFA1) and an AOM (AOM2). The mirror-reflected signal is partly coupled to the remote end after passing through the 86 km fiber again. The return signal inversely passes through the same path from the remote end to the local end. EDFA1 with a $\sim 11$ dB gain is implemented to compensate the extra losses due to the recirculation. The losses are 6 dB for double-pass through the combiner (C on

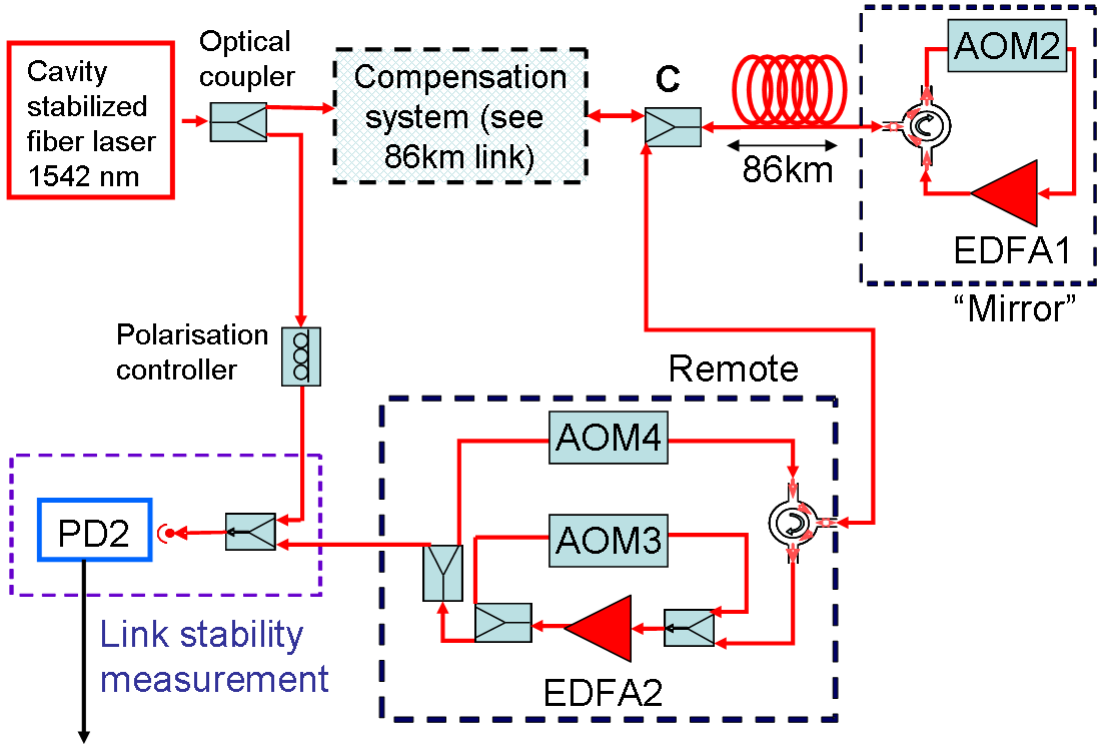


Figure 4.13: Scheme of $2 \times 86$ km link, EDFA: erbium-doped fiber amplifier, AOM: acousto-optic modulator, PD: photodiode.

Fig.4.13), 3 dB for the optical circulator of the "mirror" and 2 dB for AOM2. Thus, this link is equivalent to a 172 km span link without any intermediate optical amplifier.

At the remote end, another optical amplifier (EDFA2 with about 20 dB gain) was added to amplify the return signal. In order to compensate the EDFAs' noise, the round-trip signal should pass the EDFAs twice, while the link transferred signal (the link output at the remote end) passes these EDFAs once. This is naturally the case for EDFA1 but not for EDFA2. To compensate contribution of EDFA2's noise, we add a recirculation loop at the remote end. AOM3 is inserted in this loop to identify the single-pass and double-pass signals. The round-trip signal is transmitted successively through the circulator, EDFA2, AOM3, EDFA2, AOM4 and the circulator, while the link-transmitted signal passes sequentially through the circulator and EDFA2 to the output (i.e. the measured signal shown in Fig.4.13).

We introduce the following notations: $f_1(= 40$ MHz) is the frequency shift of AOM1, $f_2(= 70$ MHz) is the frequency shift of AOM2, $f_3(= -65$ MHz) is the frequency shift of AOM3

and $f_4(= 95$ MHz) is the frequency shift of AOM4. The round-trip beat-note signal detected on PD1 has a frequency of $2f_1 + 2f_2 + f_3 + f_4 = 250$ MHz, while the end-to-end beat-note signal on PD2 at $f_1 + f_2 = 110$ MHz is used to measure the link stability. This setup can be simplified by using bidirectional EDFAs.

#### 4.6.2.2 Stability of the link

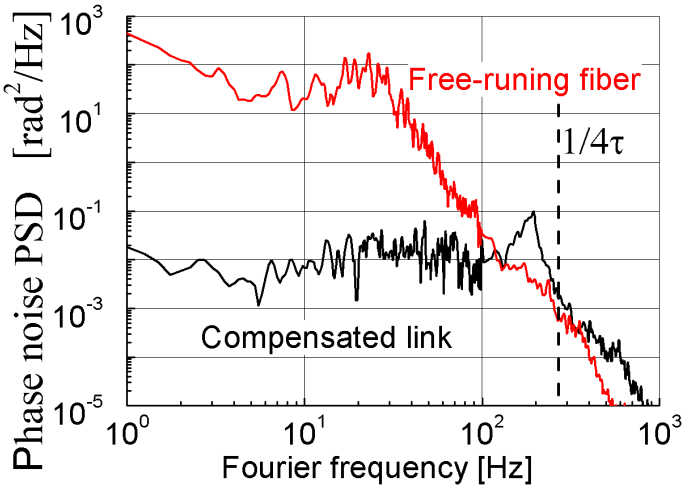


Figure 4.14: Phase noise of the $2 \times 86$ km free-running and compensated link.

Fig.4.14 displays the $2 \times 86$ km link's phase noise PSD with and without compensation. As expected, the correction bandwidth is about half of the one obtained for the 86 km link due to the link delay (see Fig.4.8). The integrated phase jitters from 1 Hz to 1 kHz are about 2.4 rad and 53 rad (rms) with and without compensation respectively.

Fig.4.15 shows the fractional frequency instability of the $2 \times 86$ km link. The Allan deviation is about $4 \times 10^{-16}$ at 1 s and in the range of $10^{-19}$ at $10^4$ s with a 10 Hz measurement bandwidth. The system noise floor is measured by replacing the urban fiber with an equivalent optical attenuator. This result is mainly limited by the thermal effect of the optical system's non-common paths.

In addition, we have used a $\Lambda$-type counter without the 10 Hz filter to highlight the counter effect (see Appendix A) and enable a comparison with the results of Newbury *et al.* (2007);

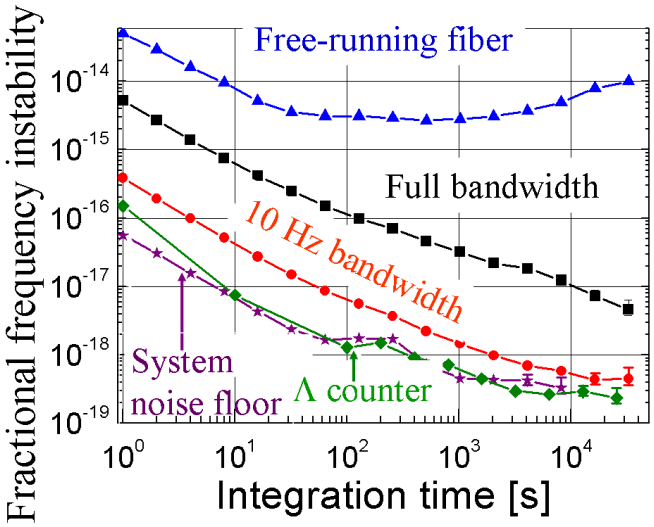


Figure 4.15: Fractional frequency instability of the free-running link (triangles), compensated $2 \times 86$ km link with 10 Hz measurement bandwidth (circles) and full measurement bandwidth ($\sim 100$ kHz) link sampled with Π-type counter (squares) and Λ-type counter (stars), diamonds indicate the system noise floor (i.e. 0 km link).

Williams *et al.* (2008) obtained with a 251 km link composed of 76 km urban fiber, 175 km spooled fiber and four inline EDFAs. The Allan deviations obtained with the Λ-type counter are shown by the star points in Fig.4.15. These deviations are lower than those obtained with a Π-type counter, owing to an additional filtering of the Λ-type counter. In order to avoid the dead-time effect, the deviations at 1 s, 10 s and 100 s are calculated from the frequency samples obtained with the corresponding gate-times at 1 s, 10 s and 100 s respectively. For longer integration times (i.e. $>$ 100 s), the deviation is calculated with frequency samples with a 100 s gate-time. Indeed, even through the Allan deviation is used, the Λ-type counter has already filtered out part of noises for Fourier frequencies higher than 0.01 Hz. It leads to a reduction factor of 2/3 on the Allan deviation for integration time above 100 s. Results are found similar to the data presented in Newbury *et al.* (2007), and in agreement with a $1/\tau^{3/2}$ slope for short term ($\tau \leq 10$ s). For integration time longer than 10 s, this deviation is roughly equal to the system noise floor which is dominated by the noise at low Fourier frequencies ($< 0.1$ Hz). It is consistent with the fact that the Λ-type counter has an additional

low-pass filter than the Π-type counter (Dawkins *et al.*, 2007).

#### 4.6.2.3 Discussion and scaling rules

Comparison between our results of the $2 \times 86$ km link and 251 km link Newbury *et al.* (2007) is not straightforward. First of all, the noise levels of the free-running links are different, because the 251 km link included 175 km fiber spools which are less noisy.

Furthermore, when the length of the fiber is virtually doubled by the recirculation technique, the phase noise PSD of the free-running link is twice that of a single-pass double-length fiber, as detailed below.

Under the assumption that the fiber phase noise is uniformly distributed and uncorrelated, the phase noise PSD is proportional to the length of the fiber, i.e. $S_\phi(L) \propto L$. However, with the recirculation technique the laser wave experiences twice the phase fluctuation $\delta\phi$ at each point of the fiber. Both contributions occurring at the same point are correlated [i.e. $\delta\phi_{first-pass} = \delta\phi_{second-pass}$] for noises, whose frequency is much lower than $1/4\tau$. Consequently, for these Fourier frequencies ($\ll 1/4\tau$), the phase noise PSD of a $2L$ length link realized by recirculation is expected to be four times that of a $L$ length fiber, because the phase noise PSD is proportional to $\delta\phi^2$ and $\delta\phi_{2L-link} = \int_0^{2L} \delta\phi dl = 2\int_0^{L} \delta\phi dl = 2\delta\phi_{L-link}$. The phase noise PSD for the recirculated link is twice of the one expected for a real 172 km link. Consequently, the stability results obtained for the recirculated link should be considered as an upper bound for a real link of the same length.

### 4.6.3 Improved experimental setup

We modified the optical system after the previous experiments with the 86 km dedicated fiber, in order to improve the robustness and reduce the system noise floor.

Fig.4.16 shows the scheme of the improved optical setup. We use an optical coupler and two Faraday mirrors (FM) to realize the round-trip noise detection instead of the previous configuration based on optical circulators. The FM rotator rotates the polarization of the laser signal by 45° for single pass. These FMs guarantee that the polarization states of backward reflected laser are orthogonal to the input states (Kersey *et al.*, 1991; Pistoni & Martinelli, 1991). As a result, the two combined FM-reflected waves at PD1's input always have the same polarization states, leading to a maximum beat-note amplitude without requiring any polarization controller. AOM2 is inserted before the FM at the remote end, and shifts the optical signal twice. Since it is driven with $f_2 = 35$ MHz instead of the previous value of

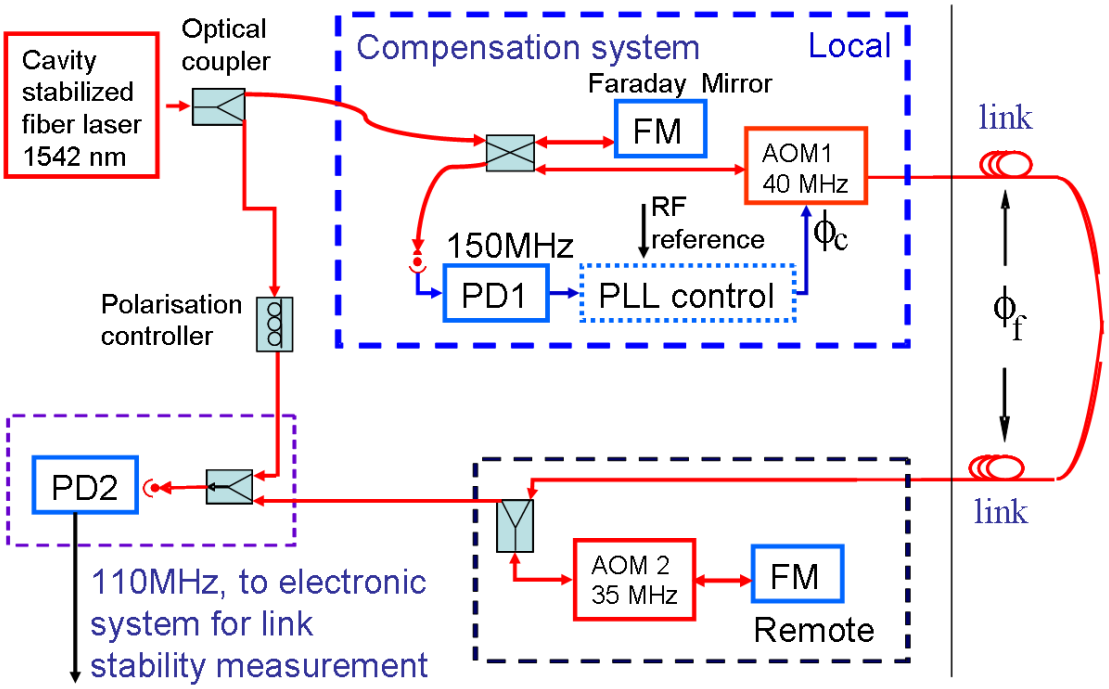


Figure 4.16: Optical part scheme of improved experimental setup (AOM: acousto-optic modulator, PLL: phase locked loop, PD: photodiode, FM: Faraday Mirror - 45° for single pass , where PLL control belongs to the electronic part.

70 MHz, the link noise detection signal and the measurement signal maintain their previous frequencies. Thus, we can keep using the previous electronic system, except for providing a 35 MHz signal rather than a 70 MHz signal to drive AOM2.

There are two benefits with such a configuration:

- The polarization states are automatic aligned, making the system more robust.
- It reduces the number of optical components and shortens the system optical path compared with the previous configuration (see Fig.4.5), corresponding to a lower system noise floor (Grosche *et al.*, 2009).

Fig.4.17 shows the system noise floor of the improved system, which is lower than that of the previous setup for integration times longer than 100 s.

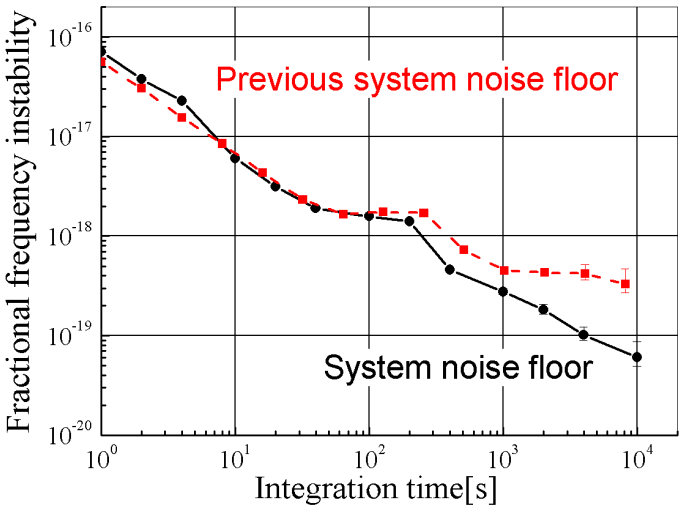


Figure 4.17: System noise floors of the improved optical system and the previous one.

## 4.7 Towards longer links

We have shown the performance of $100 - 200$ km optical link, which is comparable to reports from other research groups (Hong *et al.*, 2009; Musha *et al.*, 2008; Newbury *et al.*, 2007; Terra *et al.*, 2009; Williams *et al.*, 2008). However, the frequency comparison between metrology laboratories usually requires longer links. For example, the distance between Physikalisch-Technische Bundesanstalt (PTB) in Germany and LNE-SYRTE is about 1000 km. This section addresses a new configuration of optical link for longer distance frequency transfers.

### 4.7.1 How to extend the link to the continental scale?

There are a few limitations to the extension of the link. This part discusses requirements of the link performance, operation and availability for a continental scale link.

A longer link exhibits a higher free-running phase noise, whereas the control bandwidth and ratio of the noise correction are fundamentally limited by the propagation delay. The residual noise is proportional to $L^{3/2}$ for low Fourier frequencies, where $L$ is the link length. In practice, the link fractional stability, determined by the accumulated link noise, may be even worse than $L^{3/2}$ for longer links, because fiber noise is not homogenously distributed

and its spectrum is not follows a specific law. If a better link performance is required, it is necessary to divide the long link into a series of cascaded shorter links.

The other critical limitation of long optical link is the transfer attenuation, which limits the round-trip signal amplitude. It can not be compensated by a higher input power due to the SBS effect. This degrades the link noise detection, and could result in the unlock or loss of cycles of tracking oscillator 1, which is the front end of the detection system. The phase jitter of tracking oscillator 1 induced by the wide bandwidth detection noise should be kept much lower than 1 `rad`. This jitter is proportional to the square root of the detection bandwidth, where the bandwidth (a few `MHz`) is limited by the bandpass filter following PD1. The detection bandwidth should be large enough to detect most of the link noise (usually a few hundred `kHz`) for link noise evaluation and cancellation. By reducing the detection bandwidth, the detected signal-to-noise ratio can be improved by only $\sim$ 10 `dB`, corresponding to the loss of a 50 `km` fiber. Optical amplifiers could be used at detection, but they usually exhibit a high amplified spontaneous emission (ASE) noise when the signal is weak (e.g. nW for a 300 `km` link without any intermediate amplifier). Thus, the signals need to be amplified by adding in-line amplifiers for optical links longer than a few hundred kilometer or a shorter link with large attenuation (e.g. 50 `dB`).

A research group in Germany is developing a 900 `km` link, which connects PTB and MPQ1 (Predehl *et al.*, 2009). They have transferred the ultra-stable optical signal over a 480 `km` link with an fractional frequency instability of $2 \times 10^{-14}$ at 1 `s` integration time and $2 \times 10^{-18}$ at $10^4$ `s` (Terra *et al.*, 2010). This link is composed of a single segment and two in-line fiber Brillouin amplification (FBA) optical amplifiers. These amplifiers exhibit higher gain and lower noise than the EDFA, although it requires a pump power of up to 30 `mW` and an accurate frequency control on the pump.

However, it is quite difficult to obtain such a long dedicated fiber networks, since dedicated fibers are usually not for free. On the other hand, telecommunication networks have been established all over the world. Then, if we can use these existing networks, frequency transfer could be achieved between any remote laboratories. In that case, we have to share the fiber network with the telecommunication operator and adopt the well-known approach of wavelength division multiplexing. Our signal should propagate simultaneously with the optical carriers on which the digital data stream of Internet traffic are encoded, but on a different frequency channel, as explained in details below. With this new approach of a multiplexed link, we have to face a higher phase noise than with a dedicated link, due to the

multiple connectors and human activities in some parts of the public telecommunication networks. Consequently, we have to split the link into a few segments, in order to improve the link performance. The segments' length depends of the segments noise level, and is typically around $100 - 300$ km.

### 4.7.2 Extension with multiplexed networks

Using the public network is a very attractive idea, but the ultra-stable signal has to be transferred simultaneously with the other optical carriers, on which the digital data stream of Internet traffic are encoded. Fortunately, we can take advantage of the existing dense wavelength division multiplexing (DWDM) technique.

In fiber-optic communications, wavelength-division multiplexing (WDM) is a technology which multiplexes the optical signals on a single fiber by using different wavelengths/frequencies of laser carrier. This enables a multiplication of transferring capacity. WDM refers originally to optical signals multiplexed within the 1550 nm band, in order to efficiently make use of the working span of erbium doped fiber amplifiers (EDFAs), which is approximately $1525 - 1565$ nm (C band) or $1570 - 1610$ nm (L band). It is the most popular technique for optic communications nowadays. The international telecommunication union (ITU) has defined the ITU grid channels of DWDM networks to be 100 GHz/channel from 190.1 THz to 197.3 THz. New techniques allow a wavelength-division of 25 GHz/channel.

DWDM optical transmitters are set to a specific frequency and multiplexed together onto a fiber. The signal in each channel has to be de-multiplexed from signals in the fiber, because the optical detector cannot distinguish one frequency from another. The device, used to accomplished the multiplexing/de-multiplexing, is an optical add/drop multiplexer (OADM - a kind of frequency dependent directional coupler).

French national telecommunication network for technology, education and research (RENATER) is a DWDM public network. We applied for a dedicated channel (ITU #44) of a few segments of RENATER to extend our link. The used OADM is a three-port commercial component, which can insert or extract the signal in ITU #44 from the networks with isolation better than 25 dB for the adjacent channels ($\Delta\nu = 100$ GHz) and better than 40 dB for other channels. The losses are about 1.2 dB for the add-drop channel and below 1 dB for other channels.

Our ultra-stable signal is thus transmitted on a specific channel of the RENATER network. Such a propagation on a telecom network induces some constraints and difficulties on

the optical link scheme. First of all, the telecommunication network is designed to unidirectionally propagate signals, which enables to relax constraints on stray reflections and avoid any parasitic lasing effects in EDFAs; whereas the optical link requires bidirectional propagation. Furthermore, standard telecommunication networks often have conversions between optical signal and electrical signal in nodes, whereas the optical frequency dissemination has to be purely optical from the local end to the remote end. Therefore, OADMs have to be installed to bypass most RENATER's equipments at each node. Finally, all the equipment will be installed in the telecom networks stations. Thus, they have to operate without any laboratory facility.

### 4.7.3 A 108 km optical link with 22 km public networks

This experiment is to test the optical frequency transfer via public fiber networks.

#### 4.7.3.1 Link configuration

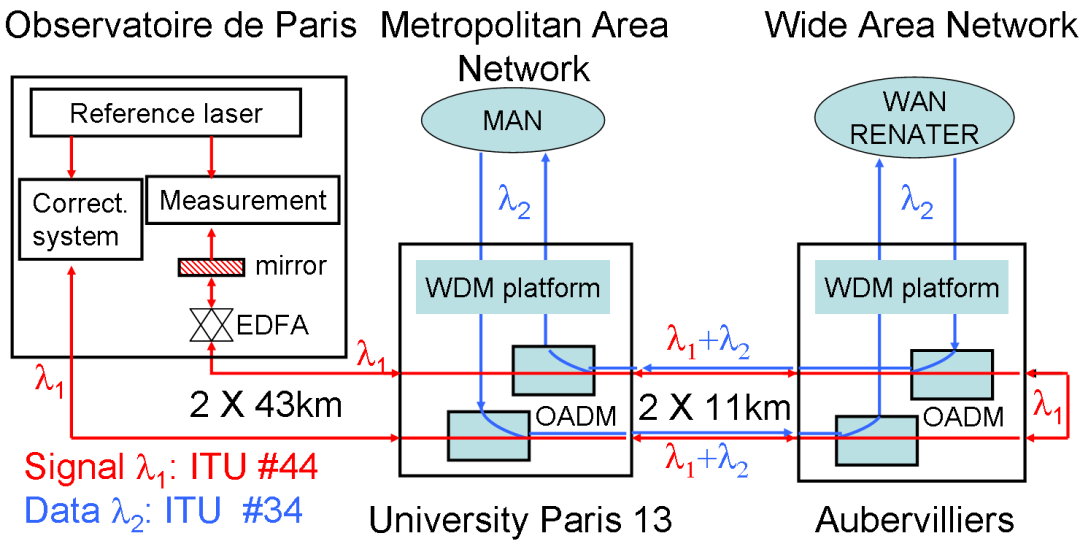


Figure 4.18: Schematic of the 108 km link, OADM: optical add-drop multiplexer, Comp: compensation system, WDM: wavelength division multiplexing, EDFA: bidirectional erbium-doped fiber amplifier, ITU: international telecommunication union, $\lambda_1$: 1542.14 nm, $\lambda_2$: 1550.12 nm.

This link is composed of four spans with a total length of 108 km (Fig.4.18). The first span is a dedicated fiber from the urban network which connects LNE-SYRTE and LPL, and extends over 43 km. The second and third spans are two 11 km fibers connecting the information service and technology center of university Paris 13 to a data center facility of the RENATER network located in Aubervilliers (near Paris). These two fibers transfer digital data through both the upstream and downstream with a rate of 10 Gbit/s in the channel ITU #34 (1550.42 nm). Our laser signal is at a wavelength of 1542.14 nm, which is in the channel ITU #44. At Aubervilliers the transferred optical frequency signal is sent into the other 11 km fiber toward University Paris 13, and then into a second 43 km dark fiber linking University Paris 13 to Observatoire de Paris. Four bidirectional off-the-shelf optical add-drop multiplexes (OADM) are employed for combining and separating these optical signals. Total attenuation of the link is about 38 dB. The 22 km round-trip between university Paris 13 and Aubervilliers has significant losses of 15 dB, which is attributed to the large number of connectors and the 4 OADMs. The signal injected into the 11 km fiber at university Paris 13 is 35 $\mu$W. Except for a bidirectional EDFA added at the remote end, the optical system is the same as shown in Fig.4.16.

#### 4.7.3.2 Experiment results

Internet traffic was unaffected during the whole period of the test (about three weeks). The bit-error rate was continuously monitored, and no transmission failure was observed. This was a crucial point, since the University Paris 13 is the access point of a metropolitan area network of about 100 km serving several high schools and universities.

The link stability performance is evaluated from the end-to-end beat-note signal. The optical phase noise PSD of the 108 km link is shown in Fig4.19 with and without compensation. The phase noise reduction reaches around 35 dB at 10 Hz, which is limited by the link delay (see Eq.4.8). The free-running phase-noise PSD (per unit of length) of the two 11 km fibers [14 $\text{rad}^2/(\text{Hz} \cdot \text{km})$ at 1 Hz] is ten times higher than the one of the 86 km fiber. The phase jitter of the optical signal from 1 Hz to 1 kHz increases from 0.4 rad to 1.5 rad due to the 22 km extension.

Fig.4.20 shows the fractional frequency instability of the 108 km link for four days of continuous operation (red circles) measured with a Π-type frequency counter and 10 Hz bandwidth. The fractional instability of the free-running fiber (black squares) is in the range of $10^{-15}$ for integration times longer than a few seconds. The link fractional instability (10 Hz

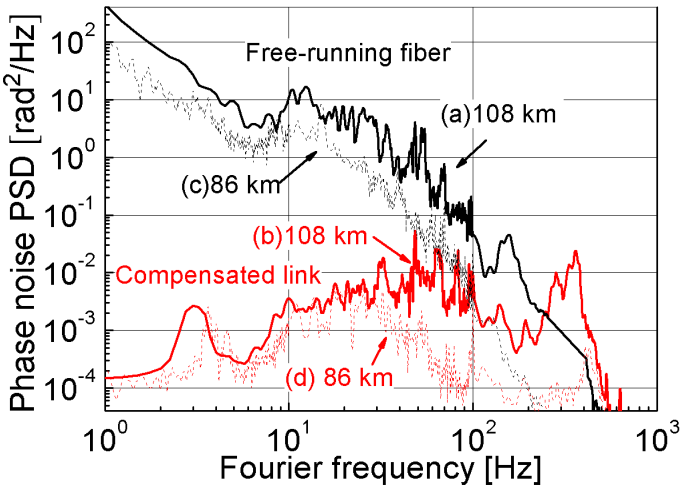


Figure 4.19: Phase noise PSD of the (a) free-running 108 km, (b) compensated 108 km links and, in dotted curves, (c) free-running 86 km and (d) compensated 86 km links.

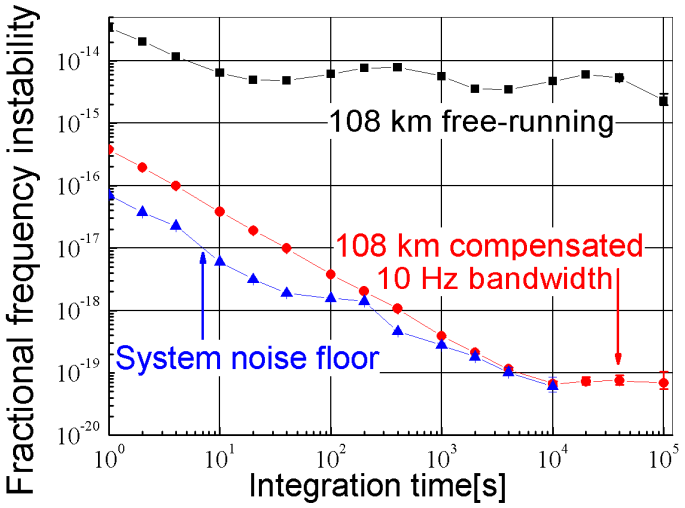


Figure 4.20: Fractional frequency instability of the 108 km free-running (black squares) and compensated link (red circles) and measurement noise floor (blue triangles).

bandwidth) is $4 \times 10^{-16}$ at 1 s integration time and scales down as $1/\tau$ from $1s$ to 5000 s. After $10^4$ s, it reaches a floor at about $7 \times 10^{-20}$. Without 10 Hz filtering, the Allan deviation is about five times higher between 1 s and 5000 s. The average frequency offset between the local signal and the transferred signal over the link is comparable to zero within the error bars with or without filtering. The Internet network degrades the short-term link stability, but not the long-term stability.

This experiment paves the way of using public fiber network to transfer ultra-stable frequency signal.

### 4.7.4 Repeater station

The multiple sub-link approach allows a broader noise compensation bandwidth compared with a single span link, but requires a repeater station between each segment.

#### 4.7.4.1 Function of the repeater station

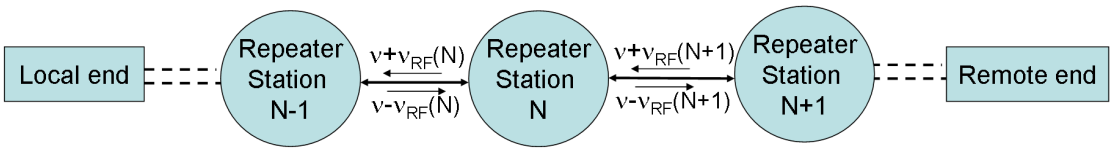


Figure 4.21: Scheme of a cascaded link, where $\nu$ is the optical frequency and $\nu_{RF}$ is the frequency shift.

Fig.4.21 shows the scheme of a cascaded link. The $N^{th}$ station of the link implements three functions. First, it processes a return optical signal to the previous station (N-1), in order to stabilize the incoming link (named N). Second, it produces a local signal by phase-locking a local optical oscillator to the signal from the previous station (N-1), and sends this signal to the next station (N+1). Third, it compensates the noise of the next link (N+1) by using the retro-reflected signal from the next station (N+1).

#### 4.7.4.2 Configuration of the station

The repeater station should be placed in a telecommunication station, where the access is restricted. Consequently, this station has to work automatically for a long period.

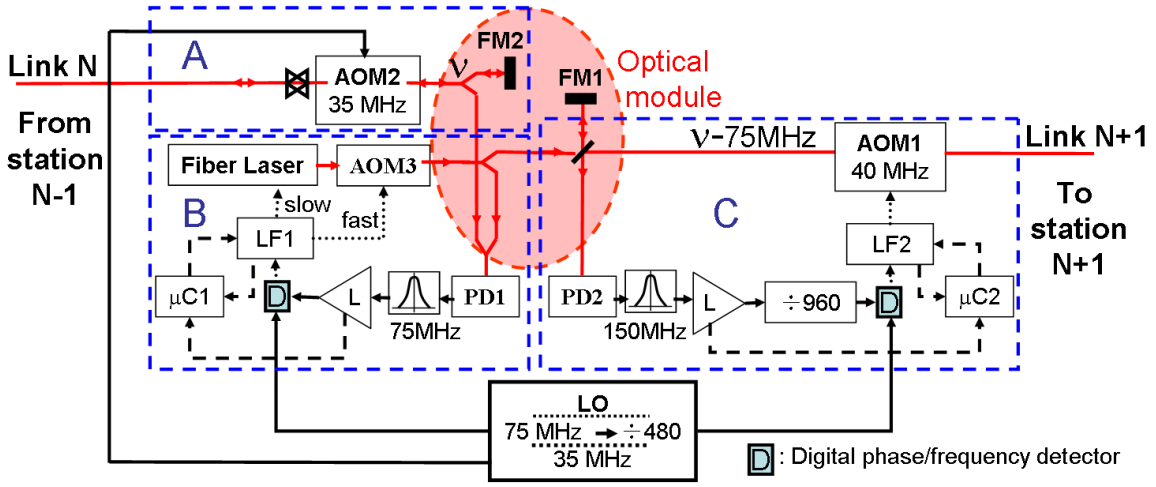


Figure 4.22: Scheme of the $N^{th}$ repeater station, FM: Faraday mirror (45° for single pass), PD: photodiode, LO: local oscillator, AOM: acousto-optic modulator, L: logarithmic amplifier, $\mu$C : micro-controller, LF: loop filter.

The scheme of the home-made repeater station is shown in Fig.4.22. The station includes three functional parts: (A) the remote end of the previous link, (B) the laser source, (C) the local end of the next link. The optical, RF, baseband analog and digital control signals[1] are shown in red (or grey) solid, black solid, dotted and dashed lines respectively. These logic signals are essential to restart the link operation, while the system is not normally operating.

#### 4.7.4.3 Function and operational process of sub-systems

The remote end (part A in Fig.4.22) is exactly the same as that of the improved experimental setup. It sends back part of the frequency-shifted laser signal from the previous station, and couples the rest to the laser source module.

In order to process the incoming signal from station N-1 with a frequency of $\nu$, we apply an optical configuration shown in part B in Fig.4.22. The local optical oscillator (Koheras Basik OEM) is a narrow linewidth fiber laser system based on a distributed-feedback technique. This laser is used as an optical tracking oscillator with a bandwidth of $100 - 150$ kHz. We use a digital phase/frequency detector rather than a classic mixer, so as to obtain a robust lock. This detector leads to a broad capture range of PLL. Furthermore, it can distinguish

[1]Usually, a digital control signal has two states: '0' and '1'.

which input frequency is higher, while a mixer can not. Thus, we can guarantee that the local laser frequency can only be locked to $\nu - 75$ MHz but not $\nu + 75$ MHz. However, the detector requires a larger signal-to-noise ratio for the input signals compared to a mixer, in order to avoid cycle slips.

A microcontroller ($\mu$C1) manages the automatic locking process with three steps. In the first step, a fast voltage ramp is applied to the laser PZT, thus tuning the laser frequency, and the input signal power of the logarithmic amplifier is monitored. When this power is above a reference level, meaning that the laser frequency is close to $\nu \pm 75$ MHz, the voltage ramp is stopped. Indeed, the laser frequency has swept over the right position after the ramp being stopped. In the second step, the laser PZT is driven by a slow voltage ramp of opposite sign. When the logarithmic amplifier input signal is high enough and the output signal of the digital phase/frequency detector (D) is passing across zero with the right slope, meaning that the laser frequency is closed to $\nu - 75$ MHz, this ramp is stopped. In the final step, the locking loops (see Fig.4.22) are sequentially closed. $\mu$C1 enables the integral and proportional gains of the fast loop at first. After that, it closes the slow loop with an integral gain. This system is very robust, allowing a long time operation (without re-locking for a few days).

At the local end (part C in Fig.4.22), the operational process of the loop (controlled by $\mu$C2) is exactly equivalent to that in part B. A combined-function of tracking oscillator and frequency-divider ($\div$960) is realized by using a DDS. The DDS, with a 1 GHz frequency reference provided by a VCO, simultaneously generates a 150 MHz signal and a 156.25 kHz signal. We lock the VCO with a bandwidth of $100 - 150$ kHz by using the beat-note between the 150 MHz signal and the link noise detection signal. Thus, the 156.25 kHz output of the DDS is the tracked and divided round-trip signal. Note that the operation of tracking is also controlled by $\mu$C2.

All RF signals are synthesized from a single local RF reference (see Fig.4.22). Thanks to the choice of the beat-note frequencies at 75 MHz and 150 MHz, the RF reference frequency drift effect is eliminated. The local laser is locked to the input signal (after AOM2) with a $-75$ MHz shift. The transferred signal to the next station is shifted to this local laser by $+75$ MHz, since the return signal from the next station is locked to the local laser signal with a 150 MHz shift. Both frequency shifts are synthesized from the same RF local oscillator of the station. Since they are opposite in sign, their sum is zero.

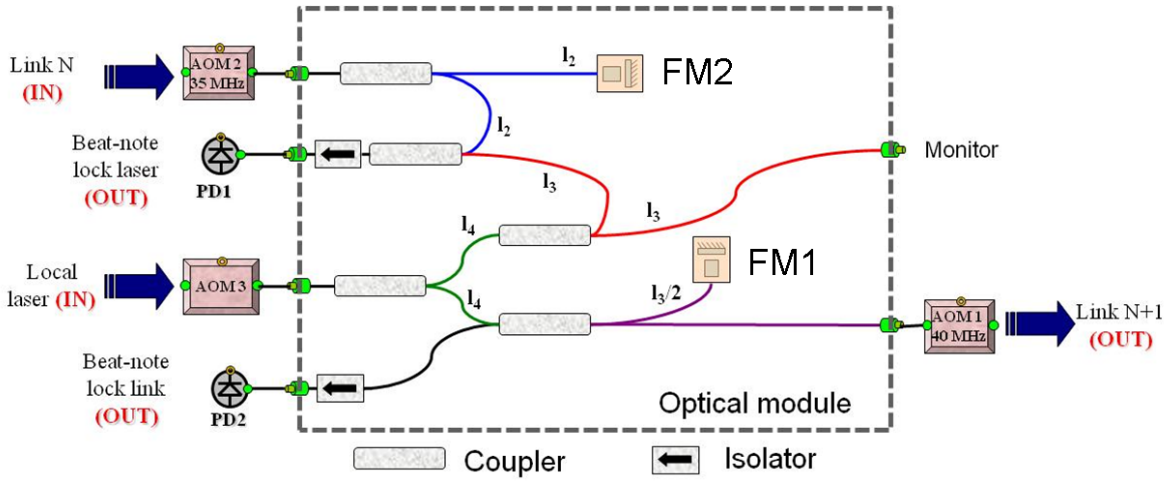


Figure 4.23: Scheme of the optical module (the ellipse part of Fig.4.22), FM: Faraday mirror, PD: photodiode, $I_2$, $I_3$ and $I_4$ are fiber lengths.

#### 4.7.4.4 Optical module

The telecom station's environment is usually much noisier and less stable (temperature) than that of the laboratory. Consequently, the fiber pigtail lengths of the optical system have been minimized and finely length-matched, in order to reduce the effect of the residual thermal fluctuations.

The compact optical module (see Fig.4.23) is realized by splicing off-the-shelf fiber-optic components. This module contains all non-common optical paths with respect to the link signal. This module is housed in an aluminum box (3 cm × 10 cm × 18 cm) covered by a thick polyurethane foam layer (5 cm) for shielding the thermal noise. Moreover, the temperature is actively stabilized around 298 K (i.e. 25 °C) by using a Peltier element. The temperature variation is less than 0.02 K when the ambient temperature fluctuates about 1 K.

The system noise floor shown in Fig.4.24 is measured in the laboratory environment with zero length link and full detection bandwidth. This floor is much lower than that of previous systems, approximately $10^{-17}$ at 1 s, and averages down in the range of $10^{-21}$ at 1 hour. This low instability is due to the fact that the optical system is well length-balanced and temperature-controlled.

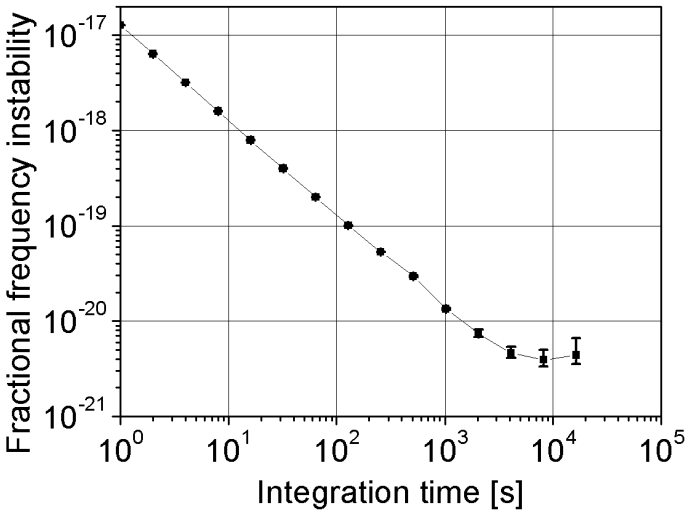


Figure 4.24: The instability of the repeat station system.

### 4.7.5 A 150 km + 150 km cascaded multiplexed optical link

This part shows the results of an experiment on a cascaded optical link, composed of two segments of Internet network fibers and one repeater station.

#### 4.7.5.1 Link configuration

The overall scheme of the 150 km + 150 km optical link (LPL-Nogent l'Artaud-LPL) with an intermediate repeater station located at Nogent l'Artaud (100 km east of Paris) is depicted in Fig.4.25. This link starts and ends at LPL, and is composed of three different fiber spans. In each span, there are two identical parallel fibers labeled as up-link and down-link. The up-link is used for transferring the link signal from LPL to Nogent l'Artaud, consisting of 114 km of fiber carrying Internet traffic and 36 km of dedicated dark fiber. The down-link represents the link from Nogent l'Artaud to LPL with the same configurations as the up-link. The first span is composed of two 11 km fibers connecting the information service and technology center of University Paris 13 to a Data Centre Facility (DCF) located in Aubervilliers (Interxion1). The digital stream between University Paris 13 and Aubervilliers is encoded on an optical carrier on channel ITU #34 (1550.12 nm), whereas the ultra-stable signal is carried by the channel ITU #44 (1542.14 nm). The second span is composed of two 36 km urban dark fibers

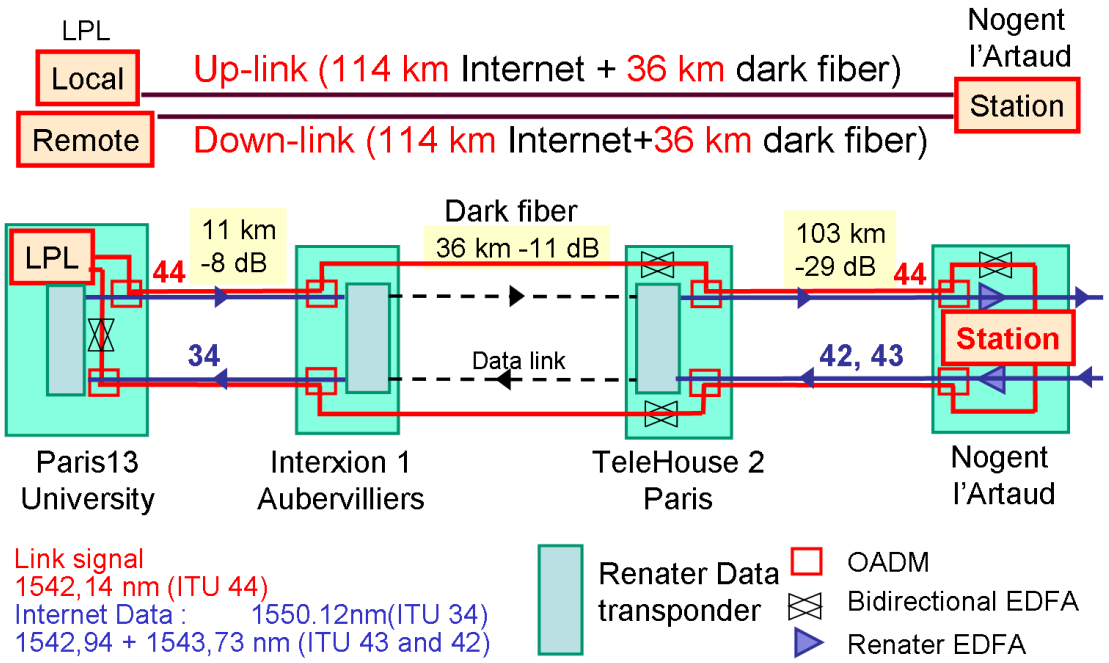


Figure 4.25: Schematic setup of 150 km+150 km cascaded link, OADM: optical add-drop multiplexer, EDFA: erbium-doped fiber amplifier, ITU: international telecommunication union, LPL: Laboratory of laser physics at university Paris 13.

which connect the two DCFs of Interxion 1 and TeleHouse 2 located in downtown Paris. The third span is composed of two 103 km long-haul intercity fibers simultaneously carrying Internet data traffic. In this part the digital data signals are transferred over channels ITU #42 and ITU #43, only 0.8 nm and 1.6 nm away from the link signal. At Nogent l'Artaud the link signal arriving from up-link is processed in the repeater station and sent into the down-link back to LPL.

Eight OADMs are used to insert and extract the link signal from the Internet fibers. The round-trip attenuation for each 150 km link is more than 100 dB due to fiber losses, OADMs and the large number of connectors. In order to compensate the losses, we used two bidirectional EDFAs for each link.

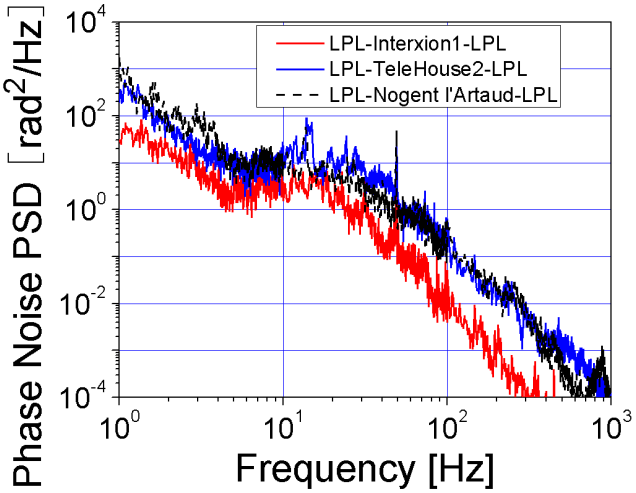


Figure 4.26: Phase noise PSD of the different subsections of the link: LPL-Interxion1-LPL of 22 km (red solid), LPL-Telehouse2-LPL link of 94 km (blue solid), and LPL-Nogent l'Artaud-LPL link of 300 km (black dashed).

#### 4.7.5.2 Measurement results

Fig.4.26 shows the phase noise PSD of the various segments composing the link. It indicates that the Interxion1-Telehouse2 segment is the noisiest one. It is not surprising, because this segment is located in the downtown Paris, therefore, suffers more noise induced by human actions.

The optical phase noise PSD of the 150 km + 150 km cascaded optical link is shown in Fig.4.27 with and without compensation. The phase noise reduction is about 50 dB at 1 Hz, which is limited by the fundamental limitation due to fiber delay. For Fourier frequencies below 5 Hz, both spectra exhibit some peaks which are probably due to seismic noise, since the optical fibers are likely to be buried along the railway tracks.

Fig.4.28 shows the variation of the link propagation delay over 3.5 days. Curve-a displays the variation of the 150 km+150 km free-running propagation delay measured by replacing the Nogent l'Artaud station with an optical amplifier. It gives the free-running fiber propagation delay fluctuation ($< 3$ ns), corresponding to a mean temperature change of less than 0.25 K. Curve-b shows the equivalent delay fluctuation of the compensated 150 km + 150 km cascaded

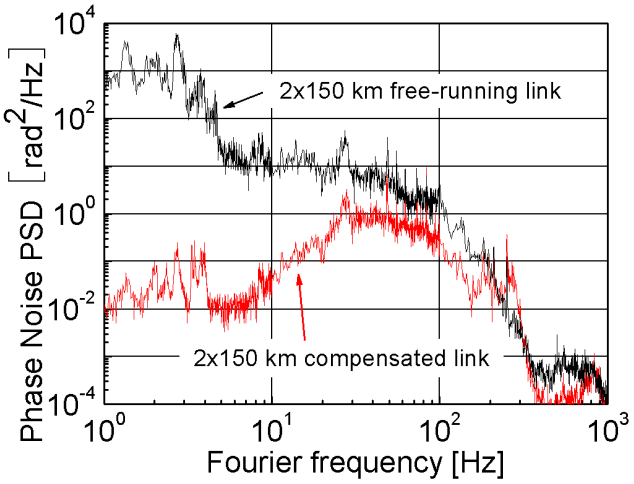


Figure 4.27: Phase noise PSD of the free running 150 km+150 km (black line) and compensated 150 km + 150 km link (red line).

link, which is about $\sim 10$ fs peak-to-peak. Curve-c is the equivalent fluctuation of the free-running up-link obtained by recording the frequency of AOM1 at LPL. It includes the delay fluctuation of the up-link and an equivalent delay fluctuation introduced by AOM2 at Nogent l'Artaud, whose frequency is drifting because there is no ultra-stable local RF reference at Nogent l'Artaud.

Fig.4.29 shows the fractional frequency stability of the 150 km+150 km link for four days of continuous operation, measured with the Π-type frequency counter. The free-running fiber instability (blue circles) is measured simultaneously by sampling the compensation signal applied to AOM1. The Allan deviation is $3 \times 10^{-15}$ at 1 s integration time and scales down as $1/\tau$ from 1 s to $\sim 1$ day reaching $7 \times 10^{-20}$ (measurement bandwidth 10 Hz). With the full bandwidth ($\sim 100$ kHz), the Allan deviation is about 3 times higher.

## 4.8 Summary and conclusion

### 4.8.1 Summary

The performance of the optical link is mainly determined by the noise level of the free-running link and the fundamental limitation due to the fiber delay. According to reported

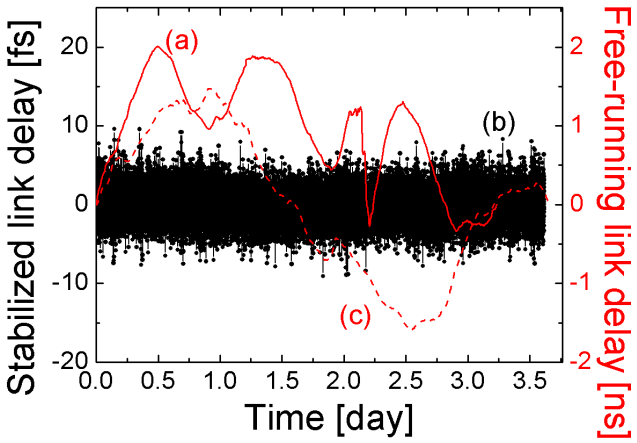


Figure 4.28: Variation of the optical link equivalent propagation delay (10 s sampling gate-time): (a) end-to-end propagation delay of the 150 km + 150 km free-running optical link recorded without repeater station at Nogent l'Artaud (red trace); (b) end-to-end propagation delay of the 150 km + 150 km cascaded compensated link (black trace); (c) correction signal (applied to AOM1 at LPL) of the 150 km up-link (red dashed trace).

experimental results, free-running link noise level can be very different from place to place, as shown in Fig4.30. Note that the link located in Tokyo is partly mounted in aerial cables, while all others are fully buried in the ground. Consequently, a cascaded link with short segments may be required, when noisy fiber networks are used. The shorter segment should be used for noisier networks, in order to well suppress the link noise.

The asymmetric noise effects, with respect to the propagation direction and path, have been discussed and evaluated. These effects are negligible for a well-engineered long-distance optical link.

At first, we transferred the optical signal with a 86 km dedicated urban networks (Jiang *et al.*, 2008). Taking advantage of the existing of public DWDM networks, we have extended the optical link by using a dedicated channel of these networks (100 GHz of width) (Kéfélian *et al.*, 2009b). Recently, a cascaded link was implemented in order to well suppress the link noise (Lopez *et al.*, 2010b). The fractional frequency instabilities listed in Tab.4.1 are mainly limited by the fundamental limitation on noise suppression due to fiber delay. The measurement bandwidth is about 10 Hz. The frequency instabilities are $3-5$ times higher

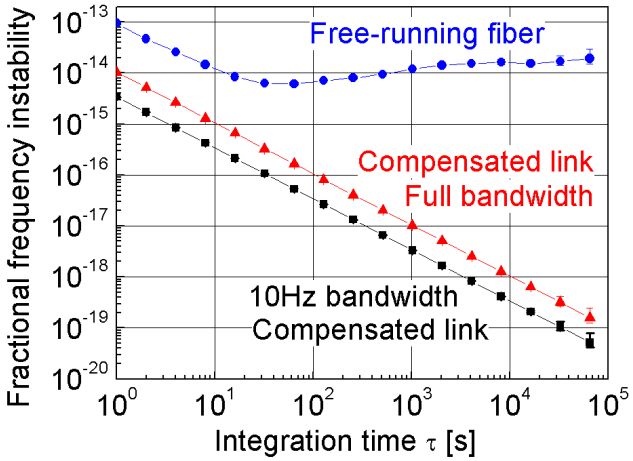


Figure 4.29: Fractional frequency instability of the 150 km + 150 km free-running link (blue circles), compensated link measured without (red triangles) and with a 10 Hz filter (black squares).

than Tab.4.1 when we use a measurement bandwidth of $\sim 100$ kHz.

Table 4.1: Instability of optical links

| Length $L$ (type) | $\sigma_y(1s)$ | $\sigma_y(10^4$ s) |
|---|---|---|
| 86 km (dedicated fiber) | $\sim 10^{-16}$ | $6 \times 10^{-19}$ |
| $2 \times 86$ km (dedicated fiber) | $3 \times 10^{-16}$ | $6 \times 10^{-19}$ |
| 108 km (dedicated channel) | $4 \times 10^{-16}$ | $8 \times 10^{-20}$ |
| 150 km + 150 km (dedicated channel) | $3 \times 10^{-15}$ | $4 \times 10^{-19}$ |

These results are calculated by using the overlapping Allan deviations of frequency samples recorded with the dead-time free Π-type counter.

### 4.8.2 Conclusion and perspective

A primary target of this project is to compare the frequencies of optical clocks located in France and Germany. Assuming the noise level along the link is comparable to that of the 150 km + 150 km link, the stability of this $\sim 1000$ km link with the cascaded configuration is

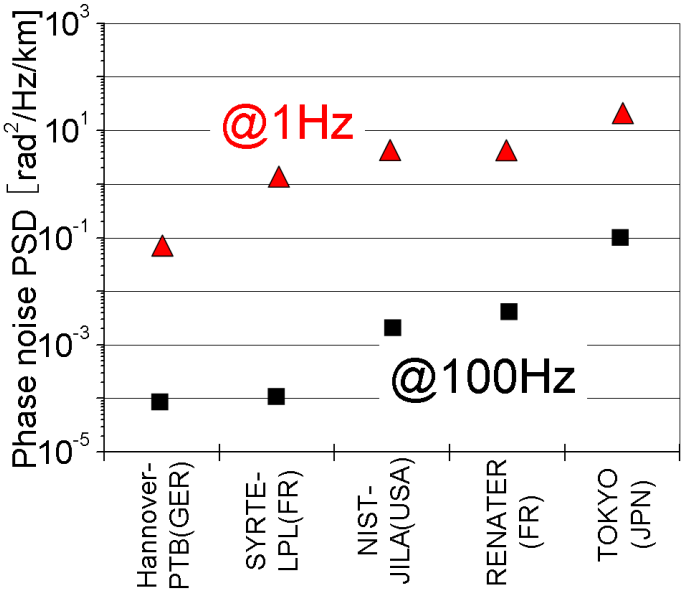


Figure 4.30: Phase noise level of fiber networks in different locations.

estimated to be in the range of $10^{-19}$ at one day integration time, which is compatible to the scientific target.

The key point of long distance cascaded link is the robustness of their repeater stations, which may be required to automatically operate over years.

At present, the repeater station does not have automatic adjustment of the beat-note amplitude between the local signal and the signal from the previous station. The polarization states can vary significantly with time, which may lead to a vanishing signal and result in the system out of lock. In the future, an automatic control system has to be implemented to maintain the beat-note power.

With these developments, we can think of future optical links, which extend to Germany, Italy and Great Britain, and finally connect most of the progress optical measurement laboratories in Europe, as shown in Fig.4.31.


Figure 4.31: Prospect optical links for Europe.

# Chapter 5

# Conclusions and Future work

This chapter concludes the thesis with a summary of the developments of ultra-stable laser sources and long distance optical links, and proposes several topics that should be considered in continuation of this work.

## 5.1 Ultra-stable laser sources

### 5.1.1 Cavity-stabilized laser

An ultra-stable cavity-stabilized laser was developed in order to provide the laser source for the optical link experiment.

The laser source is realized by stabilizing the frequency of a commercial fiber laser onto an ultra-stable FP cavity with the PDH method. In the thesis, I discuss considerations of the system design and analyze various noise effects in detail. The stabilized laser exhibits a sub-Hz linewidth for $\leq 10$ s measurement times. Its fractional frequency instability is about $10^{-15}$ at 1 s integration time, mainly limited by the fundamental thermodynamic noise of the reference cavity.

This laser exceeds the requirement of the optical link experiment. It has been used as the ultra-stable laser source for all the optical link experiments.

### 5.1.2 Fiber-stabilized laser

Fiber-stabilized lasers were developed for the repeater station of the optical link, where a robust and low noise local optical oscillator is required.

Compared with the ultra-stable cavity laser, the fiber-stabilized lasers are more robust, more compact, simpler, cheaper and more convenient for frequency tuning.

By combining advantages of the heterodyne detection, the Michelson interferometer configuration and a longer reference fiber, our fiber-stabilized lasers exhibit a significant improvement on the frequency noise than previously reported fiber-stabilized lasers. The frequency noise of this laser is well below 2 $\mathtt{Hz}^2/\mathtt{Hz}$ for frequencies higher than 1 Hz, and is comparable to that of our cavity-stabilized laser for frequencies higher than tens of Hertz. At present, the performance of the fiber-stabilized lasers is mainly limited by the environmental noise, which can be reduced further. A 2.5 km fiber-stabilized laser shows a highly-linear frequency tunability with frequency errors less than 50 Hz peak-to-peak for a 40.5 MHz/s frequency scan over 600 MHz. I have observed and explained the effect of Rayleigh backscattering (RBS) on the frequency-scanning laser for low Fourier frequencies. Moreover, a fundamental limitation due to double RBS is presented in the thesis.

This laser can be used for the optical link project, especially as the local laser source in a repeater station. It can also be used in Doppler-free optical frequency transfer between the ground and a low-orbit satellite, because of its unique agile and accurate frequency tunability.

## 5.2 Optical link

This thesis is devoted to the development of long distance ultra-stable optical frequency transfer. A long-range objective is to compare the frequency of optical clocks at LNE-SYRTE and PTB over a distance of $\sim$ 1000 km.

This thesis has demonstrated the principle and limitations of an optical link via optical fibers. The link delay induces the main limitation[1], since it limits the bandwidth of the noise correction control signal.

At first, we demonstrated an 86 km optical link composed of dedicated fibers connecting LNE-SYRTE and LPL. Later, we devised a double-pass configuration to simulate a real 172 km optical link. In succession, we successfully performed a pioneer experiment of ultra-stable optical signal transfer over a section of public networks, where link signals propagate in a dedicated channel of ITU (#44, 1542.14 nm). In the most recent experiment, we transferred the ultra-stable optical frequency through two 150 km cascaded segments. Most of this link

[1] It was first put forward in Newbury *et al.* (2007).

belongs to public fiber networks. These optical links ($86 - 300$ km) have shown a fractional instability in the range of $10^{-19}$ for $10^4$ s integration time with a 10 Hz measurement bandwidth. The performance of these links is close to the fundamental limitation due to the link delay.

According to the experimental results, we estimate that the link between LNE-SYRTE and PTB would exhibit an fractional instability of $\leq 10^{-18}$ within one day integration. This link can well reproduce the frequency of the best optical clock at the remote end with a transfer bandwidth of $\sim 10$ Hz.

## 5.3 Future work

In the future, we may consider following extensions to this work:

- A robust and transportable ultra-stable laser is required for some applications (e.g. space projects), therefore, it is useful to develop an ultra-stable cavity system with suitable mounting for this application.
- We need to study and minimize the vibration sensitivity of the fiber-stabilized laser. This thesis includes a preliminary study towards this goal.
- The temperature drift effect of fiber-stabilized laser should be reduced, if this laser is to be used as an independent laser source. It can be realized by a properly engineered thermal compensation/isolation of the fiber or by stabilization of the laser frequency to a more stable reference, such as an atomic transition.
- For a single-interferometer fiber-stabilized laser, the frequency noise control bandwidth is proportional to the inverse fiber delay. A multi-loop technique with fibers of different lengths can be used to broaden the control bandwidth without raising the frequency noise floor.
- The beat-note between the optical signals from a repeater station and its previous station has to be in an acceptable power range by an automatic alignment of the optical signals' polarization states, so as to realize a robust cascaded optical link. One possible approach is based on an automatic selection among two or three beat-notes between these optical signals with different polarization states. Another possible method is based on the polarization control of the local optical signal by using an automatic servo.

- Once the optical beat-note signal has been automatically optimized, the optical link performance could be improved by using a local tracking optical oscillator at the remote end as a source of the backward signal for the round-trip phase noise detection. Compared with the EDFA-amplified round-trip method, this return signal can be made stronger, and would reduce the broadband noise introduced by the EDFA.

- The fiber Brillouin amplification (FBA) developed at PTB exhibits higher gain and lower noise than the EDFA, although it requires a pump power of up to 30 mW and an accurate frequency control on the pump. Also, it is worth noting that this technique may lead to crosstalk on other signals for a public network. However, it is interesting to study the FBA which can simplify the optical link configuration at suitable conditions.

- In order to compare the best atomic clocks over an intercontinental distance, a composite optical link with both ground and space segments is a possible solution. The T2L2 has shown very good performance. However, ground stations of satellite-based links should be placed far away from the big cities where the best atomic clocks are usually located, mainly due to considerations on the climate conditions. On the other hand, the optical carrier frequency transfer based on satellites should be developed, so as to avoid (or reduce the number of) intermediate frequency conversions. Therefore, it may simplify the link configuration.

# Appendix A

# Characterization and measurement of frequency stability

Characterization and measurement of frequency stability are of fundamental importance in frequency metrology.

## A.1 Output signal model

The frequency stability of an oscillator indicates the degree of output frequency fluctuation in concern with a nominal frequency. Thus, the output of the oscillator can be written as [see for instance Barnes *et al.* (1971); Rutman & Walls (1991)]:

$$V(t) = [V_0 + \varepsilon(t)]sin[2\pi\nu_0 t + \phi(t)], \tag{A.1}$$

where $\phi(t)$ is a random process denoting phase noise, $V_0$ is the nominal amplitude, $\nu_0$ is the nominal frequency, $\varepsilon(t)$ represents the amplitude noise. This signal has an instantaneous frequency defined as:

$$\nu(t) = \frac{1}{2\pi}\frac{d[2\pi\nu_0 t + \phi(t)]}{dt} = \nu_0 + \frac{1}{2\pi}\frac{d\phi(t)}{dt} \tag{A.2}$$

Frequency noise is the random process described by

$$\Delta\nu(t) \equiv \nu(t) - \nu_0 = \frac{1}{2\pi}\frac{d\phi(t)}{dt}, \tag{A.3}$$

which is directly related to phase noise, as will be seen later. It is useful to introduce a normalized frequency fluctuation (i.e. the fractional frequency fluctuation):

$$\Delta y(t) = \frac{\Delta\nu(t)}{\nu_0} \texttt{ with } y(t) = \frac{\nu(t)}{\nu_0}. \tag{A.4}$$

Based on the random process model, two sets of tools are introduced for oscillator characterization:

- The spectral densities of phase and frequency noise in the so-called Fourier frequency domain.
- The variances/deviations of the averaged frequency fluctuations in the time domain.

In principle, the variances/deviations can be derived from spectral densities. In practise, they have different advantages and drawbacks because of the measurement limitations due to the measurement time, rate and bandwidth.

## A.2 Fourier frequency domain

In the Fourier frequency domain, phase and frequency noises are usually characterized by the double-sided power spectral density (PSD) in a bandwidth of 1 Hz, $S_\phi(f)$ and $S_{\Delta\nu}(f)$. They characterize the power density versus frequency, giving the so-called "frequency spectrum". They are related by the law (Barnes *et al.*, 1971):

$$S_{\Delta\nu}(f) = f^2 S_\phi(f), \tag{A.5}$$

which corresponds to the time derivative between $\Delta\nu(t)$ and $\phi(t)$. The units are $\texttt{Hz}^2/\texttt{Hz}$ and $\texttt{rad}^2/\texttt{Hz}$ respectively. It is worth noting that single-sided PSD is also widely used, e.g. the single-sided phase noise PSD

$$L_\phi(f) = \frac{1}{2} S_\phi(f), \tag{A.6}$$

with a unit of $\texttt{rad}^2/\texttt{Hz}$ (or $\texttt{dBc/Hz} = \textbf{dB}\ \texttt{rad}^2/\texttt{Hz}$).

The normalized frequency noise PSD is sometimes used, and is related with $S_{\Delta\nu}(f)$ and $S_\phi(f)$ by

$$S_y(f) = \frac{1}{\nu_0^2} S_{\Delta\nu}(f) = \frac{f^2}{\nu_0^2} S_\phi(f). \tag{A.7}$$

With this PSD, the noise levels of signals at different frequencies can be compared. The PSD can be classified by the power law model, where the spectral densities vary as a power of

$f$, so as to analyze and distinguish noise sources. Thus, the PSD becomes a sum of specific noises:

$$S_y(f) = \sum_{a=-2}^{2} h_a f^a, \tag{A.8}$$

where these items are named as white phase noise (a=-2), flicker phase noise (a=-1), white frequency noise (a=0), flicker frequency noise (a=1) and random-walk noise (a=2). For a given oscillator, the PSD in different frequency span may be dominated by one or two terms. Each term is usually related with a specific noise source.

Spectral densities of phase noise or frequency noise are measured by a spectrum analyzer (analog or digital). The time is rather long for measuring a low Fourier frequency PSD, therefore, the PSD are usually measured for Fourier frequencies higher than 1 Hz or 0.1 Hz.

Line-width, the full width at half-maximum (FWHM) of a spectrum, is a popular and traditional term for the characterization of the laser frequency noise. The laser linewidth is strongly related to the temporal coherence, characterized by the coherence time or coherence length. A laser source dominated by white frequency noise has a linewidth given by $\pi h_0$ (Elliott *et al.*, 1982), where $h_0$ is the double-sided PSD in $\mathtt{Hz}^2/\mathtt{Hz}$. For a laser dominated by higher order specific noises, the measured linewidth depends on the measurement time. Thus, this term is not very suitable for characterizing a free-running ultra-stable source, where the white frequency noise is not dominant for low Fourier frequencies. However, it can give a direct idea of the noise level to whom is acquainted with this term.

## A.3 Time domain

### A.3.1 Allan deviation

Random frequency process is characterized by several sample variances/deviations in the time domain. The original one is the two-sample standard deviation (also called ***Allan deviation***), which is the square root of the two-sample zero dead-time variance $\sigma_y^2(\tau)$ defined as (Allan, 1966; Barnes *et al.*, 1971; von Neumann *et al.*, 1941):

$$\sigma_y^2(\tau) = \left\langle \frac{(\overline{y}_{k+1} - \overline{y}_k)^2}{2} \right\rangle, \tag{A.9}$$

where

$$\begin{cases} \overline{y_k} = \frac{1}{\tau}\int_{t_k}^{t_k+\tau} y(t)dt = \frac{x_{k+1}-x_k}{\tau} \\ t_{k+1} = t_k + \tau \end{cases}. \tag{A.10}$$

in which $x_k$ and $x_{k+1}$ are measured time delays made at $t_k$ and $t_{k+1}$ times. $1/\tau$ is the fixed sampling rate which gives zero dead-time between frequency measurements.

The first estimator is:

$$\sigma_y^2(\tau_0, M) = \frac{1}{2(M-1)} \sum_{k=1}^{M-1} (\overline{y}_{k+1} - \overline{y}_k)^2 = \frac{1}{2\tau_0^2(M-1)} \sum_{k=1}^{M-1} (x_{k+2} - 2x_{k+1} + x_k)^2, \quad \text{(A.11)}$$

where $M$ is the number of frequency samples, and $\tau_0$ is the sampling time. The Allan variation $\sigma_y^2(n\tau_0, M)$ can be calculated with non-overlapped or overlapped method, where $n$ ($\geq 1$) is an integer. The non-overlapped variable estimator is

$$\sigma_y^2(n\tau_0, M) = \frac{1}{2(\frac{M}{n}-1)} \sum_{k=1}^{\frac{M}{n}-1} (\overline{y}_{nk+n} - \overline{y}_{nk})^2 = \frac{1}{2(n\tau_0)^2(\frac{M}{n}-1)} \sum_{k=1}^{\frac{M}{n}-1} (x_{nk+2n} - 2x_{nk+n} + x_{nk})^2. \quad \text{(A.12)}$$

The overlapping method, introduced in Howe *et al.* (1981) and Allan & Barnes (1981), is a more efficient estimator of $\sigma_y^2(\tau)$, which is calculated by the following equation:

$$\sigma_y^2(n\tau_0, M) = \frac{1}{2(M-2n+1)} \sum_{k=1}^{M-2n+1} (\overline{y}_{k+n} - \overline{y}_k)^2. \quad \text{(A.13)}$$

The result obtained by using overlapping or non-overlapping method has no bias with respect to the definition (see A.10).

The Allan deviation $\sigma_y(\tau)$ can be calculated from $S_y(f)$ (Cutler & Searle, 1966).

$$\sigma_y(\tau) = \sqrt{\int_0^\infty S_y(f) \frac{sin^4(\pi f \tau)}{(\pi f \tau)^2} df}. \quad \text{(A.14)}$$

### A.3.2 Other deviations

However, the slope of $\sigma_y^2(\tau)$ versus $\tau$ is the same of $\tau^{-1}$ for the white and flicker phase noises. In order to distinguish these two type noises, the modified Allan variance $MOD\sigma_y^2(\tau)$ is therefore put forward (Allan & Barnes, 1981; Howe *et al.*, 1981). The slope of $MOD\sigma_y^2(\tau)$ for these noise are $\tau^{-3/2}$ and $\tau^{-1}$ respectively. $MOD\sigma_y^2(\tau)$ is estimated by the equation:

$$MOD\sigma_y^2(n\tau_0, M) = \frac{1}{2(n\tau_0)^2(M-3n+2)} \sum_{i=1}^{M-3n+2} \left[ \sum_{k=i}^{n+i-1} (\overline{y}_{k+n} - \overline{y}_k) \right]^2. \quad \text{(A.15)}$$

Various other variances similar to the modified Allan variance were also introduced, including the Hadamard variance (Baugh, 1971), the modified Hadamard variance, and so on.

All of them filter phase fluctuations by using a finite-difference method. Consequently, their frequency responses show different frequency response slopes, which are helpful for analyzing the specific noise contribution. For example, one compares the frequencies of atomic clocks via a long-distance optical link. The frequency stability of atomic clocks is usually fundamentally limited by a white frequency noise, while the optical link is dominated by a white phase noise. Under this condition, the modified Allan deviation can rapidly determine the white frequency noise limitation of these clocks, thanks to its filtering function for the white phase noise. It is worth nothing that these estimators have a bias from the Allan variance.

These deviations can also be calculated from $S_y(f)$. For example, the modified Allan deviation is given by (Rutman & Walls, 1991)

$$MOD\sigma_y(n\tau_0) = \sqrt{\int_0^\infty S_y(f)\frac{sin^6(\pi f n\tau_0)}{(\pi f n\tau_0)^2 sin^2(\pi f\tau_0)}df}. \tag{A.16}$$

### A.3.3 Phase/Time jitter

$S_\phi(f)$ is usually measured in a frequency span from $f_l$ ($> 0$) to $f_h$. Consequently, a simplified estimator, ***Phase jitter*** is given by $\phi_{rms}(f_l, f_h) = \sqrt{\int_{f_l}^{f_h} S_\phi(f)df}$, indicating the phase variation. ***Time jitter*** $T_{rms}(f_l, f_h) = \phi_{rms}(f_l, f_h)/2\pi\nu_0$ is also widely used to express the uncertainty of a remote synchronization induced by the noise in a given bandwidth.

### A.3.4 Frequency counter

Frequency counter is the basic instrument for the measurement of the frequency stability in the time domain, which records the frequency of a RF/microwave signal. Here, I introduce three type of counters: the traditional counter (i.e. **Π*-type counter***), the high resolution triangle counter (i.e. **Λ*-type counter***) and the high resolution dead-time free Π-type counter (also named phase recorder).

The frequency sample $\nu_n$ is equal to $\int_{T_n}^{T_n+\tau} w(t)\nu(t)dt$, where $T_n$ is the starting time of the $n^{th}$ samples and $w(t)$ is the weighting function (see Fig.A.1). The frequency sample of Λ-type counter is an averaged value of many sub-samples (blocks in Fig.A.1b), leading to an efficient suppression of the white phase noise like the modified Allan deviation (Dawkins *et al.*, 2007). Comparisons of different counter samples and deviation resulting from specific noise are listed in TableA.1. For white/flicker phase noise dominated signal, significantly different results would be obtained with different counters or deviations.

## A. CHARACTERIZATION AND MEASUREMENT OF FREQUENCY STABILITY

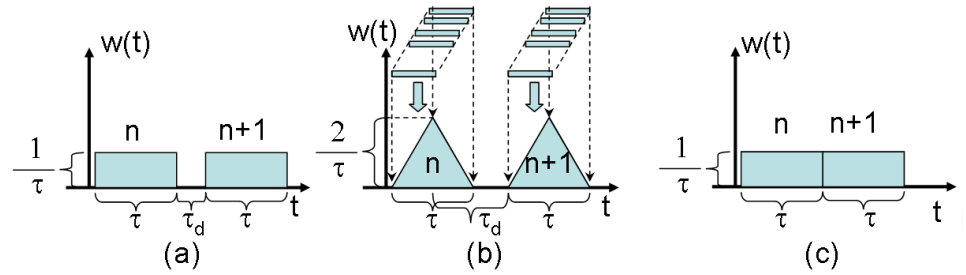


Figure A.1: Weighting function of frequency sampling, a) traditional Π-type counter, b) Λ-type counter, c) dead-time free Π-type counter, $\tau$ is the gate time and $\tau_d$ is the dead-time.

Table A.1: Comparisons of Standard Allan Deviation (Π-type Counter), Triangle Deviation (Λ-type Counter), and Modified Allan Deviation Resulting from Characteristic Noise. Note that $f_H$ (usually $f_H \gg 1/\tau$) is a cutoff frequency dependent on the working mode of the counter.—obtained from Dawkins *et al.* (2007)

| Noise Type | $S_y(f)$ | Allan $\sigma_y(\tau)$ | Triangle | Modified Allan |
|---|---|---|---|---|
| White Phase | $h_2 f^2$ | $\sqrt{\frac{3f_H}{4\pi^2\tau^2}h_2}$ | $\sqrt{\frac{8}{3f_H\tau}}\sigma_y(\tau)$ | $\sqrt{\frac{1}{2f_H\tau}}\sigma_y(\tau)$ |
| Flicker phase | $h_1 f^1$ | $\sqrt{\frac{1.038+3\ln(2\pi f_H\tau)}{4\pi^2\tau^2}h_1}$ | $\sqrt{\frac{12.56}{3.12+3.434f_H\tau}}\sigma_y(\tau)$ | $\sqrt{\frac{3.37}{3.12+3.434f_H\tau}}\sigma_y(\tau)$ |
| White Freq. | $h_0$ | $\sqrt{\frac{h_0}{\tau}}$ | $\sqrt{1.33}\sigma_y(\tau)$ | $\sqrt{0.5}\sigma_y(\tau)$ |
| Flicker Freq. | $h_{-1}f^{-1}$ | $\sqrt{2\ln(2)h_{-1}}$ | $\sqrt{1.30}\sigma_y(\tau)$ | $\sqrt{0.67}\sigma_y(\tau)$ |
| Rand. Walk | $h_{-2}f^{-2}$ | $\sqrt{\frac{2}{3}\pi^2 h_{-2}\tau}$ | $\sqrt{1.15}\sigma_y(\tau)$ | $\sqrt{0.82}\sigma_y(\tau)$ |

Both traditional and Λ-type counters yield a dead-time between two adjacent frequency samples. The dead-time degrades the phase conjugation between recorded frequencies, can even lead a white phase noise dominated signal to be seen as a white frequency noise dominated signal (Blair, 1974). In order to estimate the Allan deviation $\sigma_y(\tau)$ without a bias, the only method is use of data obtained by the dead-time free Π-type counter.

# Appendix B

# Parameters of the SMF-28 fiber

## B. PARAMETERS OF THE SMF-28 FIBER

Table B.1: Parameters of the SMF-28 fiber

-obtained from Glenn (1989), Knudsen *et al.* (1995), Chang *et al.* (2000) and the datasheet of SMF-28 fiber.

| **Parameter** | **Symbol** | **Value** | **Unit** |
|---|---|---|---|
| Attenuation | $L_{att}$ | $\sim 0.2$ @ 1.542 $\mu$m | $\frac{\mathrm{dB}}{\mathrm{km}}$ |
| Boltzmann constant | $k_B$ | $1.38 \times 10^{-23}$ | $\frac{\mathrm{J}}{\mathrm{K}}$ |
| Boundary condition parameter | $k_{max}$ | $2/\omega_0 = 3.846 \times 10^5$ | $\mathrm{m}^{-1}$ |
| Boundary condition parameter | $k_{min}$ | $2.405/a_f = 3.848 \times 10^4$ | $\mathrm{m}^{-1}$ |
| Chromatic Dispersion | $D_{cd}$ | $1.7 - 1.8$ @ 1.55 $\mu$m | $\frac{\mathrm{ps}}{\mathrm{nm \cdot km}}$ |
| Chromatic Dispersion Slope | $D'_{cd}$ | $\leq 4$ @ $1.54 - 1.55$ $\mu$m | $\frac{\mathrm{ps}}{\mathrm{nm^2 \cdot km}}$ |
| Effective refractive index | n | 1.468 @ 1.55 $\mu$m | |
| Fiber cladding radius | $a_f$ | 62.5 | $\mu$m |
| Fiber length | L | | km |
| Mode-field radius | $\omega_0$ | 5.2 $\pm$0.4@ 1.55 $\mu$m | $\mu$m |
| Polarization Mode Dispersion | $D_{pmd}$ | $\leq 0.1$ | $\frac{\mathrm{ps}}{\sqrt{\mathrm{km}}}$ |
| Temperature | T | 300 | K |
| Thermal conductivity | $\kappa$ | 1.37 | $\frac{\mathrm{W}}{\mathrm{m \cdot K}}$ |
| Thermal diffusivity | $D_{th}$ | $0.82 \times 10^{-6}$ | $\frac{\mathrm{m^2}}{\mathrm{s}}$ |
| Thermal expansion coefficient | $\alpha_L$ | $0.55 \times 10^{-6}$ | $\mathrm{K}^{-1}$ |
| Thermo-optic coefficient | dn/dT | $9.2 \times 10^{-6}$ | $\mathrm{K}^{-1}$ |
| Wavelength | $\lambda$ | 1542 | nm |

# Appendix C

# Cross-section and dimensions of SMF-28 and polyimide-coated fibers

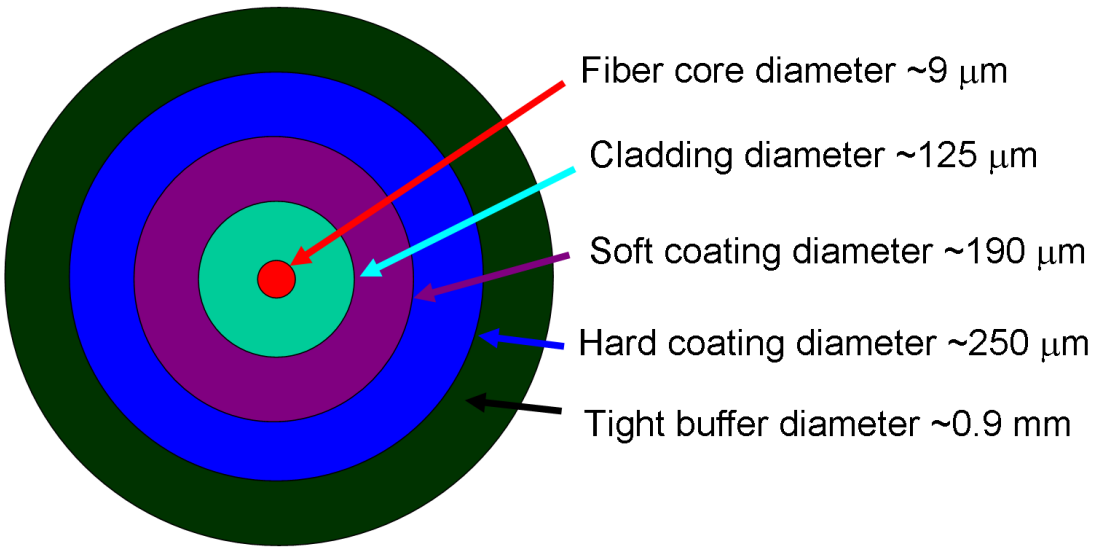


Figure C.1: Cross-section and dimensions of SMF-28 fiber.

## C. CROSS-SECTION AND DIMENSIONS OF SMF-28 AND POLYIMIDE-COATED FIBERS

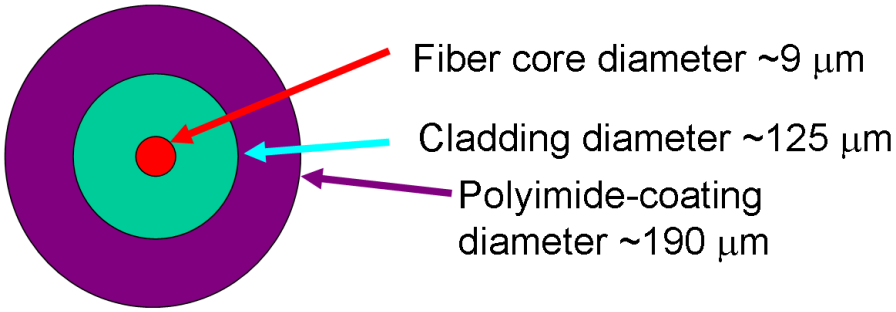


Figure C.2: Cross-section and dimensions of polyimide-coated fiber.

# References


Abraham, E.R. & Cornell, E.A. (1998). Teflon feedthrough for coupling optical fibers into ultrahigh vacuum systems. *Appl. Opt.*, **37**, 1762–1763. 52

Allan, D. (1966). Statistics of atomic frequency standards. *Proceedings of the IEEE*, **54**, 221–230. 141

Allan, D. & Barnes, J. (1981). A modified "allan variance" with increased oscillator characterization ability. *Proceedings of the 35th Annual Frequency Control Symposium. 1981*, 470–475. 142

Alnis, J., Matveev, A., Kolachevsky, N., Udem, T. & Hänsch, T.W. (2008). Subhertz linewidth diode lasers by stabilization to vibrationally and thermally compensated ultralow-expansion glass fabry-perot cavities. *Physical Review A (Atomic, Molecular, and Optical Physics)*, **77**, 053809. 8, 19, 20, 51

Amy-Klein, A., Goncharov, A., Daussy, C., Grain, C., Lopez, O., Santarelli, G. & Chardonnet, C. (2004). Absolute frequency measurement in the 28-thz spectral region with a femtosecond laser comb and a long-distance optical link to a primary standard. *Applied Physics B: Lasers and Optics*, **78**, 25–30. 6, 89

Amy-Klein, A., Goncharov, A., Guinet, M., Daussy, C., Lopez, O., Shelkovnikov, A. & Chardonnet, C. (2005). Absolute frequency measurement of a sf6 two-photon line by use of a femtosecond optical comb and sum-frequency generation. *Optics Letters*, **30**, 3320–3322. 6

Aso, Y., Ando, M., Otsuka, S. & Tsubono, K. (2006). Active vibration isolation using a suspension point interferometer. *Journal of Physics: Conference Series*, **32**, 451–456. 52

Barber, Z.W., Babbitt, W.R., Kaylor, B., Reibel, R.R. & Roos, P.A. (2010). Accuracy of active chirp linearization for broadband frequency modulated continuous wave ladar. *Appl. Opt.*, **49**, 213–219. 9, 38

Barger, R., Sorem, M. & Hall, J. (1973). Frequency stabilization of a cw dye laser. *Applied Physics Letters*, **22**, 573. 7

Barnes, J.A., Chi, A.R., Cutler, L.S., Healey, D.J., Leeson, D.B., Mcgunigal, T.E., Jr., J.A.M., Smith, W.L. & Sydnor, R.L. (1971). Characterization of frequency stability. *IEEE Trans. Instrum. Meas*, **20**, 105–120. 139, 140, 141

Bauch, A., Achkar, J., Bize, S., Calonico, D., Dach, R., Hlavac, R., Lorini, L., Parker, T., Petit, G., Piester, D., Szymaniec, K. & Uhrich, P. (2006). Comparison between frequency standards in europe and the usa at the $10^{-15}$ uncertainty level. *Metrologia*, **43**, 109–120. 11, 89

Baugh, R. (1971). Frequency modulation analysis with the hadamard variance. *Proceedings of the 25th Annual Symposium on Frequency Control*, 222–225. 142

Beenakker, C. & Schonenberger, C. (2003). Quantum shot noise. *Physics Today*, **56**, 37–42. 52

Black, E.D. (2001). An introduction to pound–drever–hall laser frequency stabilization. *American Journal of Physics*, **69**, 79–87. 16, 17, 28

Blair, B. (1974). *Time and frequency dissemination: an overview of principles and techniques.*. 144

Boggs, B., Greiner, C., Wang, T., Lin, H. & Mossberg, T.W. (1998). Simple high-coherence rapidly tunable external-cavity diode laser. *Opt. Lett.*, **23**, 1906–1908. 9, 38, 44

Cacciapuoti, L. & Salomon, C. (2009). Space clocks and fundamental tests: The aces experiment. *The European Physical Journal - Special Topics*, **172**, 57–68. 11, 12, 90

Cacciapuoti, L., Dimarcq, N., Santarelli, G., Laurent, P., Lemonde, P., Clairon, A., Berthoud, P., Jornod, A., Reina, F., Feltham, S. & Salomon, C. (2007). Atomic clock ensemble in space: Scientific objectives and mission status. *Nuclear*

*Physics B - Proceedings Supplements*, **166**, 303 – 306, proceedings of the Third International Conference on Particle and Fundamental Physics in Space, Proceedings of the Third International Conference on Particle and Fundamental Physics in Space. 11

Calhoun, M., Wang, R., Kirk, A., Diener, W., Dick, G.J. & L., T.R. (2000). Stabilized reference frequency distribution for radio science with the cassini spacecraft and the deep space network. *32nd Annual Precise Time and Time Interval (PTTI) Systems and Applications Meeting*. 12

Calhoun, M., Huang, S. & Tjoelker, R. (2007). Stable photonic links for frequency and time transfer in the deep-space network and antenna arrays. *Proceedings of the IEEE*, **95**, 1931–1946. 89, 90

Callen, H.B. & Greene, R.F. (1952). On a theorem of irreversible thermodynamics. *Phys. Rev.*, **86**, 702–710. 15, 20

Campbell, G.K., Ludlow, A.D., Blatt, S., Thomsen, J.W., Martin, M.J., Miranda, M.H.G.d., Zelevinsky, T., Martin, M.B., Ye, J., Diddams, S.A., Heavner, T.P., Parker, T. & Jefferts, S.R. (2008). The absolute frequency of the 87 sr optical clock transition. *Metrologia*, **45**, 539. 5, 89

Caves, C.M. (1980). Quantum-mechanical radiation-pressure fluctuations in an interferometer. *Phys. Rev. Lett.*, **45**, 75–79. 22

Chang, S., Hsu, C., Huang, T., Chuang, W., Tsai, Y., Shieh, J. & Leung, C. (2000). Heterodyne interferometric measurement of the thermo-optic coefficient of single mode fiber. *Chinese Journal of Physics*, **38**, 437–442. 146

Chen, L., Hall, J.L., Ye, J., Yang, T., Zang, E. & Li, T. (2006). Vibration-induced elastic deformation of fabry-perot cavities. *Phys. Rev. A*, **74**, 053801. 20, 78

Chen, Y.T. (1989). Use of single-mode optical fiber in the stabilization of laser frequency. *Appl. Opt.*, **28**, 2017–2021. 9, 37

Chou, C.W., Hume, D.B., Koelemeij, J.C.J., Wineland, D.J. & Rosenband, T. (2010). Frequency comparison of two high-accuracy $al+$ optical clocks. *Phys. Rev. Lett.*, **104**, 070802. 5, 89

Chu, S. (1998). Nobel lecture: The manipulation of neutral particles. *Reviews of Modern Physics*, **70**, 685. 3

Clairon, A., Dahmani, B., Acef, O., Granveaud, M., Domnin, Y., Pouchkine, S., Tatarenkov, V. & Felder, R. (1988). Recent experiments leading to the charcterization of the performance of the portable (HE-NE)/CH4 lasers .2. Results of the 1986 LPTF absolute frequency measurments. *Metrologia*, **25**, 9–16. 5

Clairon, A., Laurent, P., Santarelli, G., Ghezali, S., Lea, S. & Bahoura, M. (1995). A Cesium fountain frequency standard - prelimiary results. *IEEE Transactions on Instrumentation and Measurment*, **44**, 128–131, 1994 Conference on Precision Electromagnetic Measurements (CPEM 94), BOULDER, CO, JUN 27-JUL 01, 1994. 3

Cliche, J.F., Allard, M. & Têtu, M. (2006). Ultra-narrow linewidth and high frequency stability laser sources. *Optical Amplifiers and Their Applications/Coherent Optical Technologies and Applications*, CFC5. 9, 38, 64

Cohen-Tannoudji, C.N. (1998). Nobel lecture: Manipulating atoms with photons. *Reviews of Modern Physics*, **70**, 707. 3

Cranch, G., Dandridge, A. & Kirkendall, C. (2003). Suppression of double rayleigh scattering-induced excess noise in remotely interrogated fiber-optic interferometric sensors. *Photonics Technology Letters, IEEE*, **15**, 1582–1584. 60

Cranch, G.A. (2002). Frequency noise reduction in erbium-doped fiber distributed-feedback lasers by electronic feedback. *Opt. Lett.*, **27**, 1114–1116. 9, 38, 64

Crozatier, V., Gorju, G., Bretenaker, F., Gouët, J.L.L., Lorgeré, I., Gagnol, C. & Ducloux, E. (2006). Phase locking of a frequency agile laser. *Applied Physics Letters*, **89**, 261115. 9

Cutler, L. & Searle, C. (1966). Some aspects of the theory and measurement of frequency fluctuations in frequency standards. *Proceedings of the IEEE*, **54**, 136 – 154. 142

Darquié, B., Stoeffler, C., Shelkovnikov, A., Daussy, C., Amy-Klein, A., Chardonnet, C., Zrig, S., Guy, L., Crassous, J., Soulard, P., Asselin, P., Huet, T.R., Schwerdtfeger, P., Bast, R. & Saue, T. (2010). Progress toward the

first observation of parity violation in chiral molecules by high-resolution laser spectroscopy. *Chirality*, **22**, 870–884. 10

Daussy, C., Lopez, O., Amy-Klein, A., Goncharov, A., Guinet, M., Chardonnet, C., Narbonneau, F., Lours, M., Chambon, D., Bize, S., Clairon, A., Santarelli, G., Tobar, M.E. & Luiten, A.N. (2005). Long-distance frequency dissemination with a resolution of $10^{-17}$. *Physical Review Letters*, **94**, 203904. 12, 90, 101

Dawkins, S., Mcferran, J. & Luiten, A. (2007). Considerations on the measurement of the stability of oscillators with frequency counters. *Ultrasonics, Ferroelectrics and Frequency Control, IEEE Transactions on*, **54**, 918–925. 115, 143, 144

Day, T., Gustafson, E. & Byer, R. (1992). Sub-hertz relative frequency stabilization of two-diode laser-pumped nd:yag lasers locked to a fabry-perot interferometer. *Quantum Electronics, IEEE Journal of*, **28**, 1106–1117. 16

Dick, G.J. (1987). Local oscillator induced instabilities in trapped ion frequency standards. *in Proc. 19th Precise Time and Time Interval (PTTI) Applications and Planning Meeting, Redondo Beach*. 5

Dicke, R.H. (1953). The effect of collisions upon the doppler width of spectral lines. *Physical Review*, **89**, 472. 4

Diddams, S., Jones, D., Ma, L., Cundiff, S. & Hall, J. (2000). Optical frequency measurement across a 104-THz gap with a femtosecond laser frequency comb. *Optics Letters*, **25**, 186–188. 5

Djerroud, K., Acef, O., Clairon, A., Lemonde, P., Man, C.N., Samain, E. & Wolf, P. (2010). Coherent optical link through the turbulent atmosphere. *Opt. Lett.*, **35**, 1479–1481. 12

Donley, E.A., Heavner, T.P., Levi, F., Tataw, M.O. & Jefferts, S.R. (2005). Double-pass acousto-optic modulator system. *Review of Scientific Instruments*, **76**, 063112. 26

Dorsel, A., McCullen, J.D., Meystre, P., Vignes, E. & Walther, H. (1983). Optical bistability and mirror confinement induced by radiation pressure. *Phys. Rev. Lett.*, **51**, 1550–1553. 22

## REFERENCES


Drever, R.W.P., Hall, J.L., Kowalski, F.V., Hough, J., Ford, G.M., Munley, A.J. & Ward, H. (1983). Laser phase and frequency stabilization using an optical resonator. *Applied Physics B*, **31**, 97–105. 8, 15

Duan, L. & Gibble, K. (2005). Locking lasers with large fm noise to high-q cavities. *Opt. Lett.*, **30**, 3317–3319. 28

Elliott, D.S., Roy, R. & Smith, S.J. (1982). Extracavity laser band-shape and bandwidth modification. *Phys. Rev. A*, **26**, 12–18. 51, 141

Essen, L. & Parry, J.V.L. (1955). An atomic standard of frequency and time interval: A caesium resonator. *Nature*, **176**, 280–282. 3

Fischer, M., Kolachevsky, N., Zimmermann, M., Holzwarth, R., Udem, T., Hänsch, T.W., Abgrall, M., Grünert, J., Maksimovic, I., Bize, S., Marion, H., Santos, F.P.D., Lemonde, P., Santarelli, G., Laurent, P., Clairon, A., Salomon, C., Haas, M., Jentschura, U.D. & Keitel, C.H. (2004). New limits on the drift of fundamental constants from laboratory measurements. *Phys. Rev. Lett.*, **92**, 230802. 10

Foreman, S.M., Holman, K.W., Hudson, D.D., Jonesand, D.J. & Ye, J. (2007a). Remote transfer of ultrastable frequency references via fiber networks. *Review of Scientific Instruments*, **78**, 021101. 12, 90

Foreman, S.M., Ludlow, A.D., de Miranda, M.H.G., Stalnaker, J.E., Diddams, S.A. & Ye, J. (2007b). Coherent optical phase transfer over a 32-km fiber with 1 s instability at $10^{-17}$. *Physical Review Letters*, **99**, 153601. 13, 90

Fortier, T.M., Ashby, N., Bergquist, J.C., Delaney, M.J., Diddams, S.A., Heavner, T.P., Hollberg, L., Itano, W.M., Jefferts, S.R., Kim, K., Levi, F., Lorini, L., Oskay, W.H., Parker, T.E., Shirley, J. & Stalnaker, J.E. (2007). Precision atomic spectroscopy for improved limits on variation of the fine structure constant and local position invariance. *Phys. Rev. Lett.*, **98**, 070801. 10

Foster, S., Tikhomirov, A. & Milnes, M. (2007). Fundamental thermal noise in distributed feedback fiber lasers. *Quantum Electronics, IEEE Journal of*, **43**, 378–384. 50, 51

Geng, J., Spiegelberg, C. & Jiang, S. (2005). Narrow linewidth fiber laser for 100-km optical frequency domain reflectometry. *IEEE Photonics Technology Letters*, **17**, 1827. 87

Gerginov, V., Nemitz, N., Weyers, S., Schrder, R., Griebsch, D. & Wynands, R. (2010). Uncertainty evaluation of the caesium fountain clock ptb-csf2. *Metrologia*, **47**, 65. 4

Glenn, W. (1989). Noise in interferometric optical systems: an optical nyquist theorem. *Quantum Electronics, IEEE Journal of*, **25**, 1218–1224. 50, 146

Goldberg, B. (2000). Phase noise theory and measurements: A short review. *MICROWAVE JOURNAL*, **43**, 112+. 40

Gorju, G., Jucha, A., Jain, A., Crozatier, V., Lorgeré, I., Gouët, J.L.L., Bretenaker, F. & Colice, M. (2007). Active stabilization of a rapidly chirped laser by an optoelectronic digital servo-loop control. *Opt. Lett.*, **32**, 484–486. 9, 38

Greene, R.F. & Callen, H.B. (1952). On a theorem of irreversible thermodynamics. ii. *Phys. Rev.*, **88**, 1387–1391. 15, 20

Greiner, C., Boggs, B., Wang, T. & Mossberg, T.W. (1998). Laser frequency stabilization by means of optical self-heterodyne beat-frequency control. *Opt. Lett.*, **23**, 1280–1282. 9, 38, 44

Grosche, G., Terra, O., Predehl, K., Holzwarth, R., Lipphardt, B., Vogt, F., Sterr, U. & Schnatz, H. (2009). Optical frequency transfer via 146 km fiber link with 10-19 relative accuracy. *Opt. Lett.*, **34**, 2270–2272. 13, 90, 116

Grosche, G., Lipphardt, B., Schnatz, H., Santarelli, G., Lemonde, P., Bize, S., Lours, M., Narbonneau, F., Clairon, A., Lopez, O., Amy-Klein, A. & Chardonnet, C. (2007). Transmission of an Optical Carrier Frequency over a Telecommunication Fiber Link. In *2007 Conference on Lasers & Electro-Optics/Quantum Electronics and Laser Science Conference (CLEO/QELS 2007), Vols 1-5*, 428–429, IEEE. 101, 110

Hartog, A. & Gold, M. (1984). On the theory of backscattering in single-mode optical fibers. *Lightwave Technology, Journal of*, **2**, 76–82. 57, 94

Hocker, L., JAVAN, A., ROA, D., FRENKEL, L. & SULLIVAN, T. (1967). Absolute frequency measurement and spectroscopy of gas laser transitions in far infrared. *Applied Physics Letters*, **10**, 147–&. 5

Holman, K.W., Jones, D.J., *DarrenD. Hudson & Ye, J. (2004). Precise frequency transfer through a fiber network by use of 1.5-$\mu$m mode-locked sources. *Opt. Lett.*, **29**, 1554–1556. 13, 90

Hong, F.L., Musha, M., Takamoto, M., Inaba, H., Yanagimachi, S., Takamizawa, A., Watabe, K., Ikegami, T., Imae, M., Fujii, Y., Amemiya, M., Nakagawa, K., Ueda, K. & Katori, H. (2009). Measuring the frequency of a sr optical lattice clock using a 120 km coherent optical transfer. *Opt. Lett.*, **34**, 692–694. 13, 90, 117

Hough, J. & Rowan, S. (2005). Laser interferometry for the detection of gravitational waves. *Journal of Optics A: Pure and Applied Optics*, **7**, S257. 87

Howe, D., Allan, D. & Barnes, J. (1981). Properties of signal sources and measurement methods. 669 – 716. 142

Howe, D., Hati, A., Nelson, C., Taylor, J. & Ashby, N. (2007). Active vibration-induced pm noise control in optical fibers: Preliminary studies. *Frequency Control Symposium, 2007 Joint with the 21st European Frequency and Time Forum. IEEE International*, 552–556. 80, 82

Huang, S., Tu, M., Yao, S. & Maleki, L. (2000). A 'turn-key' optoelectronic oscillator with low acceleration sensitivity. *FCS'2000*, CL00–0626. 78, 82

Jefferts, S.R., Heavner, T.P., Parker, T.E. & Shirley, J.H. (2007). Nist cesium fountains: current status and future prospects. *Time and Frequency Metrology*, **6673**, 667309. 4

Jenkins, F.A. & White, H.E. (1981). *Fundamentals of Optics, 4 the ed.* McGraw-Hill, Inc. 74

Jiang, H., Kéfélian, F., Crane, S., Lopez, O., Lours, M., Millo, J., Holleville, D., Lemonde, P., Chardonnet, C., Amy-Klein, A. & Santarelli, G. (2008). Long-distance frequency transfer over an urban fiber link using optical phase stabilization. *J. Opt. Soc. Am. B*, **25**, 2029–2035. 13, 15, 90, 131

Jiang, H., Kéfélian, F., Lemonde, P., Clairon, A. & Santarelli, G. (2010). An agile laser with ultra-low frequency noise and high sweep linearity. *Opt. Express*, **18**, 3284–3297. 9, 15, 38

Kéfélian, F., Jiang, H., Lemonde, P. & Santarelli, G. (2009a). Ultralow-frequency-noise stabilization of a laser by locking to an optical fiber-delay line. *Opt. Lett.*, **34**, 914–916. 9, 15, 38

Kéfélian, F., Lopez, O., Jiang, H., Chardonnet, C., Amy-Klein, A. & Santarelli, G. (2009b). High-resolution optical frequency dissemination on a telecommunications network with data traffic. *Opt. Lett.*, **34**, 1573–1575. 13, 15, 90, 91, 131

Kersey, A.D., Marrone, M.J. & Davis, M.A. (1991). Polarisation-insensitive fibre optic michelson interferometer. *Electronics Letters*, **27**, 518–520. 46, 115

Kim, J., Cox, J.A., Chen, J. & Kaertner, F.X. (2008). Drift-free femtosecond timing synchronization of remote optical and microwave sources. *NATURE PHOTONICS*, **2**, 733–736. 13, 90

Kleckner, D., Irvine, W.T.M., Oemrawsingh, S.S.R. & Bouwmeester, D. (2010). Diffraction-limited high-finesse optical cavities. *Phys. Rev. A*, **81**, 043814. 17

Kleppner, D. (2006). Time too good to be true. *Physics Today*, **59**, 10–11. 5, 90

Knabe, K., Wu, S., Lim, J., Tillman, K.A., Light, P.S., Couny, F., Wheeler, N., Thapa, R., Jones, A.M., Nicholson, J.W., Washburn, B.R., Benabid, F. & Corwin, K.L. (2009). 10 khz accuracy of an optical frequency reference based on 12c2h2-filled large-core kagome photonic crystal fibers. *Opt. Express*, **17**, 16017–16026. 77

Knudsen, S., Tveten, A. & Dandridge, A. (1995). Measurements of fundamental thermal induced phase fluctuations in the fiber of a sagnac interferometer. *Photonics Technology Letters, IEEE*, **7**, 90–92. 50, 146

Kogelnik, H. & Li, T. (1966). Laser beams and resonators. *Appl. Opt.*, **5**, 1550–1567. 28

Kumagai, M., Fujieda, M., Nagano, S. & Hosokawa, M. (2009). Stable radio frequency transfer in 114 km urban optical fiber link. *Opt. Lett.*, **34**, 2949–2951. 12, 90

Laurent, P., Abgrall, M., Clairon, A., Lemonde, P., Santarelli, G., Salomon, C., Massonnet, D., Cacciapuoti, L. & Ieee (2008). *ACES/PHARAO Space Program Status*. 2008 Ieee International Frequency Control Symposium, Vols 1 and 2, Ieee, New York. 11

Lavielle, V., Lorgeré, I., Gouët, J.L.L., Tonda, S. & Dolfi, D. (2003). Wideband versatile radio-frequency spectrum analyzer. *Opt. Lett.*, **28**, 384–386. 87

Layland, J.W. & Rauch, L.L. (1997). The evolution of technology in the deep space network: A history of the advanced systems program. *Jet Propulsion Laboratory, Pasadena, CA, TDA Prog. Rep.*. 89

Legero, T., Kessler, T. & Sterr, U. (2010). Tuning the thermal expansion properties of optical reference cavities with fused silica mirrors. *J. Opt. Soc. Am. B*, **27**, 914–919. 8, 20

Levi, F., Calonico, D., Lorini, L. & Godone, A. (2006). Ien-csf1 primary frequency standard at inrim: accuracy evaluation and tai calibrations. *Metrologia*, **43**, 545. 4

Lipson, S., Lipson, H. & Tannhauser, D. (1995). *Optical Physics (3rd ed.)*. London: Cambridge. 17

Livas, J.C., Thorpe, J.I., Numata, K., Mitryk, S., Mueller, G. & Wand, V. (2009). Frequency-tunable pre-stabilized lasers for lisa via sideband locking. *Classical and Quantum Gravity*, **26**, 094016. 17

Lopez, O., Amy-Klein, A., Daussy, C., Chardonnet, C., Narbonneau, F., Lours, M. & Santarelli, G. (2008). 86-km optical link with a resolution of $2x10^{-18}$ for rf frequency transfer. *The European Physical Journal D*, **48**, 35–41. 12, 90, 100, 101

Lopez, O., Amy-Klein, A., Lours, M., Chardonnet, C. & Santarelli, G. (2010a). High-resolution microwave frequency dissemination on an 86-km urban optical link. *Applied Physics B: Lasers and Optics*, **98**, 723–727. 12, 90, 100, 101

Lopez, O., Haboucha, A., Kéfélian, F., Jiang, H., Chanteau, B., Roncin, V., Chardonnet, C., Amy-Klein, A. & Santarelli, G. (2010b). Cascaded multiplexed optical link on a telecommunication network for frequency dissemination. *Opt. Express*, **18**, 16849–16857. 13, 15, 90, 91, 131

Ludlow, A.D., Huang, X., Notcutt, M., Zanon-Willette, T., Foreman, S.M., Boyd, M.M., Blatt, S. & Ye, J. (2007). Compact, thermal-noise-limited optical cavity for diode laser stabilization at 1e-15. *Opt. Lett.*, **32**, 641–643. 8, 23, 28, 51, 78, 84

Ludlow, A.D., Zelevinsky, T., Campbell, G.K., Blatt, S., Boyd, M.M., de Miranda, M.H.G., Martin, M.J., Thomsen, J.W., Foreman, S.M., Ye, J., Fortier, T.M., Stalnaker, J.E., Diddams, S.A., Le Coq, Y., Barber, Z.W., Poli, N., Lemke, N.D., Beck, K.M. & Oates, C.W. (2008). Sr Lattice Clock at 1 x 10-16 Fractional Uncertainty by Remote Optical Evaluation with a Ca Clock. *Science*, **319**, 1805–1808. 89

Lutes, G. (1980). Optical fiber for the distribution of frequency and timing references. *12nd Annual Precise Time and Time Interval (PTTI) Applications and Planning Meeting*. 12, 90

Ma, L.S., Jungner, P., Ye, J. & Hall, J.L. (1994). Delivering the same optical frequency at two places: accurate cancellation of phase noise introduced by an optical fiber or other time-varying path. *Opt. Lett.*, **19**, 1777–1779. 13, 90, 91, 94

Ma, L.S., Bi, Z., Bartels, A., Kim, K., Robertsson, L., Zucco, M., Windeler, R.S., Wilpers, G., Oates, C., Hollberg, L. & Diddams, S.A. (2007). Frequency uncertainty for optically referenced femtosecond laser frequency combs. *IEEE Journal of Quantum Electronics*, **43**, 139–146. 6

Margolis, H.S. (2010). Optical frequency standards and clocks. *Contemporary Physics*, **51**, 37 – 58. 90

Marion, H., Pereira Dos Santos, F., Abgrall, M., Zhang, S., Sortais, Y., Bize, S., Maksimovic, I., Calonico, D., Grünert, J., Mandache, C., Lemonde, P., Santarelli, G., Laurent, P., Clairon, A. & Salomon, C. (2003). Search for variations of fundamental constants using atomic fountain clocks. *Phys. Rev. Lett.*, **90**, 150801. 10

Marra, G., Margolis, H.S., Lea, S.N. & Gill, P. (2010). High-stability microwave frequency transfer by propagation of an optical frequency comb over 50 km of optical fiber. *Opt. Lett.*, **35**, 1025–1027. 13, 90

Maxwell, J.C. (1873). *Treatise on Electricity and Magnetism*. Oxford: Clarendon. 2

Meiser, D., Ye, J., Carlson, D.R. & Holland, M.J. (2009). Prospects for a millihertz-linewidth laser. *Physical Review Letters*, **102**, 163601. 15

Millo, J., Abgrall, M., Lours, M., English, E.M.L., Jiang, H., Guéna, J., Clairon, A., Tobar, M.E., Bize, S., Coq, Y.L. & Santarelli, G. (2009a). Ultralow noise microwave generation with fiber-based optical frequency comb and application to atomic fountain clock. *Applied Physics Letters*, **94**, 141105. 15

Millo, J., aes, D.V.M., Mandache, C., Coq, Y.L., English, E.M.L., Westergaard, P.G., Lodewyck, J., Bize, S., Lemonde, P. & Santarelli, G. (2009b). Ultrastable lasers based on vibration insensitive cavities. *Physical Review A (Atomic, Molecular, and Optical Physics)*, **79**, 053829. 8, 15, 20, 22, 35, 41, 51, 78, 84

Millo, J., Boudot, R., Lours, M., Bourgeois, P.Y., Luiten, A.N., Coq, Y.L., Kersal, Y. & Santarelli, G. (2009c). Ultra-low-noise microwave extraction from fiber-based optical frequency comb. *Opt. Lett.*, **34**, 3707–3709. 15

Much, R., Daganzo, E., Feltham, S., Nasca, R., Cacciapuoti, L., Hess, M.P., Stringhetti, L. & Salomon, C. (2009). Status of the ACES Mission. 199–204, Joint Meeting of the 23rd European Frequency and Time Forum/IEEE International Frequency Control Symposium, Besancon, France, Apr 20-24, 2009. 4

Mucke, O.D., Kuzucu, O., Wong, F.N.C., Ippen, E.P., Kartner, F.X., Foreman, S.M., Jones, D.J., Ma, L.S., Hall, J.L. & Ye, J. (2004). Experimental implementation of optical clockwork without carrier-envelopephase control. *Opt. Lett.*, **29**, 2806–2808. 6

Musha, M., Hong, F.L., Nakagawa, K. & ichi Ueda, K. (2008). Coherent optical frequency transfer over 50-km physical distance using a 120-km-long installed telecom fiber network. *Opt. Express*, **16**, 16459–16466. 13, 89, 90, 117

Narbonneau, F., Lours, M., Bize, S., Clairon, A., Santarelli, G., Lopez, O., Daussy, C., Amy-Klein, A. & Chardonnet, C. (2006). High resolution frequency standard dissemination via optical fiber metropolitan network. *Review of Scientific Instruments*, **77**, 064701. 12, 90, 101

Nazarova, T., Riehle, F. & Sterr, U. (2006). Vibration-insensitive reference cavity for an ultra-narrow-linewidth laser. *Applied Physics B: Lasers and Optics*, **83**, 531–536. 20, 78, 84

Newbury, N.R., Williams, P.A. & Swann, W.C. (2007). Coherent transfer of an optical carrier over 251 km. *Opt. Lett.*, **32**, 3056–3058. 13, 90, 92, 95, 110, 113, 114, 115, 117, 136

Notcutt, M., Ma, L.S., Ye, J. & Hall, J.L. (2005). Simple and compact 1-hz laser system via an improved mounting configuration of a reference cavity. *Opt. Lett.*, **30**, 1815–1817. 15, 20, 28, 78

Numata, K., Kemery, A. & Camp, J. (2004). Thermal-noise limit in the frequency stabilization of lasers with rigid cavities. *Phys. Rev. Lett.*, **93**, 250602. 8, 15, 20, 51

Okoshi, T., Kikuchi, K. & Nakayama, A. (1980). Novel method for high resolution measurement of laser output spectrum. *Electronics Letters*, **16**, 630–631. 37, 97

Parker, T.E. (2010). Long-term comparison of caesium fountain primary frequency standards. *Metrologia*, **47**, 1. 4

Pavlis, N.K. & Weiss, M.A. (2003). The relativistic redshift with 3 10 -17 uncertainty at nist, boulder, colorado, usa. *Metrologia*, **40**, 66. 5, 90

Peik, E., Lipphardt, B., Schnatz, H., Schneider, T., Tamm, C. & Karshenboim, S.G. (2004). Limit on the present temporal variation of the fine structure constant. *Phys. Rev. Lett.*, **93**, 170801. 10

Pellegrini, C. (2006). Overview of single pass free electron lasers. *Prepared for 10th European particle accelerator conference (EPAC06), Scotland*. 89

Phillips, W.D. (1998). Nobel lecture: Laser cooling and trapping of neutral atoms. *Reviews of Modern Physics*, **70**, 721. 3

Pistoni, N.C. & Martinelli, M. (1991). Polarization noise suppression in retracing optical fiber circuits. *Opt. Lett.*, **16**, 711–713. 46, 115

Pound, R. (1946). Electronic frequency stabilization of microwave oscillators. *Review of Scientific Instruments*, **17**, 490–505. 8

Predehl, K., Holzwarth, R., Udem, T., Haensch, T., Terra, O., Grosche, G., Lipphardt, B. & Schnatz, H. (2009). Ultra Precise Frequency Dissemination across Germany - Towards a 900 km Optical Fiber Link from PTB to MPQ. 1555–1556, Conference on Lasers and Electro-Optics/Quantum Electronics and Laser Science Conference (CLEO/QELS 2009), Baltimore, MD, JUN 02-04, 2009. 118

Quessada, A., Kovacich, R.P., Courtillot, I., Clairon, A., Santarelli, G. & Lemonde, P. (2003). The dick effect for an optical frequency standard. *Journal of Optics B: Quantum and Semiclassical Optics*, **5**, S150. 5

Rabi, I.I. (1945). Meeting at new york, january 19 and 20, 1945. *Phys. Rev.*, **67**, 199–204. 2

Ramsey, N. (1983). History of atomic clocks. *Journal of research of the National Bureau of Standards*, **88**, 301–320. 3

Ramsey, N.F. (1965). The atomic hydrogen maser. *Metrologia*, **1**, 7. 3

Ramsey, N.F. & Silsbee, H.B. (1951). Phase shifts in the molecular beam method of separated oscillating fields. *Phys. Rev.*, **84**, 506–507. 3

Roos, P.A., Reibel, R.R., Berg, T., Kaylor, B., Barber, Z.W. & Babbitt, W.R. (2009). Ultrabroadband optical chirp linearization for precision metrology applications. *Opt. Lett.*, **34**, 3692–3694. 9, 38

Rubiola, E., Salik, E., Huang, S., Yu, N. & Maleki, L. (2005). Photonic-delay technique for phase-noise measurement of microwave oscillators. *J. Opt. Soc. Am. B*, **22**, 987–997. 97

Rutman, J. & Walls, F.L. (1991). Characterization of frequency stability in precision frequency sources. *Proceedings of the IEEE*, **79**, 952–960. 139, 143

Samain, E., Vrancken, P., Weick, J. & Guillemot, P. (2007). T2l2 flight model metrological performances. *Frequency Control Symposium, 2007 Joint with the 21st European Frequency and Time Forum. IEEE International*, 1291–1294. 12

Samain, E., Exertier, P., Guillemot, P., Pierron, F., Albanese, D., Paris, J., Torre, J.M., Petitbon, I., Leon, S. & Ieee (2009). Time transfer by laser link t2l2 first results. 194–198. 12, 90

Santarelli, G., Audoin, C., Makdissi, A., Laurent, P., Dick, G. & Clairon, A. (1998). Frequency stability degradation of an oscillator slaved to a periodically interrogated atomic resonator. *Ultrasonics, Ferroelectrics and Frequency Control, IEEE Transactions on*, **45**, 887 –894. 5

Santarelli, G., Laurent, P., Lemonde, P., Clairon, A., Mann, A.G., Chang, S., Luiten, A.N. & Salomon, C. (1999). Quantum projection noise in an atomic fountain: A high stability cesium frequency standard. *Phys. Rev. Lett.*, **82**, 4619–4622. 4

Satyan, N., Vasilyev, A., Rakuljic, G., Leyva, V. & Yariv, A. (2009). Precise control of broadband frequency chirps using optoelectronic feedback. *Opt. Express*, **17**, 15991–15999. 9

Saulson, P.R. (1994). *Fundamentals of interferometeric gravitational wave detectors*. World Scientific. 22

Schnatz, H., Lipphardt, B., Helmcke, J., Riehle, F. & Zinner, G. (1996). First phase-coherent frequency measurement of visible radiation. *Phys. Rev. Lett.*, **76**, 18–21. 5

Schoof, A., Grünert, J., Ritter, S. & Hemmerich, A. (2001). Reducing the linewidth of a diode laser below 30 hz by stabilization to a reference cavity with a finesse above $10^5$. *Opt. Lett.*, **26**, 1562–1564. 28

Seel, S., Storz, R., Ruoso, G., Mlynek, J. & Schiller, S. (1997). Cryogenic optical resonators: A new tool for laser frequency stabilization at the 1 hz level. *Phys. Rev. Lett.*, **78**, 4741–4744. 15, 84

Sellmeier, W. (1971). Zur erklarung der abnormen farbenfolge im spectrum einiger sub stanzen. *Annalen der Physik und Chemie*, **219**, 272–282. 74

Sheard, B.S., Gray, M.B. & McClelland, D.E. (2006). High-bandwidth laser frequency stabilization to a fiber-optic delay line. *Appl. Opt.*, **45**, 8491–8499. 40, 41

Shelkovnikov, A., Butcher, R.J., Chardonnet, C. & Amy-Klein, A. (2008). Stability of the proton-to-electron mass ratio. *Physical Review Letters*, **100**, 150801. 10, 89

Shillue, B., AlBanna, S., D'Addario, L. & ieee (2004). *Transmission of low phase noise, low phase drift millimeter-wavelength references by a stabilized fiber distribution*

*system*. 2004 Ieee International Topical Meeting on Microwave Photonics, Technical Digest, Ieee, New York. 90

Szymaniec, K., Chalupczak, W., Whibberley, P.B., Lea, S.N. & Henderson, D. (2005). Evaluation of the primary frequency standard npl-csf1. *Metrologia*, **42**, 49. 4

Takahashi, K., Ando, M. & Tsubono, K. (2008). Stabilization of laser intensity and frequency using optical fiber. In *Conference Series 122*, 102016, IOP. 9, 38, 64

Taylor, J., Nelson, C., Hati, A., Ashby, N. & Howe, D. (2008). Vibration-induced pm noise measurements of a rigid optical fiber spool. *Frequency Control Symposium, 2008 IEEE International*, 807–810. 80, 82

Terra, O., Grosche, G., Predehl, K., Holzwarth, R., Legero, T., Sterr, U., Lipphardt, B. & Schnatz, H. (2009). Phase-coherent comparison of two optical frequency standards over 146 km using a telecommunication fiber link. *Applied Physics B: Lasers and Optics*, **97**, 541–551. 13, 89, 90, 117

Terra, O., Grosche, G. & Schnatz, H. (2010). Brillouin amplification in phase coherent transfer of optical frequencies over 480 km fiber. *Opt. Express*, **18**, 16102–16111. 13, 90, 118

Thomson, S.W. & Tait, P.G. (1878). *Treatise on natural philosophy*. Cambrage: England. 2

Thorpe, M.J. & Ye, J. (2008). Cavity-enhanced direct frequency comb spectroscopy. *Applied Physics B: Lasers and Optics*, **91**, 397–414. 6

Touahri, D., NEZ, F., ABED, M., ZONDY, J., ACEF, O., HILICO, L., CLAIRON, A., MILLERIOUX, Y., BIRABEN, F., JULIEN, L. & FELDER, R. (1995). LPTF frequency-synthesis chain - reuslts and improvement for the near future. *IEEE Transactions on Instrumentation and Measurement*, **44**, 170–172, 1994 Conference on Precision Electromagnetic Measurements (CPEM 94), Boulder, CO, Jun 27-Jul 01, 1994. 5

Tsujikawa, K., Tajima, K. & Ohashi, M. (2000). Rayleigh Scattering Reduction Method for Silica-Based Optical Fiber. *Journal of Lightwave Technology*, **18**, 1528. 59

Udem, T., Reichert, J., Holzwarth, R. & Hänsch, T.W. (1999). Absolute optical frequency measurement of the cesium $d_1$ line with a mode-locked laser. *Phys. Rev. Lett.*, **82**, 3568–3571. 5

Vessot, R.F.C., Levine, M.W., Mattison, E.M., Blomberg, E.L., Hoffman, T.E., Nystrom, G.U., Farrel, B.F., Decher, R., Eby, P.B., Baugher, C.R., Watts, J.W., Teuber, D.L. & Wills, F.D. (1980). Test of relativistic gravitation with a space-borne hydrogen maser. *Phys. Rev. Lett.*, **45**, 2081–2084. 91

Vian, C., Rosenbusch, P., Marion, H., Bize, S., Cacciapuoti, L., Zhang, S., Abgrall, M., Chambon, D., Maksimovic, I., Laurent, P., Santarelli, G., Clairon, A., Luiten, A., Tobar, M. & Salomon, C. (2005). Bnm-syrte fountains: recent results. *Instrumentation and Measurement, IEEE Transactions on*, **54**, 833–836. 4

von Neumann, J., Kent, R.H., Bellinson, H.R. & Hart, B.I. (1941). The mean square successive difference. *Annals of Mathematical Statistics*, **12**, 153–162. 141

Wanser, K. (1992). Fundamental phase noise limit in optical fibres due to temperature fluctuations. *Electronics Letters*, **28**, 53–54. 41, 50

Webster, S.A., Oxborrow, M. & Gill, P. (2007). Vibration insensitive optical cavity. *Phys. Rev. A*, **75**, 011801. 8, 15, 20, 78, 84

Webster, S.A., Oxborrow, M., Pugla, S., Millo, J. & Gill, P. (2008). Thermal-noise-limited optical cavity. *Physical Review A (Atomic, Molecular, and Optical Physics)*, **77**, 033847. 8, 19, 51

White, A. (1965). Frequency stabilization of gas lasers. *IEEE Journal of Quantum Electronics*, **1**, 349–357. 7

Wieman, C.E. & Gilbert, S.L. (1982). Laser-frequency stabilization using mode interference from a reflecting reference interferometer. *Opt. Lett.*, **7**, 480–482. 7

Wilcox, R., Byrd, J.M., Doolittle, L., Huang, G. & Staples, J.W. (2009). Stable transmission of radio frequency signals on fiber links using interferometric delay sensing. *Opt. Lett.*, **34**, 3050–3052. 10, 13, 89, 90

Williams, P.A., Swann, W.C. & Newbury, N.R. (2008). High-stability transfer of an optical frequency over long fiber-optic links. *J. Opt. Soc. Am. B*, **25**, 1284–1293. 13, 90, 95, 96, 110, 114, 117

Wolf, P., Bord, C., Clairon, A., Duchayne, L., Landragin, A., Lemonde, P., Santarelli, G., Ertmer, W., Rasel, E., Cataliotti, F., Inguscio, M., Tino, G., Gill, P., Klein, H., Reynaud, S., Salomon, C., Peik, E., Bertolami, O., Gil, P., Pramos, J., Jentsch, C., Johann, U., Rathke, A., Bouyer, P., Cacciapuoti, L., Izzo, D., De Natale, P., Christophe, B., Touboul, P., Turyshev, S., Anderson, J., Tobar, M., Schmidt-Kaler, F., Vigu, J., Madej, A., Marmet, L., Angonin, M.C., Delva, P., Tourrenc, P., Metris, G., Mller, H., Walsworth, R., Lu, Z., Wang, L., Bongs, K., Toncelli, A., Tonelli, M., Dittus, H., L?mmerzahl, C., Galzerano, G., Laporta, P., Laskar, J., Fienga, A., Roques, F. & Sengstock, K. (2009). Quantum physics exploring gravity in the outer solar system: the sagas project. *Experimental Astronomy*, **23**, 651–687. 87

Yao, X. & Maleki, L. (2000). Multiloop optoelectronic oscillator. *Quantum Electronics, IEEE Journal of*, **36**, 79–84. 41

Ye, J., Peng, J.L., Jones, R.J., Holman, K.W., Hall, J.L., Jones, D.J., Diddams, S.A., Kitching, J., Bize, S., Bergquist, J.C., Hollberg, L.W., Robertsson, L. & Ma, L.S. (2003). Delivery of high-stability optical and microwave frequency standards over an optical fiber network. *J. Opt. Soc. Am. B*, **20**, 1459–1467. 12, 90

Young, B.C., Cruz, F.C., Itano, W.M. & Bergquist, J.C. (1999). Visible lasers with subhertz linewidths. *Phys. Rev. Lett.*, **82**, 3799–3802. 8, 15, 22, 28, 32

Zhang, W., Xu, Z., Lours, M., Boudot, R., Kersale, Y., Santarelli, G. & Le Coq, Y. (2010). Sub-100 attoseconds stability optics-to-microwave synchronization. *Applied Physics Letters*, **96**. 6

Zhao, Y.N., Zhang, J., Stejskal, A., Liu, T., Elman, V., Lu, Z.H. & Wang, L.J. (2009). A vibration-insensitive optical cavity and absolute determination of its ultrahigh stability. *Opt. Express*, **17**, 8970–8982. 42

Zhu, M. & Hall, J.L. (1993). Stabilization of optical phase/frequency of a laser system: application to a commercial dye laser with an external stabilizer. *J. Opt. Soc. Am. B*, **10**, 802–816. 16